NTNU – Trondheim
Norwegian University of
Science and Technology

Faculty of Engineering Science and Technology
Department of Civil and Transport Engineering

Thesis Title:	Date: 7/6/2015		
Laboratory Investigation of the Pore Pressure Built-Up in Moving Debris	**Number of pages** (incl. appendices): 102		
	Master Thesis	×	Project Work	

Name: XIANG YU

Professor in charge/supervisor: VIKAS THAKUR

Other external professional contacts/supervisors:

Abstract

Debris flow poses significant threat to property and human life mainly as a result of its high sediment concentrations and mobility. For the purpose of predicting debris flow mobility and mitigating potential damage, considerable attention has been drawn to the development of debris flow physical models. Despite of the achievements, a thorough mechanism accounting for the built-up and maintaining of pore pressure within the shearing layer of debris flow has not been made available mainly due to the lack of experiment data. In viewing of that situation this study developed a coaxial-cylinder apparatus and conducted two series of tests concerning pore pressure built-up in samples of varying solid fraction concentration (by volume) and fine grain content (by weight) at differing rotational velocity.

The first series of tests show that when solid fraction concentration increase from 20% to 50%, pore pressure built-up tends to be higher. The second series of tests exhibit that similar pattern can apply except for samples with 80% and 100% silt content. This peculiarity together with grain size analyses before and after experiment give rise to a postulation that mixing rods shearing may be responsible for the constant pore pressure built-up, while «most breakable grain sizes" may exist and have led to the extraordinarily low peak values and prolonged decline in samples with rich silt content through dilatancy. Nonlinear relationship between pore pressure built-up and rotational velocity was found in all tests. Initial stagnation and transitional stage were observed for most samples; plausible explanations have been proposed. Concerning the shortcomings of current study, some recommendations are also provided.

Keywords:

1. debris flow	4. solid fraction concentraton
2. coaixial-cylinder	5. fine grain content
3. pore pressure built-up	

I

Master thesis

SPRING 2015
XIANG YU

Laboratory investigation of the pore pressure built-up in moving debris

Background

Debris flow is gravity-driven mixture of sediment and water, and is mechanically characterized by the interaction of solid and liquid fractions. Initiated by heavy rain fall or slope failure, debris flow may entrain more material on its way and gain disastrous momentum before deposition. Each year around the world debris flow causes considerable damage and claim many fatalities. In order to predict the mobility of debris flow and estimate the potential influenced area, multiple physical models have been developed. Practically most models are based on a single-constituent material even though a debris flow is clearly a mixture. Therefore, the role played by the fluid can at most be incorporated parametrically, and certainly not kinematically. Solid-fluid interaction (including pore pressure generation and dissipation) plays a significant role in the entrainment and detrainment processes involved in moving debris. However, until now, only few experiments have been dedicated to the significance of pore-liquid pressure built-up, and its correlation to flowing velocity and grain size on a limited range of samples. In view of this, this study shall help in improving our understanding of the pore pressure built-up in moving debris. Debris flow is a vast topic and it is not possible to cover all aspects in one master thesis. Therefore, a dedicated description of tasks to be carried-out in this master thesis is as follows.

Task Description

- Literature review on debris flow classification, process, pore pressure built-up and entrainment as influencing factors of its mobility.

- Development a new laboratory set-up to study the pore-pressure built-up in moving debris. i.e. development of a coaxial-cylinder, mixing component and data collecting system.

- Testing on varieties of samples of varying solid fraction concentration, and fine contents.

- Establish a relationship between the pore pressure and fine contents in debris

- Analyze test results and compare with the results with the literature.

- Evaluate the representativeness of results, and the effectiveness of this apparatus.

- Come up with improving measures and proposals concerning better experimental study of pore pressure built-up and entrainment effect in the future.

VIKAS THAKUR
Professor
Geotechnical Division, NTNU

Preface

This thesis is submitted in partial fulfillment of the requirement for Master's Degree (MSc) in Geotechnics and Geohazards at the Geotechnical Division of Civil and Transport Engineering Department, Norwegian University of Science and Technology (NTNU). It was carried out in the spring semester of 2015.

The idea for this thesis was raised by Professor Vikas Thakur which focuses on the laboratory investigation of pore pressure built-up in the basal layer of moving debris flow.

Trondheim, Norway

Xiang Yu

_____

Xiang Yu

June 2015

Acknowledgement

First and foremost, I wish to thank my supervisor, Vikas Thakur, Professor at the Geotechnical Division, NTNU. He has been supportive since I was an intern at Statens Vegvesen last summer. I remember that he shew the learning curve to encourage me to keep trying on some numerical back-analyses. He helped me come up with the thesis topic, and guided me over each stage of thesis work. Many ideas present in this thesis would have been impossible without the regular discussions with him. In addition, writing of the thesis also benefited a lot from Professor Vikas's advices on reference papers and phrasing.

Besides my advisor, I would like to thank engineers Per Asbjørn Østensen and Frank Stæhli for their assiduous work in fabricating the experiment apparatus and writing the programme. The phrase said by Per that "paper may seem concise and neat, but science is most often messy and arduous" is definitely another treasure gained in my master project.

Acknowledgement also goes to the support from the "Effective countermeasures for the debris and mudflow hazards" project which is financed by the Ferry free E-39 project by the Norwegian Public Roads Administration.

Many people have also helped and taught me during my thesis work and two years study at NTNU. Professor Steinar Nordal has been guiding and inspiring me through the courses he taught, and some random talks in the corridor. Professor Gustav Grimstad had been continuously bothered by my silly questions especially during theoretical soil mechanics course. Later he lent his strong support in my summer job application. Scientist Harald Norem from Statens Vegvesen is deeply appreciated for sharing his rich knowledge in debris flow. Senior engineer Jan Jønland is thanked for retrieving and preparing silt sample for my use. Engineer Geir Tesaker from Hydrodynamics Lab, NTNU is also thanked for providing me with coarse sand twice. Special gratitude goes to research assistant Ashenafi Lulseged Yifru at the division for the instructions of several tests and the constructive advices on the writing of thesis.

I thank my fellow classmates and friends Hiruy Ghidey, Antonios Nikolaos Tzatzakis, Cecilie Myklebust Helle and Suresh Shrestha for the stimulating discussions, and the wonderful two years we had together.

I would like to thank my parents, my younger sister and her cute baby for supporting me spiritually throughout my life and providing me with endless happiness.

Finally I would like to thank my girlfriend, Mengjie Zhang, whom I believe is a precious gift given by God. Her accompany has been and will always be the best thing I can image in the world.

Contents

List of figures

List of tables

XVII

List of symbols

α	Dynamics angle of internal friction
β	Angle of an infinite slope
γ_w	Unit weight of water
γ_d	Bulk density of the plastic substance
γ_f	Floating ratio
$\dot{\gamma}$	Shearing rate
θ	Angle of downstream channel; volumetric water content
θ_u	Angle of internal friction
μ_f	Dynamic viscosity of liquid
ρ	Density of interstitial liquid
ρ_s	Density of solid particles
$\sigma \text{ or } \sigma_t$	Total normal stress
σ_a	Pressure acting on the top of a debris element in coaxial cylinder
σ_b	Pressure acting on the bottom of a debris element in coaxial cylinder
τ	Shear stress
τ_r	Shear strength
τ_y	Yield strength
τ_i	Initial shear strength
τ_f	Maximum shear strength
τ_r	Residual shear strength
φ	Internal friction angle
ω	Rotational velocity
λ	Pore pressure ratio
λ_s	Linear grain concentration defined in Bagnold number

1.Introduction

1.1. Background

Debris flow represents a gravity-driven mixture of sediment particles of various sizes and water flowing down channel-shaped region. Triggered by heavy precipitation, rapid snow melting, warm wind and abrupt change in the temperatures, debris flow constitutes surging fronts, variably erodible sediment and compositions that may change with position and time. Each year around the world debris flow causes considerable damage and claim many life losses. In Norway fatalities caused by debris flow are less than in many other countries because of the low population density in influenced areas. However, annual economic losses from damage on properties and infrastructures are enormous. According to the statistics, alone in year 2011, the cost of damage increased by about 100 Million Euros (NIFS 2014). Recent experiences from Norway and also the studies (e.g. (Nadim, Kjekstad et al. 2006, NVE 2011, Infrarisk 2013, NIFS 2014)) suggest there is a growth in the frequency and/or intensity of extreme rainfall, rapid snow melting, and change in the ambient temperatures. In return, the frequencies and the magnitudeof debris flow have increased (see Fig. 1.1).
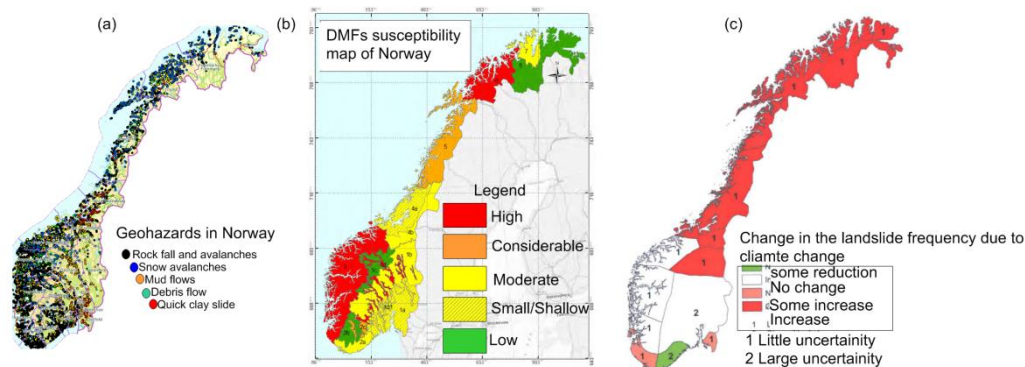
Figure 1.1: (a) Geohazard challenges in Norway based on www.skrednett.no; (b) DMFs susceptibility map of Norway illustrated using a recent study carried-out by NIFS (2014); (c) Change in landslide frequencies due to climate change suggested by NVE (2011)

In order to identify the locations where climate trigged debris flow can actually occur, various quantitative or semi-quantitative approaches have been proposed to assess the relations between climatic conditions and debris flow. These approaches are often focused on rainfall intensity based models, while other vital parameters such as the size of the catchment area, snow melting and the geomaterials itself are often less-attacked. Geomaterials, which are found in a great variety in the nature, exhibits different thermo-hydro-mechanical properties depending on their types and origin. Whether a

geomaterial may be subjected to debris flow depends on, among other, it's resilience towards climate factors, infiltration properties, water retention properties under drying and wetting process, pore water pressure built-up, content of fine grains and the degree of saturation.

For the purpose of predicting the mobility of debris flow and coming up with effective countermeasures to mitigate its damage, multiple physical models have been developed. As a complex material debris flow exhibits many aspects of phenomenology: dilatancy, internal friction, cohesion, fluidization and particle segregation, but in most theories only the first three are successfully incorporated. Practically, the role played by the fluid is usually treated parametrically, not kinematically. Solid-fluid interaction (including pore pressure generation and dissipation) plays a significant role in the entrainment and detrainment processes involved in moving debris.

Until now, only few experiments have been devoted to the significance of pore-liquid pressure built-up, and its correlation to flowing velocity and grain size on a limited range of samples. In view of this, this study shall help in improving our understanding of the pore pressure built-up in moving debris.

1.2. Objective of the study

Debris flow is a vast topic and it is not possible to cover all aspects in one master thesis. Therefore, this master thesis is dedicated to the following issues.

- To develop a co-axial cylinder experiment system and evaluate its effectiveness.

- To explore the effects of solid fraction concentration on pore pressure built-up, and the relationship between pore pressure built-up and flowing velocity for this series of tests.

- To examine pore pressure build-up in samples of varying fine grain content.

- To verify the existence of decline of pore pressure build-up after certain velocity, and to explain it in terms of sediment dilatancy (particles break-up).

- To observe pore pressure built-up profile at differing heights, and dissipation process in varying samples.

1.3. Methodology

The capricious timing and disastrous nature of debris flows hamper direct collection of detailed data. Scientific understanding has thus been gleaned mostly from qualitative

field observations and experiments and models (Iverson 1997). As a master thesis project the available time and resources are also limited. Therefore a portable apparatus that can be fabricated and operated without great effort seems appropriate. Starting from the schematic illustration of a double-cylinder equipment (Wang and Sassa 2003) the co-axial cylinder, mixing component and data-collecting system have been developed. Tested samples were from the mixture of Geo&Geo sand and Tiller silt available in the laboratory. Apart from two main series of tests, some trial tests were also conducted to gain knowledge of suitable sample height, sensor data quality and centrifugal correction.

1.4. Scope of the study

After assembling the apparatus, several trial tests were ran to check the torque capacity of motor, and to improve the mixing rods, the test procedure and the sensors' performance. Afterwards, two series of samples with varying solid fraction concentration and silt content were performed.

Before extracting meaningful information from test results, three pure water tests were conducted to provide basis of centrifugal correction as sensors on the wall were believed to give reliable data. Out of the purpose of verifying dilatancy as reason of floating ratio decline, sieving tests and hydrometer tests were performed before and after experiment.

1.5. Limitations

First of all, coaxial cylinder apparatus used for debris mixture has seen few precedents (Wang and Sassa 2003) though coaxial cylinder rheometer has been common in obtaining rheological parameters of pure liquid or suspension. Thus detailed documentation of apparatus, procedures, and potential challenges are unavailable. For this reason much effort has been paid and some errors or imperfections were realized only after the event.

The adopted Geo&Geo Sand and Tiller Silt are classified as medium sand and coarse silt respectively. Clay content in the silt is merely 2.1% by weight, rather low compared with 6.76% in M30 from Wang & Sassa's work. Therefore discrepant results could be expected.

In explaining decline of pore pressure built-up hypothesis of sediment dilatancy was proposed. And in many tests the transitional stage was observed. However when did particle start to break and at what rate, and what really happened during transitional stage remained unclear unless micro phenomena were made visible.

Finally major findings of this study were not examined against in-situ events.

1.6. Structure of the thesis

Structure of the next chapters will be discussed as follows:

Chapter 2: presents literature reviews on the definition, classification and process of debris flow, influencing factors of debris mobility, and studies on the physical modeling of debris flow.

Chapter 3: presents the set-up of the coaxial cylinder apparatus, experiment procedure and plan, tested materials, and supplementary tests as well.

Chapter 4: presents the original results, centrifugal corrections, corrected results and analysis.

Chapter 5: concludes the main messages draw from the study. Shortcomings of this work are also discussed.

Chapter 6: presents some recommendations towards future work on this topic.

Appendices: presents the drawings of coaxial cylinder apparatus, plots of data-saving duration, and plots of test results that are not incorporated in main content.

2.Literature review

2.1. General

Debris flow, as a specific subject of study, has derived from the regime of landslide(Stiny 1910). Hereafter the definition of debris flow has received considerable attentions from varying researchers to distinguish it from mud flow, debris avalanches and debris flood(Jakob and Hungr 2005). A systematic compilation of the main hyperconcentrated flow classifications has been proposed by G. Lorenzini and N. Mazza (2004) in which debris flow is endowed differing meaning according to criteria adopted.

Nowadays it is widely accepted that debris flow is a gravity-driven mixture of various size of grains and abundant water that usually develops from slope failure or intensive precipitation in unprotected mountain area. Confined in channel-like region, debris flow may exhibit great variation of composition and kinetics depending on topography, sediment condition etc.

In order to come up with effective counter-measures, a thorough understanding of the post-failure mobility of debris flow is necessary(Hungr 1995). Among the influencing factors the role play by water and entrainment condition of bed have been revealed of great significance through remarkable experiments and analytical examinations (Wang and Sassa 2003, Iverson 2013).

2.2. Debris flow: definition

Debris flows occur when masses of poorly sorted sediment, agitated and saturated with water, surge down slopes in response to water infiltration and gravitational attraction. Both solid and fluid forces vitally influence the motion, distinguishing debris flows from related phenomena such as rock avalanches and sediment-laden water floods. Different from avalanche and flood, whose behavior is dominated by solid grain forces and fluid forces respectively, debris flow is marked by the collaboration of solid grain forces and fluid forces as solid particles and liquid take approximately similar fraction by volume (Iverson 1997). Based on multiple laboratory experiments on samples from Colorado, O'Brien and Julien (O'Brien and Julien 1985) classified hyperconcentrated flows, according to the properties determined by sediment concentrations, as water floods, mudfloods, mudflows (debris flow) and landslides (Fig. 2.1). Sediment concentration by volume in debris flow varies between 45% and 55%; silt and clay particles, which may constitute to a large content, make debris flow extremely viscous and give it notable yield stress, enabling debris flow to hold considerably sized clasts in suspension.
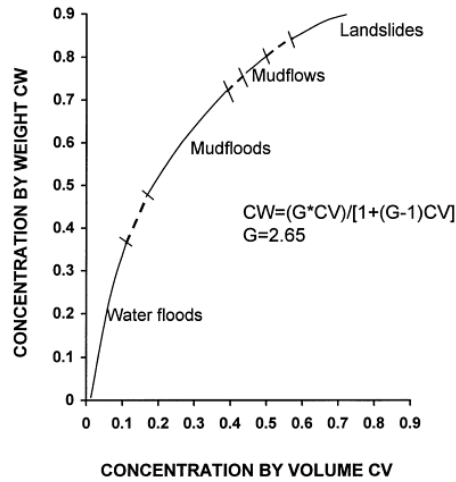
Figure 2.1: The classification of hyperconcentrated streamflows in the study of O'Brien and Julien (Julien and Lan 1991)

Besides, debris flow is also characterized by low plasticity (plasticity index < 5%) in sand and finer fractions, particle size segregation (Takahashi, Nakagawa et al. 1992), bouldery front and lateral levee as well (see Fig. 2.2). In current study the thin bottom layer (Fig. 2.3) under severe shearing, where fine grains concentrate, is of interest.
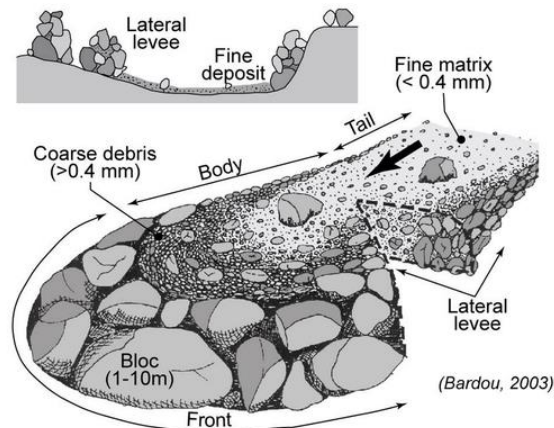
Figure 2.2: Configuration of a typical debris flow (Bardou, Ancey et al. 2003)
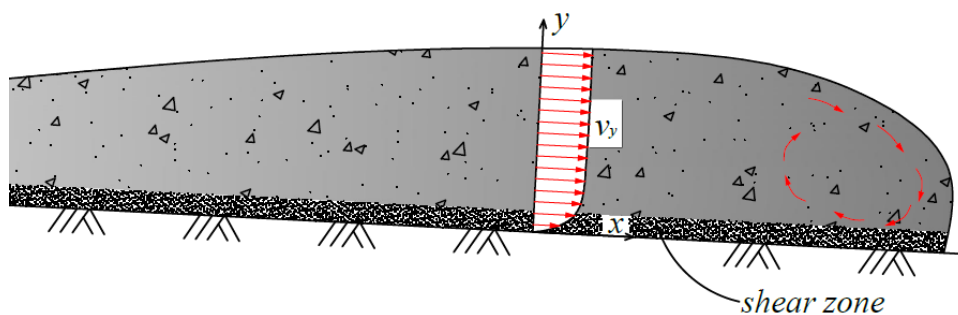
Figure 2.3: Illustration of shear zone

2.3. Classification of debris flow

Majorly based on solid concentration, fine grain content and consequently the dominating stresses, debris flow has been classified by many researchers (Coussot 1992, Takahashi 2014) as: stony type, viscous debris flows, and turbulent-muddy type, though other terminologies may be adopted. "Stony debris flows" refer to those in which the stress is dominated by particle collision, "turbulent muddy debris flows" correspond to those that are dominated by turbulent mixing stress, and "viscous debris flows" are characterized by viscoplastic stress.

2.3.1. Stony type debris flow

Stony debris flows are majorly featured by a large proportion of large particles. Dynamics of this type debris flow is dominated by grains collisions and inertial stress. When collisional effects are not damped by viscosity, grains give rise to collective phenomena, such as segregation, force percolation or shock waves (Herrmann and Luding 1998).

In order to account for the decisive effects of large particles in the simulation of stony debris flow, two-phase models, considering a continuum fluid phase, and large sediment particles, such as boulders, as a non-continuum phase, are more appropriate and competent in delivering accurate results (De Wrachien and Brebbia 2010).

2.3.2. Viscous debris flows

When the fine grains in interstitial liquid account for a significant proportion in the entire solid fraction, and it is mainly composed of cohesive solids, the fluid becomes highly viscous slurry. In addition to the large viscosity of the slurry, the dense content of coarse particles adds to the apparent viscosity of the whole material. Therefore, in such a debris flow, the viscous stress is more prominent than the stresses caused by the inter-particle collisions and/or the macro turbulent mixing. This kind of debris flow is called as the viscous type.

A dimensionless coefficient B_a initially defined by Bagnold R. A. (1954) and later named by Hill H. M. (1966) as Bagnold number is commonly used to differentiate stony and viscous debris flows. It reads

$$B_a = \frac{\rho_s d_s^2 \lambda_s^{\frac{1}{2}} \dot{\gamma}}{\mu_f} \tag{2.1}$$

In which

μ_f = the dynamic viscosity of the liquid $(Pa \cdot s)$;

$\dot{\gamma}$ = shearing rate (s^{-1});

ρ_s = density of solid particles (kg/m³);

d_s = characteristic diameter of the grains (mm);

λ_s is the linear grain concentration at point y in flow and is related to the volume concentration by

$$\lambda = \frac{1}{\left(c_0/c\right)^{1/2}-1} \tag{2.2}$$

where

c = volume concentration of solids in flow;

c_0 = volume concentration of solids at closet possible packing.

As illustrated in Fig. 2.4 viscous debris flows are denoted by $B_a < 40$, and stony debris flows by $B_a > 450$ with a transition region for $40 \leq B_a \leq 450$.
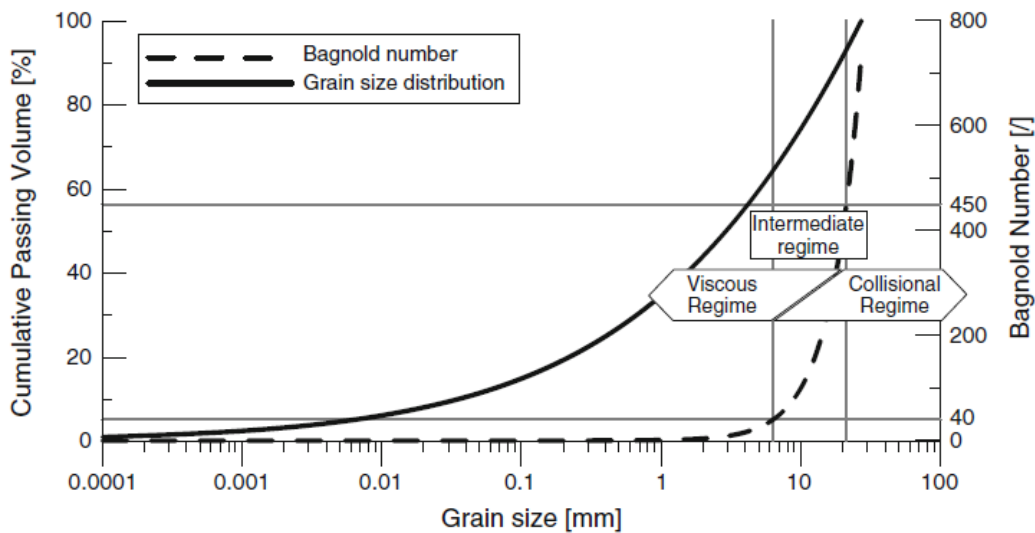
Figure 2.4: A typical grain size distribution and its effect on the dynamics of the mixture. The Bagnold number is calculated with $\mu_f = 1.0\ Pa \cdot s, \rho = 1000\ kg/m^3, \lambda = 1, \dot{\gamma} = 100\ s^{-1}$ (Leonardi, Wittel et al. 2014)

2.3.3. Turbulent-muddy type debris flow

This type of debris flows is, even though they may contain many large boulders, primarily comprised of fine content. Usually the fine fraction (clay) is large enough (say about 10%) for the solid-water mixture to form an interstitial fluid that significantly reduces inter-particle collision and have the mixture manifest liquid behavior (Coussot and Meunier 1996). Frequent occurrence of this type of debris flow is often seen in volcanic ash cover area as it can be easily eroded even by a slight rainfall. Samples collected in the channel works downstream in the Nojiri River of Japan indicate that the concentration of solids with median diameter 0.3-1 mm is up to 54-72% by volume. Despite that, the fluidity measured with Manning's formula resembles that of plain water flow(Takahashi 2014). In terms of mechanical characterization,

this type of debris flow is mainly described with the help of Bingham model(Coussot and Meunier 1996).

2.4. Process of debris flow
2.4.1. Initiation

Three prerequisites must be fulfilled to initiate a debris flow: failure of the mass, sufficient water to saturate the mass, and conversion of gravitational potential energy to internal kinetic energy to transform the localized sliding motion to widespread deformation(Iverson 1997).

The mechanical sources of debris flow initiation can be analyzed as three types:

1. Water runoff. Flowing surface water may erode gully deposit when shear strength of deposit is exceeded by shear stress due to increased water level and/or seepage force. The concentration of solids in the water flow later becomes dense enough to be called debris flow;
2. Landslides. Landslides may be mobilized into debris flow when sufficient water, either stored in the slide or supplied from outside, exists.
3. Dam breach. The collapse of a dam in river or gully may lead to catastrophic surging debris flow.

Water runoff induced debris flow

Water infiltration and a flowing layer on the surface happen when there is rainfall or flood. This may cause erosion as the shear strength τ_r of deposit is surpassed by shear stress τ. Assuming τ and τ_r to distribute linearly normal to the terrain surface, Takahashi (1978, Takahashi 1981) described the six cases (Fig. 2.5) corresponding to the relative arrangement of those two lines as shown below. In cases (1), (2), (3), and (4), τ is larger than τ_r, therefore debris flow may arise
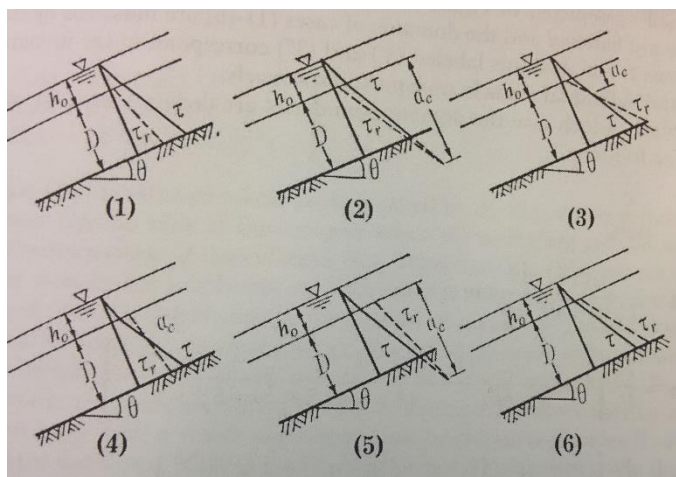
Figure 2.5: Relative relations of shear strength and shear stress

By conducting large scale experiments in the USGS debris flow flume, Mark E. Reid et al. (1997) observed disparate patterns of initiation when the slope is exposed to these three hydrologic conditions: localized groundwater inflow, prolonged moderate-intensity rainfall, and high-intensity rainfall. Groundwater inflow and prolonged moderate-intensity rainfall lead to sudden, complete failure whereas moderate-intensity sprinkling gives rise to retrogressive, block-by-block failure.

Landslides induced debris flow

Two types of landslides occur on the occasion of intensive rainfall; the shallow landslide of about 1~2m thick and the deep-seated one of several tens of meters thick. The shallow landslide stores plenty of water in itself and is also facilitated by a high flood runoff discharge. As a result, under the severest rainfall it is easily transformed into a debris flow almost from the instant of the initiation of motion. The mechanism of mobilization of shallow landslides can further be classified into three subcategories: monolithic, retrogressive and progressive (see Fig. 2.6).
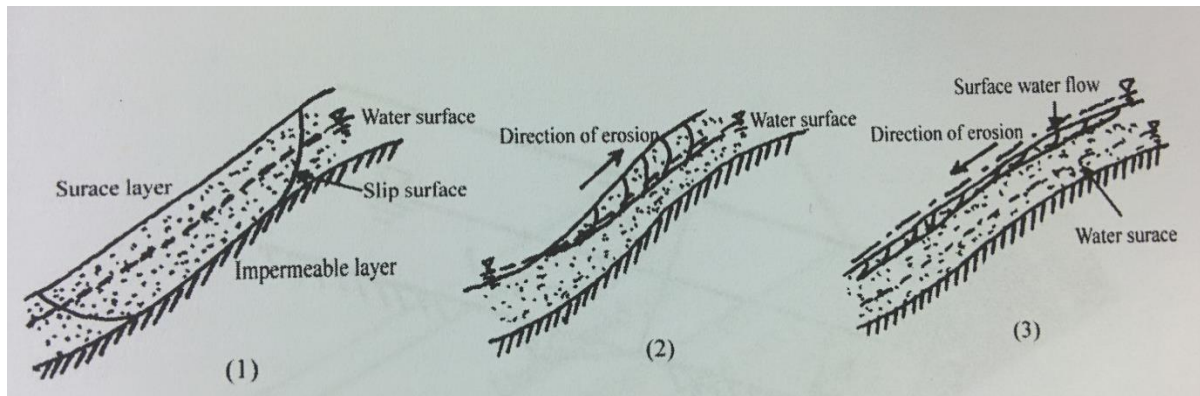
Figure 2.6: Subcategories of shallow landslides

As pointed out by Takahashi (2014) deep-seated landslide needs a relatively long time before the ground water level rises high enough to make the earth block unstable. Hence, it often occurs later than the time of strongest precipitation. Due to that reason, the mechanism for the transformation into debris flow would be entirely different from that of a shallow landslide.

Dam breach induced debris flow

There are two types of dams that may trigger hazardous debris flow; natural dam and check dam. Natural dams are formed after huge amount of masses fall by chance into a river channel and choke the river. Check dams are constructed by human beings to mitigate the momentum of debris flow and collect debris material. The failure of natural dams are often attributed to overtopping and/or seepage, while check dams collapse are commonly due to the failure of barrier structure.

2.4.2. Transportation

After initiation the debris flow starts to flow mainly under the influence of gravity. The flow velocity, debris depth and run-out area are often of great interest as they indicate the magnitude of potential damage. Multiple factors are found to contribute to the dynamics of debris flow during transportation. Among them topography stands as an apparent and dominant element. The steeper the path is, the more turbulent the flow will be, also the entrainment capacity. In the contrary, the deposition effect will be more prominent. As the laboratory studies conducted by Espen Fiskum (Fiskum 2014) displayed, the lateral confinement of flow path facilitates debris transportation markedly.

The significance of deposit conditions have been analytically proved and experimentally documented regarding debris volume increase and flow velocity. Sassa and his colleagues (Sassa, Fukuoka et al. 1998, Wang and Sassa 2002, Wang and Sassa 2003, Sassa, Fukuoka et al. 2004) examined the pore-pressure built-up and maintaining effects of several samples of fine sand mixed with varying content of medium silt. The results revealed that the finer-grain content was not only capable of increasing the peak excess pore pressure but keeping the pressure at a considerable high level for about one day, long after the stoppage of debris flow. Abrupt excess pore pressure rise was observed (Wang and Sassa 2002) even in dense sands, which was found to be triggered by grains crushing.

After performing eight large scale experiments in the USGS debris-flow flume, Mark E. Reid et al. (Reid and Iverson 2011) concluded that the largest debris-flow volume growth and speed increase occurred when debris flows traveled over wetter sediment. Undrained loading and loose sediment contraction were proposed as the mechanisms. Initial stress states and shearing history of sediment were also reported (Wang and Sassa 2002) to have effects on flow dynamics during transportation.

2.4.3. Deposition

Deposition of debris flows normally happens after lateral confinements end, which give rise to widespread-flowing, then depositional lobes form where the frictional resistance of coarse-grained flow fronts and margins is sufficient to terminate progress of the trailing, liquefied debris. In some cases (Iverson 2014) no marked variations of topography exist, but merely depletion of kinetic energy due to friction and collision brings the debris flow to a halt.

The mechanism of the stoppage and deposition have been less treated, despite its significance to the prevention of hazard. Hooke (1967) conducted experiments in which small alluvial cone were built, and found the angles of cone slopes to lie between 4° and 8°, values that are about average for natural cones rich in cobbles and boulders. Johnson (1970) derived the equation of the snout curve as below assuming plastic behavior of the debris material. As indicated in Fig. 2.7, x axis is made parallel to debris bottom and pointing to the direction of movement, while y axis is normal to the bottom and pointing upwards.

$$x = -\frac{\tau_y}{\gamma_d} \ln\left[\cos\left(\frac{\gamma_d}{2\tau_y}y\right)\right] \qquad (2.3)$$

where γ_d is the bulk density of the plastic substance, and τ_y is the yield strength.
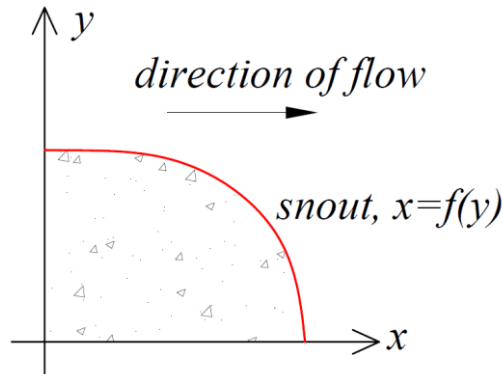
Figure 2.7: Illustration of the snout curve

Takahashi & Yoshida (1979) presented the criterion for the stoppage of debris flow in situation where the slope of the channel abruptly changes to a flatter value without expansion of width. According to the criterion, the snout would stop when

$$tan\theta < \frac{tan\alpha}{tan\varphi} tan\theta_u \qquad (2.4)$$

where θ and θ_u are the angles of downstream and upstream channel respectively; α is the dynamic angle of internal friction, while φ is the internal friction angle.

Empirical methods for predicting deposition area have been studied by many researchers. Among them, the one proposed by Iverson et al. (Iverson, Schilling et al. 1998) has received wide attention. Their method, which originates from the study of volcanic lahars; correlates lahar volume (V) with valley cross-sectional area (A) and planimetric area (B) inundated by employing two semi-empirical equations (V–A and V–B), has inspired multiple endeavors to establish similar correlations suitable for debris flow in certain area (Crosta, Cucchiaro et al. 2003, Griswold 2004, Berti and Simoni 2007).

2.5. Influencing factors of debris flow mobility

Debris flow mobility refers to the flow behaviors during motion which, from a microscopic point of view, may incorporate kinetics and reverse segregation of grains, interaction between interstitial liquid and solid fraction, and entrainment process etc. As manifestations of above behaviors, flow velocity, momentum, turbulence, and indirectly the traveling distance constitute the observable characteristics of debris flow dynamics.

Numerous factors influence debris flow mobility. Geological condition provides important implications towards initial void ratio, initial stress states and stress history of source material. Topography characteristics, for instance elevation, path gradient, lateral confinement and

singularity, decide the potential energy available, and its rate of conversion into kinetic energy as well. In addition, pore pressure built-up together with entrainment have been demonstrated by researchers (Wang and Sassa 2003, Iverson, Logan et al. 2010) to have significant impacts on the mobility of debris flow.

2.5.1. Pore pressure built-up

At the stage of initiation, increased pore pressure could be induced by intensive and prolonged rainfall, eventually resulting in slope failure. While in the process of transportation, floating of coarse grains, contraction of loose or medium dense sands, along with grain crushing are found to be the most important triggers leading to the built-up of high pore pressure, most often corresponding to liquefaction.

After presenting the three typical cases of pore pressure generation at slip plane (Sassa 1988), Sassa and Wang (2002) conducted a series of ring shear tests in a specially designed apparatus to examine the pore pressure built-up and the behavior of sand under undrained condition when subjected to long shear displacement especially at the initiation stage. Through their tests, the effects of relative density, stress state and shear history were inspected. In order to facilitate the interpretation of liquefaction as a consequence of high pore pressure built-up, "static liquefaction resistance" (R_L), proposed by Kramer and Seed (1988) to analyze the condition needed to trigger liquefaction in ring shear tests and the "brittleness index" (I_B) proposed by Bishop (1967) to analyze the consequence of liquefaction, were introduced (see Fig. 2.8). Finally, it was revealed that an optimal density existed at which the undrained brittleness index had a minimum value; meantime, the undrained brittleness index turned greater with increasing initial normal and shear stresses, but decreased with shear times.
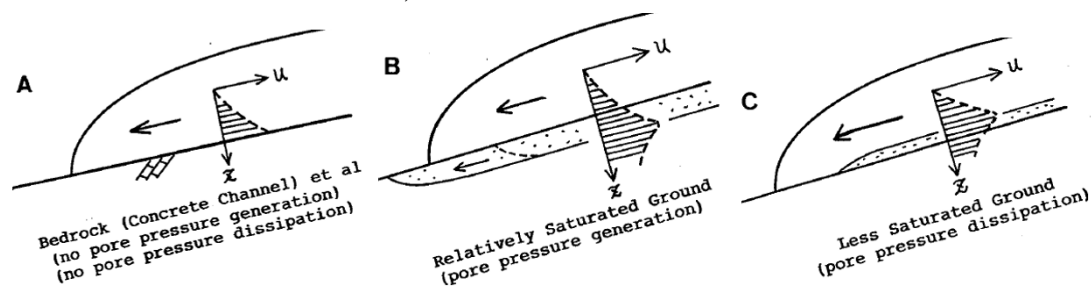
Figure 2.8: Three typical cases of pore pressure generation at slip plane (Sassa 1988)
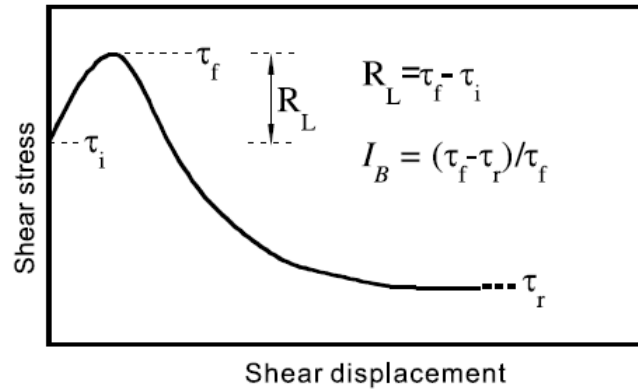
Figure 2.9:Shear stress - shear displacement curve in the ring shear test (Wang & Sassa, 2002)

In a subsequent experiment of these two authors (Wang and Sassa 2003), they further investigated the effects of grain size and fine-particle content in pore pressure built-up and maintaining. By employing a double-cylinder apparatus (Fig. 2.10), in which saturated samples were rotated at varying speed, and pore pressure was measured at the bottom. Measured pore pressure was found to increase with velocity. In addition, sample with finer grains or greater fine grain content floated more easily, and higher pore pressure could be maintained during motion (as shown in Fig. 2.11, where S7 denotes a relative coarse sand, S8 denotes the finer one, M10/20/30 are names given to sands mixed with 10%, 20% and 30% of clay by weight respectively). Remarkably, peak value of excess pore pressure generated in sample with 30% of clay content lasted for about 5 hours after the stop of rotation before experiencing appreciable drop (see Fig. 2.12).
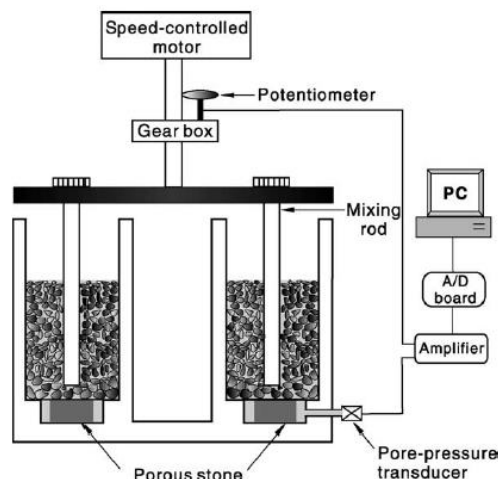
Figure 2.10: Arrangement of double-cylinder rotating apparatus (Sassa 1988)
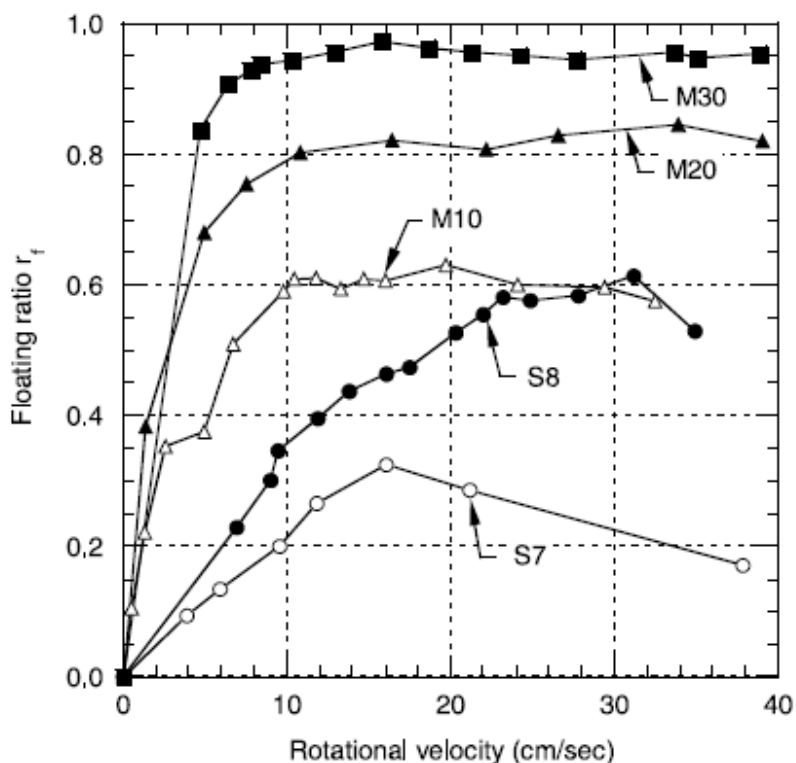
Figure 2.11: Floating ratio versus rotational velocity for different samples (Wang and Sassa 2003)

Floating ratio referred in the diagrams is a dimensionless indication of excess pore pressure that was defined by Sassa (1998), and is formulated as:

$$r_f = \frac{u - u_s}{\sigma_t - u_s} \qquad (2.5)$$

where, u is measured pore pressure; σ_t is total normal stress, u_s is the static water pressure, or the initial water pressure measured before the rotating.
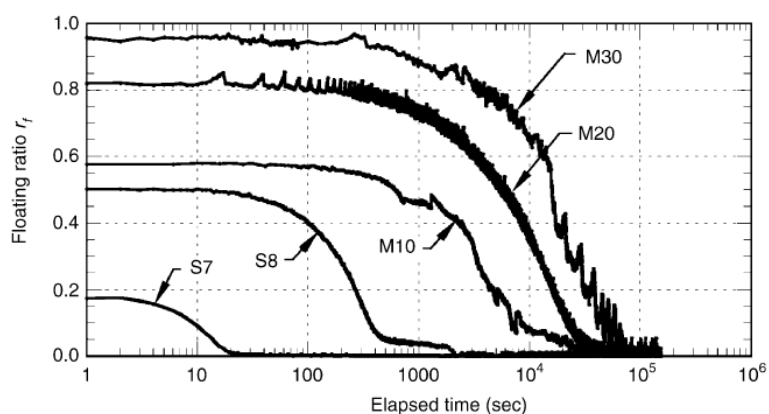
Figure 2.12: Time series of floating ratio after the rotation ceased for different samples (Wang and Sassa 2003)

As shown in Fig. 2.10 that floating ratios of samples S7 and S8 reached their crest before apparent drop was instantly observed at greater rotational velocity. In the authors' opinion, this phenomenon was attributed to the fact that when mixing rods rotated too fast (relative to the moving mixture) the mixture could not move with rods, and subsequently was subjected to shearing, which reduced the agitation of grains, and thus caused reduction in pore pressure. Alternatively, dilatancy due to the break-up of particles may turn out to be a more convincing explanation.

For samples containing various content of clay, floating ratio tended to stabilize after certain velocity, and no significant decreasing trends were detected over the whole velocity range. Explanation concerning this discrepancy was not offered in their paper.

2.5.2. Entrainment

Entrainment is commonly defined as incorporation of solid and fluid boundary material from channel path and/or bank. When debris flows grow by entraining sediment, they can become especially hazardous owing to increased volume, speed, and run-out (Reid and Iverson 2011).

By conducting large-scale flume experiments, Mark E. Reid et al (2011) explored the profound role played by entrainment in changing the mobility of debris flow. They found that when debris flows traveled over relatively dry sediment, net scour was minimal, but when debris flows traveled over wetter sediment (volumetric water content > 0.22), debris flow volume grew rapidly and flow speed together with run-out were enhanced. In an effort to link water content with elevated pore pressure, an abrupt transition of entrainment behavior was revealed with water content threshold as 0.22 (Fig. 2.13). When peak basal pore pressure ratio approached unity, the sediment would liquefy, leading to reduced basal friction and enhanced debris flow mobility.
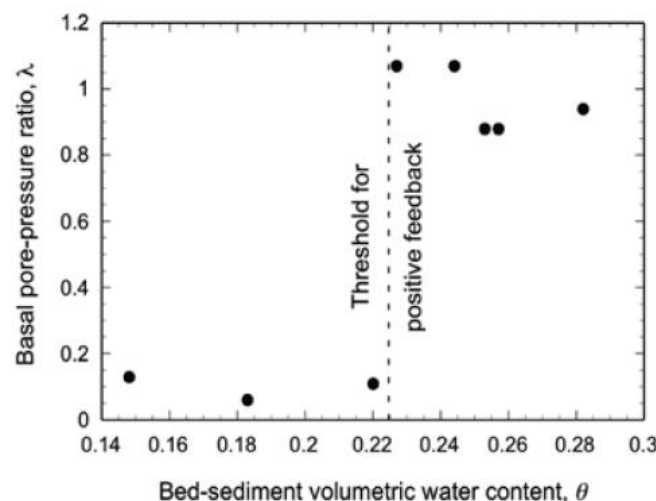
Figure 2.13: Peak basal pore-pressure ratio, $\lambda(= p/\sigma)$, as a function of bed-sediment volumetric water content, θ Mark E. Reid et al (2011)
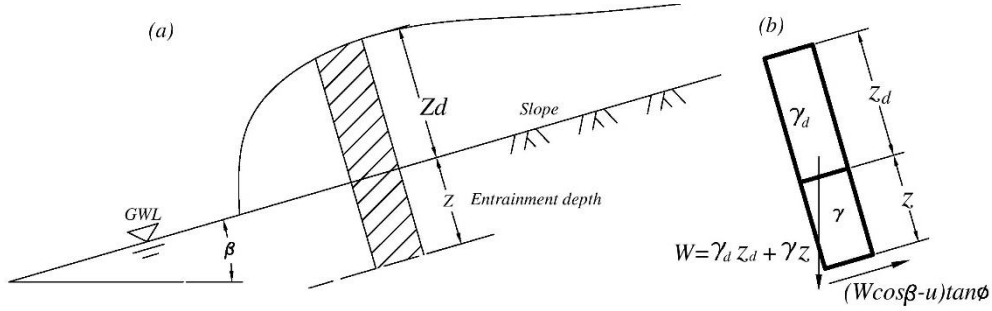
Figure 2.14: (a) Schematic representation of a saturated bed over-ridden by a debris flow, showing a slope-normal column of unit length and width. (b) Forces acting on the column in (a) (adapted from O. Hungr et al. (2005))

Entrainment was first attacked in terms of erosion depth. Among the pioneers Takahashi (1978) assumed slope-parallel seepage and uniform flow, combined with instant drainage, so that the pore fluid is hydrostatically pressurized and flowing in a steady-state regime. Taking a typical column of a unit base area for stability analysis (Fig. 2.14), the shear stress at the column base equals:

$$\tau = W sin\beta = (\gamma_d z_d + \gamma z)sin\beta \tag{2.6}$$

where γ is the saturated unit weight of bed material, and γ_d is the bulk unit weight of the debris.

The normal total stress equals:

$$\sigma = W cos\beta = (\gamma_d z_d + \gamma z)cos\beta \tag{2.7}$$

The pore pressure at the bottom base is:

$$u = \gamma_w(z_d + z)cos\beta \tag{2.8}$$

The shear strength of the bed material is given by the cohesionless Mohr-Coulomb shear strength law, in which φ is the friction angle:

$$S = (\sigma - u)tan\varphi \tag{2.9}$$

At shear failure $S = \tau$, i.e.

$$(W cos\beta - u)tan\varphi = W sin\beta \tag{2.10}$$

Substituting eq. X, Y and Z into eq. and solving for z:

$$z = z_d \left[\frac{\frac{\gamma_d}{\gamma}\left(1 - \frac{tan\beta}{tan\varphi}\right) - \frac{\gamma_w}{\gamma}}{\frac{\gamma_w}{\gamma} - \left(1 - \frac{tan\beta}{tan\varphi}\right)} \right] \tag{2.11}$$

The formula shows that a certain amount of entrainment is possible for any value of γ_d less than $\frac{\gamma_w}{1-\frac{tan\beta}{tan\varphi}}$, with more dilute flows causing instability to greater entraining depths. For fully developed debris surges, whose bulk density approximates the density of the bed material (i.e., $\frac{\gamma_d}{\gamma} \approx 1$), no entrainment will be predicted with these assumptions, if the bed itself is inherently stable.

Instead of assuming a steady seepage condition, a more realistic assumption would be that the bulk weight of the debris flow $\gamma_d z_d$ will be transferred to pore-water through undrained loading, hence building high pore pressure within the deposit materials. Thus the new expression for u is:

$$u = (z_d \gamma_d + z\gamma_w)cos\beta \qquad (2.12)$$

Following the same steps that have led to equation 2.11 a new formula is obtained (Hungr, McDougall et al. 2005):

$$z = z_d \left[\frac{-\frac{\gamma_d tan\beta}{\gamma \, tan\varphi}}{\frac{\gamma_w}{\gamma}-(1-\frac{tan\beta}{tan\varphi})} \right] \qquad (2.13)$$

Equation 2.13 together with equation 2.11 are plotted in Fig. 2.15 and interpreted by O. Hungr et al. (2005) as follows. Compared with formula 2.11, the new formula predicts entrainment depth for all values of γ_d. The actual value of the unstable depth may lie somewhere between the two extremes depicted in Fig. 2.15 although it is likely closer to the undrained condition (solid lines) than those for the drained condition.
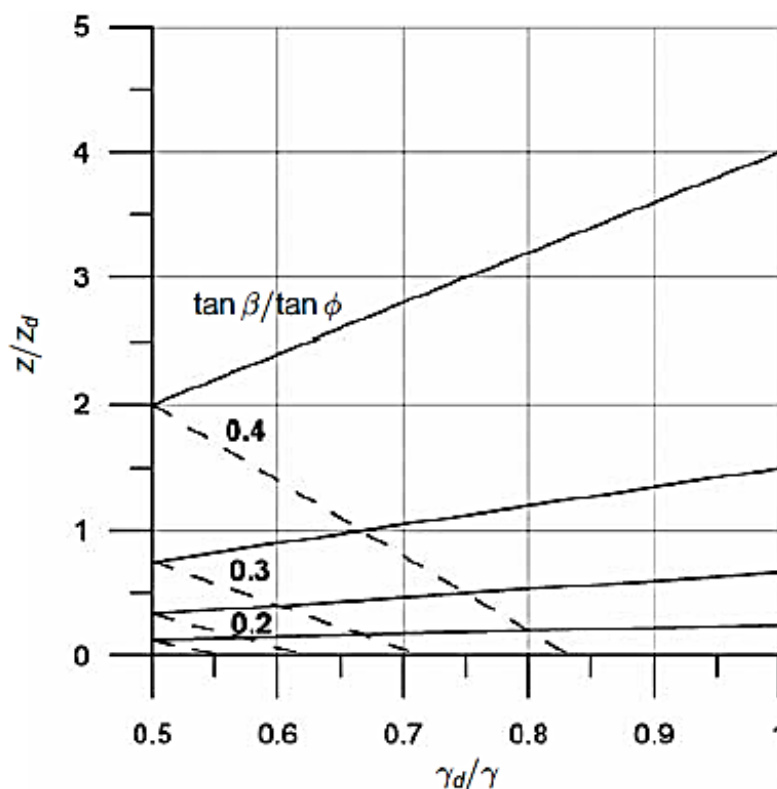
Figure 2.15: Erosion depths predicted by equation 2.11 (dashed lines) and equation 2.13 (solid lines)

Contrary to the proposition by Takahashi (1978) that saturated bed sediment fails en masse, Mark E. Reid & Iverson observed from a series of flume experiments that entrainment occurs through rapid (5-10 cm/s) progressive downward scour.

The estimation of entraining depth is regarded difficult and subjective for erodible base channels. Hungr and McDougall (2005) suggested that theoretical means of estimating erosion depths in such cases is not practically useful, and recourse must be directed to subjective judgement or empirical relations.

2.6. Debris flow modeling

Analogous to any other engineering challenge, analytical modeling, numerical modeling and physical modeling have long been dedicated to the study of debris flow. Numerous branches can be named for each approach. In this study the emphasis is directed to its physical modeling, which would help draw a most related background for current study.

Detailed data on the dynamic characteristics of debris flow are needed to interpret and predict debris flow behavior. However due to the sporadic and irreproducible nature of in-situ events, direct measurements or observations are difficult to obtain. Alternatively various physical models have been developed, of which flume test, rotating flume (mill) test have received the most attention.

2.6.1. Rotating flume (mill)

In USA, Brown S. M. (1992) first proposed the use of rotating flume in his master thesis, later Huizinga (Huizinga 1993, 1996) continued the development and verified it using Non-Newtonian Fluids. In Austria, R. Kaitna and D. Rickenmann (2007) constructed a similar apparatus (Fig.2.16), but had it systematically equipped with more sensors and tracing techniques. The apparatus allows generating and observing stationary surges of materials ranging from viscous slurries to granular flows for an extended time period. With it the normal stress and shear stress at bottom, flow depth/surge geometry, mean flow velocity, surface velocity and pore fluid pressure could be well documented. Two simple methods were proposed to allow the flow parameters for a Bingham model to be estimated.

Figure 2.16: Side view of the rotating flume (Kaitna and Rickenmann 2007)

Norifumi Hotta (2011) from University of Tsukuba, Japan employed a small rotating mill (4 cm wide and 20 cm in diameter, see Fig. 2.17) to assess the validity of related constitutive equations (Hotta and Miyamoto 2008). The results implied that a Reynolds stress model best fitted the experimental data when only larger particles were present, whereas an "infiltration flow" drag model best fitted the data when only smaller particles were present. A combination of the two models provides the best fit to the full dataset. The data are inconclusive as far as determining which model might work best for real debris flows with a great diversity of particle sizes.
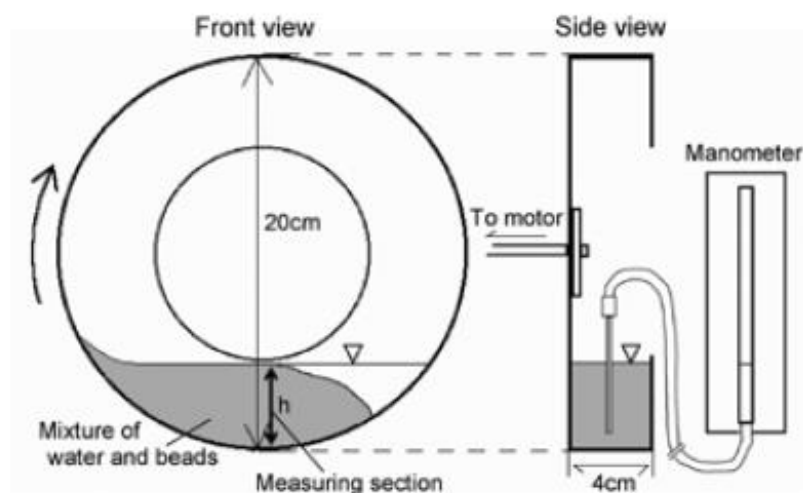
Figure 2.17: Sketch of the rotating mill (Hotta 2011)

Excess pore water pressures at different depth were also examined with size-varied glass and plastic beads under some chosen speeds. In Fig. 2.18 materials of 6 mm glass beads and 6 mm plastic beads were found to generate more or less linearly distributed excess pore pressure, which is indicated by p_f, and made dimensionless by dividing by unit weight of water (ρg). Excess pore pressure was also found to monotonically increase with rotational speed in both materials.
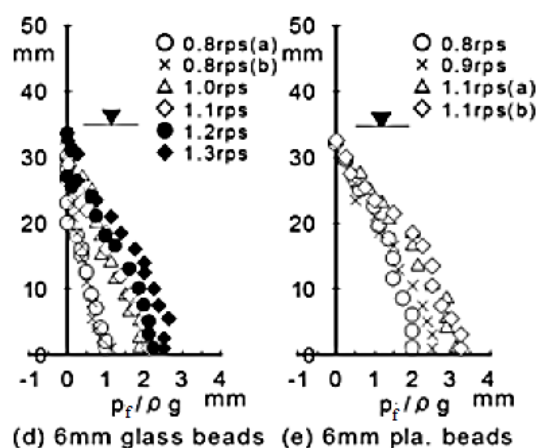
Figure 2.18: Excess pore water pressure distributions (Norifumi Hotta (2011)). Here "rps" is short for "revolution per second"

According to Kaitna and D. Rickenmann (2007) the main advantage of employing a rotating flume is the possibility to establish stationary conditions over an extended period of time. On the other hand the flow behavior is more complex due to flume bottom curvature, and the effect of wall friction may be more significant compared to a conveyor belt apparatus. Despite of this,

rotating flume or rotating mill is still capable of offering meaningful insights into the characteristics of debris flow at a relatively low cost.

2.6.2. Flume test

Compared with rotating flume (mill) tests, flume tests are able to simulate natural debris flow events more closely. Among the flume tests that have been conducted (Rickenmann, Weber et al. 2003, Wang and Sassa 2003, Papa, Egashira et al. 2004, Reid and Iverson 2011) the flume constructed at U.S. Geological Survey (Iverson, Logan et al. 2010) is worth detailed introduction due to its large scale and systematic influential tests performed.

The flume is composed of a reinforced concrete channel 95 m long, 2 m wide and 1.2 m deep that slopes at 31 degrees, an angle typical of terrain where natural debris flows originate (Iverson, Costa et al. 1992). A nearly horizontal concrete runout plate is located at the base (Fig. 2.19). Various types of sensors are able to be installed, thus enabling the measurements of soil-moisture, pore pressure, total pressure, flow height, traveling velocity, entrainment process. According to its website (http://pubs.usgs.gov/of/2007/1315/), 146 experiments had been conducted from 1992 to 2013, with subjects involving roughness and geometry of flow path, entrainment of bed sediment, effect of fine content material (loam), and counter-measures. As an effort focusing on the significance of bed sediment to mobility of debris flow, Mark E. Reid et al (2011) performed eight entrainment experiments and two control experiments without any erodible sediment in the flume (Iverson, Logan et al. 2010). Among their discoveries, they concluded that entrainment occurred through rapid progressive downward scour (see Fig. 2.20) rather than by mass failure at depth as postulated by Takahashi (1978, Takahashi 1981).

Figure 2.19: Flume at USGS
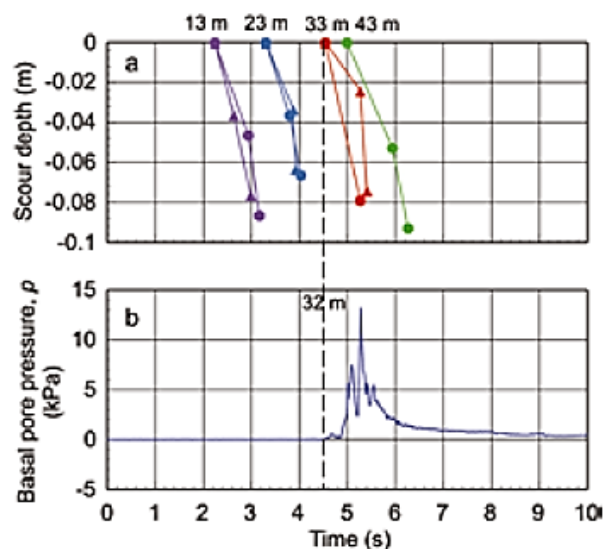
Figure 2.20: (a) Scour depth detected at 4 measurement sections down the flume during an entrainment experiment with wet bed sediment (water content=0.25). (b) Basal pore-pressure

responses at the 32-m measurement section. Vertical dashed line denotes arrival of debris-flow front at 32-m section. Experiment date: 13 May 2008. Mark E. Reid et al (2011)

2.6.3. Coaxial-cylinder test

As mentioned previously, coaxial cylinder test has been employed by Sassa (1988) in the pursue of relationship between pore pressure built-up and rotational velocity of samples with varying grain size distribution and fine grain content. Another sketch of their apparatus is given in Fig. 2.21 below. This apparatus turned to be successful and efficient for that purpose. However, the solid fraction concentrations of samples were not documented, the grain size coverage was also confined, and the maximum rotational velocity employed was relatively low compared with real event. These facts actually outline what can be achieved in future work.
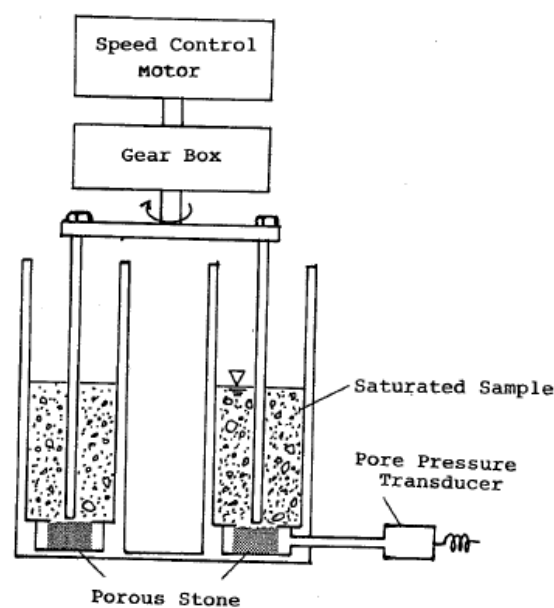
Figure 2.21: Apparatus to measure pore pressure in moving saturated soils. Size of sample box: 14 cm (inside), 30 cm (outside) in diameter, 28 cm in depth. Sassa (1988)

3. Coaxial cylinder apparatus set-up

3.1. Apparatus configuration

Starting from the schematic illustration of the apparatus (see Fig. 2.10) from K. Sassa and G. H. Wang (Sassa 1988, 2003), a coaxial cylinder equipment, mixing component, data-collecting system were designed and fabricated. Besides, a programme was written dedicating to controlling. Fig. 3.1 presents an overview of the apparatus.
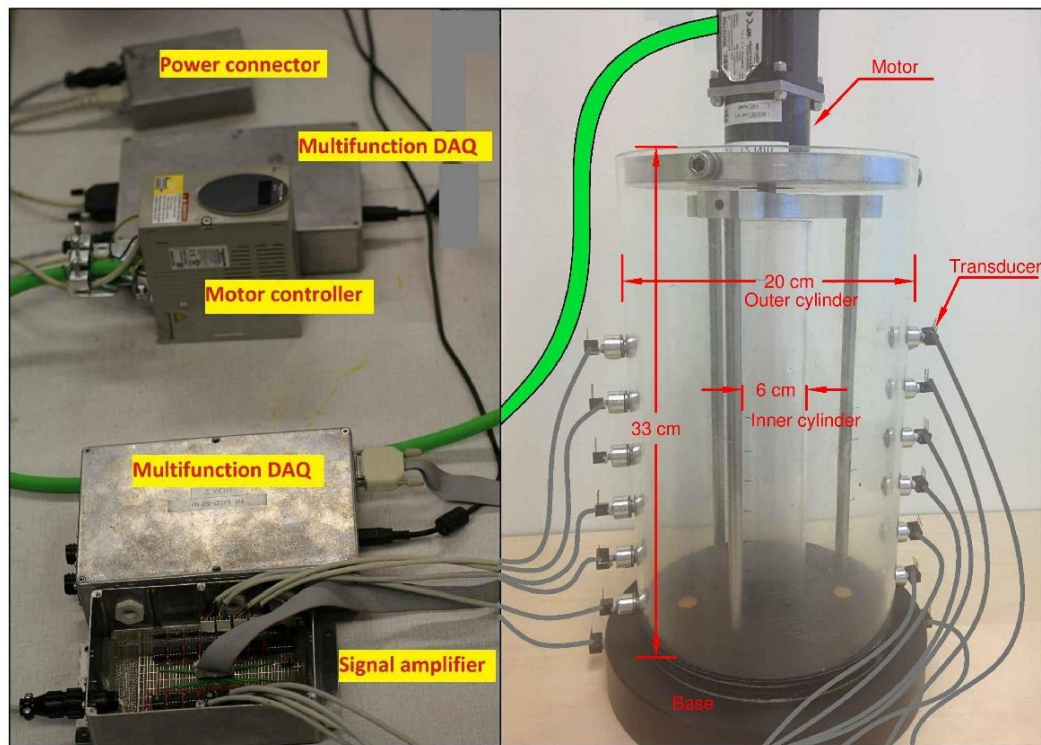
Figure 3.1: Apparatus set-up overview

3.1.1. Coaxial cylinder

The coaxial cylinders (see Fig. 3.1), a 20 cm outer one and 6 cm inner one, sit on a rubber base. Two O-rings were mounted between cylinder and base to prevent leakage. Six pairs of holes were drilled on opposite positions of the wall of outer cylinder at varying heights for installation of transducers. Two holes and connecting ducts were drilled on the base to allow for placing of porous stones and sensors. The rotating component is mounted on outer cylinder with three screws. The fixing plate was shaped for the purposes of reducing weight and retaining the possibility of interference during rotation as indicated in Appendix 1.

3.1.2. Mixing component

Two sets of rods were fabricated, of which the shorter ones are to be used for tests with deposits. Screw threads were carved on the ends of each rod; three sleeves with total length 7 cm can be connected to rods enabling adjusting of rod-length (Fig. 3.2). The distance of rods from cylinder center is 6.25 cm.

The step motor has 200 steps per revolution, and torque capacity 1.2 $N \cdot m$, which can be geared up to 5 times. Maximum rotational velocity was set as 200 rpm, much lower than the limit 1000 rpm and equivalent to translational velocity 1.3 m/s. Speed increment was given as 3 rpm (1.962 cm/s).

The torque capacity was found insufficient for Geo&Geo sand mixture higher than 10 cm in trial test, therefore in formal tests the heights of mixture were kept lower than 10 cm. Despite of this, extra care must be paid during the insertion of rods, and some successful experiences are worth being mentioned here.

- Before inserting rods, the motor should be turn on at low speed (3 rpm);
- The rods must be lowered slowly. Only when stability is achieved at one depth can they be lowered further. This could be explained as excess pore pressure was generated upon agitation of rods, and that reduced effective stress and subsequently shear strength;
- It's better to have the base fixed or held by someone else during insertion, because the revolving rods may cause the whole cylinder to rotate.
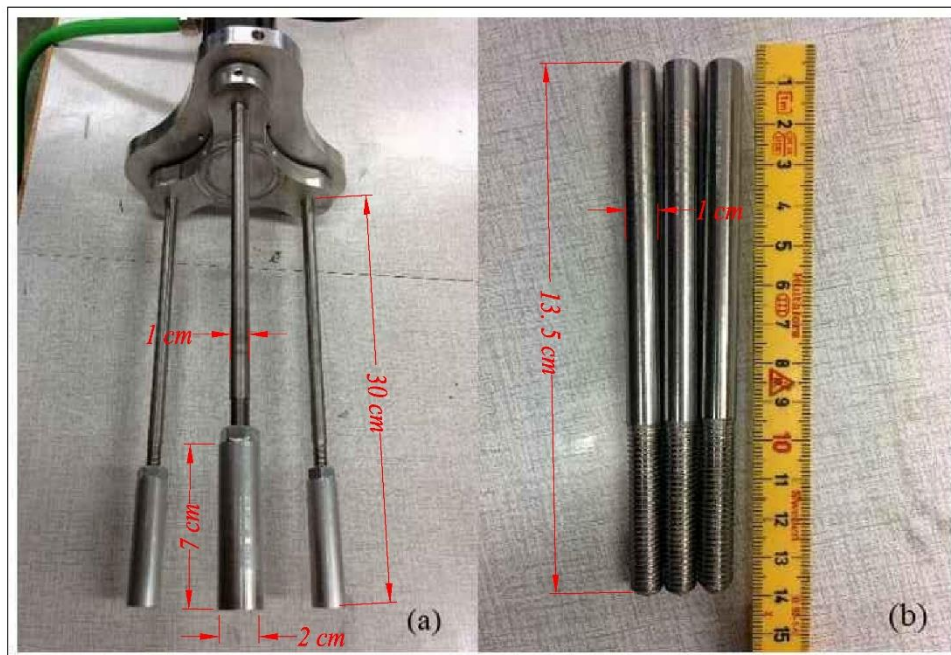
Figure 3.2: (a) Long rods and sleeves; (b) short rods

3.1.3. Data collection system

Up to 6 sensors could be installed on each side of the wall with 4 cm apart. The lowest ones are 0.5 cm above the base. Initially the wall-sensor was connected to a screw which was home to porous stone (Fig. 3.3). During trail tests the porous stone was found prone to being stuck and lead to unreliable readings. This may be because the pore size of porous stone was larger than the finest grains. Thereafter an alternative method was proposed, which exclude the porous stone and added an oil-filled hose linking the sensor and screw. The chosen saturation oil was

paraffin liquid that is high in viscosity, thus assuring full-filling of the hose during installation. The cavity of screw is prone to trapping air bubbles when wet sample is poured inside quickly or the water content of sample is too less (when sample with porosity 0.4 was tested, many air bubbles were observed after careful dumping). Though this has remained as a concern, satisfactory results have been extracted using this technique judged by coincidence of readings from sensors of the same height. After experiment, the cavity of screw was found filled with well-graded sand under visual inspection (Fig. 3.4), which most probably behaved as natural porous stone.

Figure 3.3: Porous stone and sensor screw
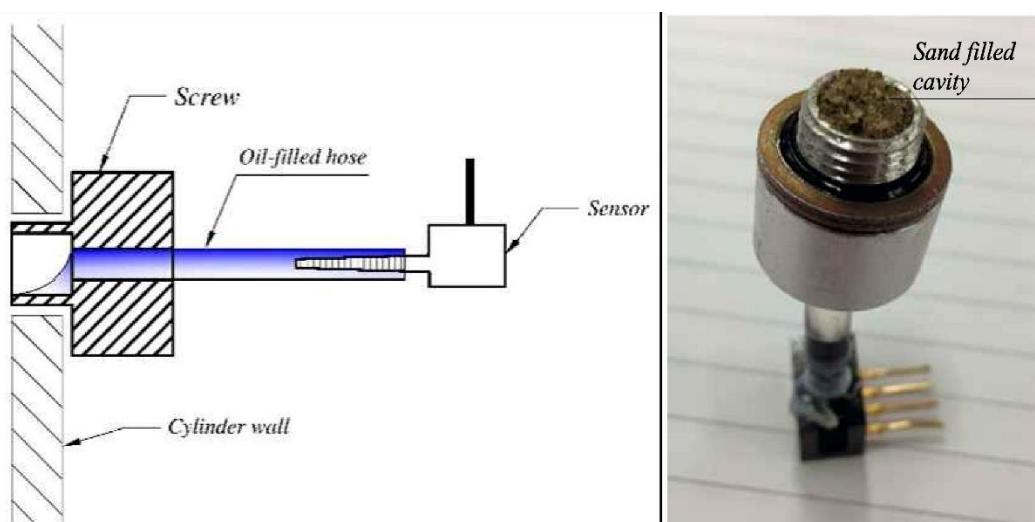
Figure 3.4: (Left) Alternative sensor-connecting technique; (right) screw cavity filled with sand

The sensors are linked to signal amplifier with 4-channel cables. At the end of sensor, the red cord should be positioned at right side when facing sensor rear (Fig. 3.5). At the end of signal amplifier, the red cord should be with the red plug as indicated by arrow. Each time before test, the two holes on base were injected full with paraffin liquid.
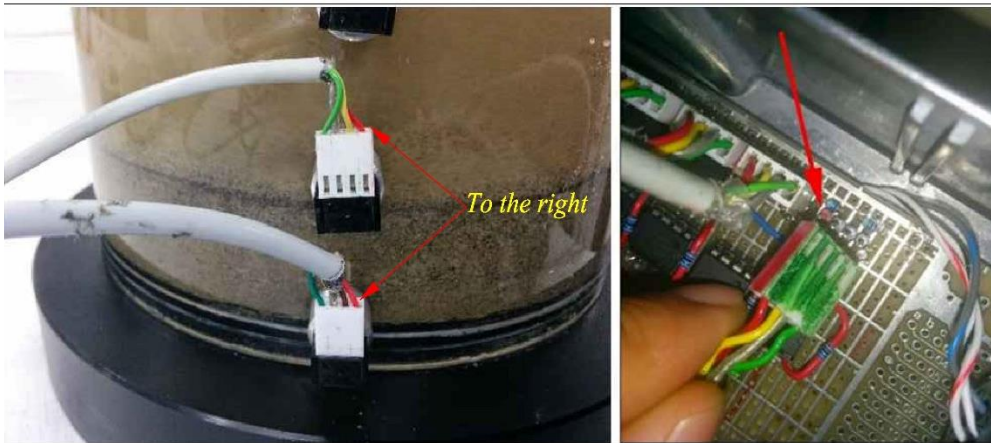
Figure 3.5: Cable connection: sensor end (left); signal amplifier end (right)

3.1.4. Controlling programme

The programme written in LabVIEW 2014 consists of two modules (see Fig. 3.6). One is the main function module, which offers manual speed control, manual/auto switch button, data saving options (start button, file name, time interval), pore pressure measurements and indicators, and raw data measured in mV; the other is auto module which defines the auto test sequence with speed, duration and data-saving option for each step.
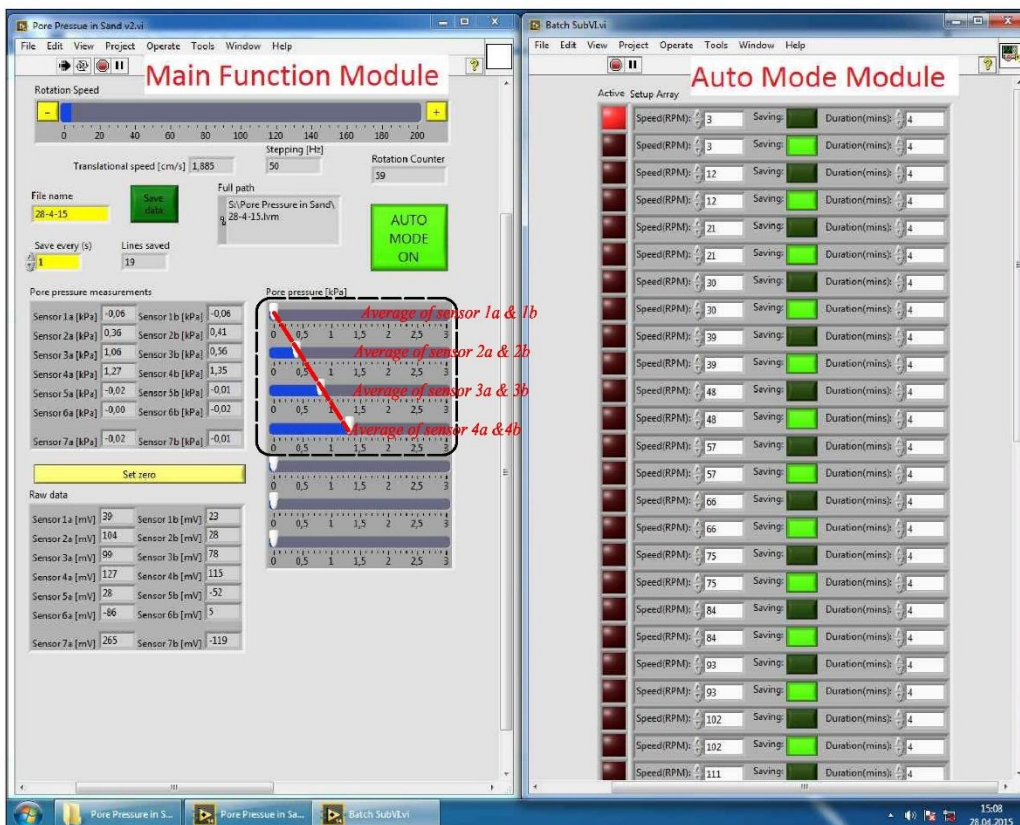
Figure 3.6: Controlling programme

3.2. Tested material

Before this study many debris flow flume experiments had been performed by previous master students Espen Fiskum et al. at NTNU hydrodynamics laboratory. Therefore the initial intention was to use their material in my experiment and attempt to build connections. However trial tests shew that their sand was not suitable for two reasons. First, less significant excess pore pressure could be generated when compared with Geo&Geo sand which has been used for the basic course "Geoteknikk og geologi". Comparison of excess pore water pressure before centrifugal correction is presented in Fig. 3.8 where both tests were carried with same height and approximately identical solid concentration (50%). The other reason is their sand is too coarse and stiff, causing insertion of rods rather time-consuming (it took around 1.5 hours in trial test) for depth beyond 8 cm in addition to the high frequency of getting stuck.

Moraine silt taken at Tiller, Trondheim had been used to increase the fine grain content in Geo&Geo sand. Clay content in this silt is about 2.1% by weight, which is considerably lower than that in Loess used in Wang, G. H., & Sassa, K. (2003)'s experiments. Grain size distributions of the materials used in this study and Wang, G. H., & Sassa, K. (2003) are plotted in Fig. 3.7. Grain properties of employed samples with varying silt content are compiled in Table 3.1.

Table 3.1: Properties of employed samples with varying silt content

Sample	Silt	$C50S20_{h8}$	$C50S33_{h8}$	$C50S40_{h8}$	$C50S50_{h8}$	$C50S80_{h8}$
Mean size D_{50} (mm)	0.0495	0.3454	0.2630	0.2176	0.1406	0.0832
Effective size, D_{10} (mm)	0.0074	0.0319	0.0158	0.0138	0.0119	0.0089
Coefficient of uniformity, c_u	10.87	13.62	23.38	23.61	20.59	11.28
Coefficient of curvature, c_c	0.49	2.28	2.06	1.97	2.07	0.560
Specific gravity, G_s	2.647	2.723	2.711	2.704	2.694	2.666

As pointed out by Casagrande (1940), during shear deformation, the void change of sand in loose state and in dense state tends to produce the same ''critical void ratio''. Therefore, it can be inferred that the tested sand will tend to arrive at the same void ratio after reaching steady-state movement, no matter whether the sand was initially in loose or dense state. Therefore, in this test series, all the samples were placed by means of wet mixture without tamping, and the effects of initial void ratio were not examined.
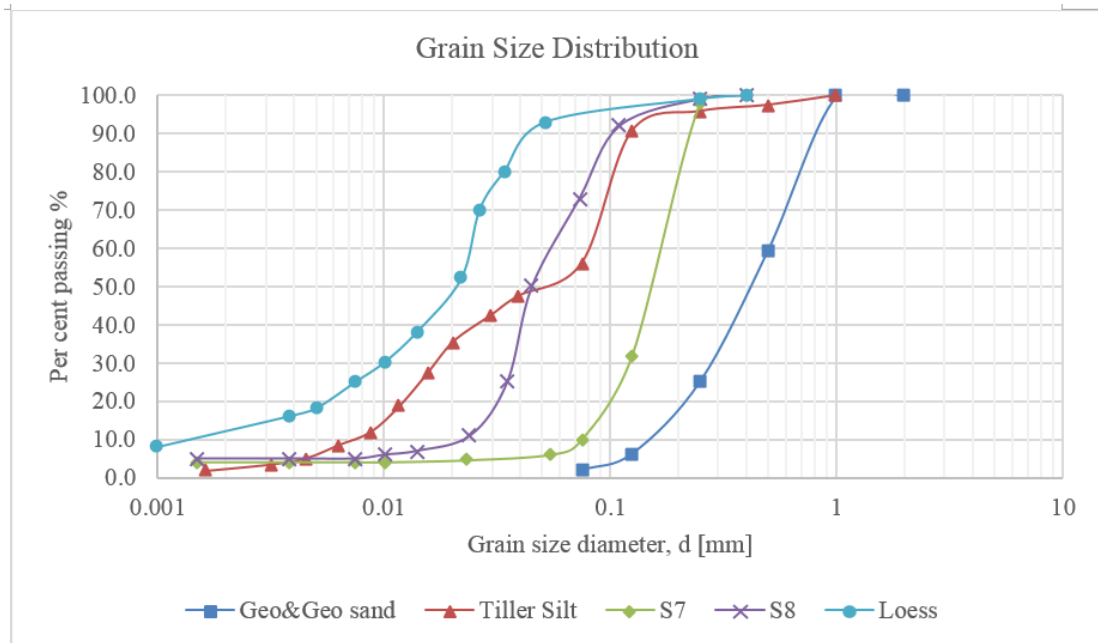
Figure 3.7: Grain size distribution of used and referred materials
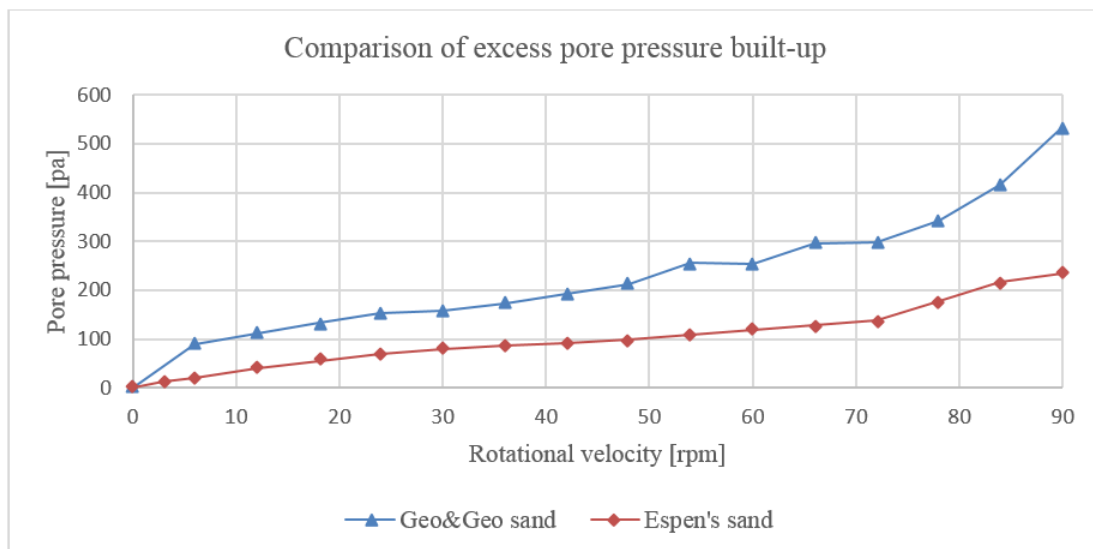
Figure 3.8: Comparison of excess pore pressure built-up in Geo&Geo sand and Espen's sand (data from the average of sensors 3a&3b)

3.3. Naming of tests

Take test "$C50S40_{h8}$" as an example, here "C" stands for solid fraction concentration by volume, "S" represents silt content by weight in solid fraction, "h" is to indicate the height of mixture by centimeter in apparatus. Collectively "$C50S40_{h8}$"means test of sample with 50% solid fraction volumetric concentration, 40% silt content, and a height of 8 cm.

When it comes to the up limit of solid concentration, 50% seemed appropriate. Initially tests $C60S20_{h10}$, $C64S50_{h7.5}$ and $C66S50_{h8.2}$ were performed. In test $C60S20_{h10}$ up to half height

sand was not stirred up, and it prevented pore pressure readings of sensors 2a, 2b, 3a and 3b from gaining meaningful increase until speed 174 rpm, when 60% pore pressure increase was seen (Fig. 3.9). In tests $C64S50_{h7.5}$ and $C66S50_{h8.2}$ the mixture behaved more in a plastic manner than fluid.

For several tests deceleration process was performed after maximum rotational speed was reached. These tests are denoted with a star on the right corner of the name, such as $C50S20^*_{h8}$.
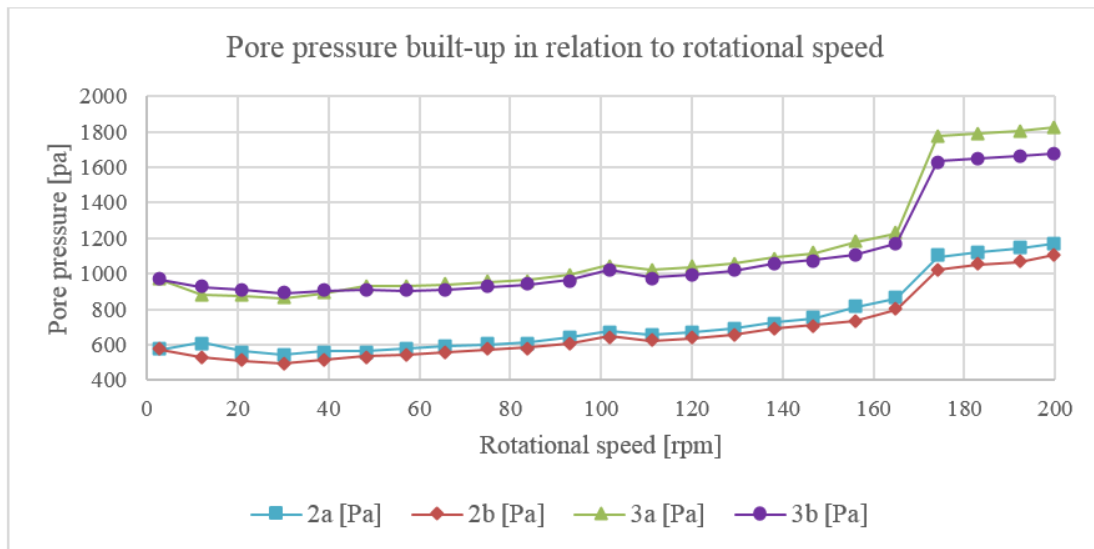
Figure 3.9: Pore pressure built-up in $C60S20_{h20}$

All tests conducted in coaxial cylinder are presented below in Table 3.2, of which samples with varying solid fraction concentration are classified into test series one; samples of varying silt content are classified into test series two.

Table 3.2 Summary of Coaxial Cylinder tests

Solid concentration	Silt content 20%	Silt content 33%	Silt content 40%	Silt content 50%	Silt content 80%	Silt content 100%	Other
30%	$C30S20_{h10}$						
40%	$C40S20_{h6}$ $C40S20_{h10}$						• Tests of Espen Fiskum's sand;
50%	$C50S20_{h8}$ $C50S20_{h8}{}^{*}$ $C50S20_{h10}$	$C50S33_{h8}$	$C50S40_{h8}$	$C50S50_{h8}$	$C50S80_{h8}$ $C50S80_{h8}{}^{*}$	$C50S100_{h8}$	• Centrifugal correction tests.
60%	$C60S20_{h8}$ $C60S20_{h10}$						
>60%				$C63.6S50_{h7.5}$ $C66S50_{h8}$			

Test series one (spans Silt content 20%). Test series two (spans Silt content 33%–100%).

• Test $C50S20_{h8}$ and $C50S20_{h10}$ exist in both series.
• Superscript star in some names, for instance, $C50S80_{h8}{}^{*}$ indicates a repeated test.

3.4. Experiment procedure

A standard coaxial-cylinder experiment consists of following steps:

- Calculate weights of every dry material and water;
- Weigh and mix dry material in a container, add distilled water to an amount which is about 200 ml less than needed; mix until the material becomes homogeneous. The left water is to be used to flush the container and cylinder's inner wall;
- Put the container into vacuum fest for at least 30 minutes to have the mixture saturate;
- Saturate the holes, porous stones at base, and the hoses that connect sensors with screws with paraffin liquid by using syringe;
- Install sensors onto the wall and base;
- Connect data-collecting cables; start the programme and set zero values after 20 minutes;
- Dumping the mixture slowly and carefully into the apparatus. It is recommended to dump more fluid at the beginning, which would form a liquid surface from bottom and help exclude air in screw cavities. Direct dumping of mixture onto sensors should be avoided;
- Flush residual mixture in the container and cylinder wall with the spared about 200 ml water;
- Rake and mix the mixture carefully. Wait for about half an hour until hydrostatic state is reached inside the mixture. Name the log file and start to record the static readings;
- Turn on the motor at speed 3 rpm; slowly insert rods into position then install and tight the three screws on top plate. It is better to fix the apparatus during insertion as rotating rods may cause the whole apparatus to rotate;
- Seal openings on top plate and unused screw holes on the wall with membrane;
- Maintain the speed 3 rpm for 5 minutes (later it was modified as : "maintain the speed 3 rpm until the excess pore pressure caused by rods insertion fully dissipates"); start to save data for another 4 minutes;
- Proceed to next velocity level, and maintain for 5 minutes before data saving; or switch to auto mode which has defined a test procedure beforehand;
- After the completion of all speed levels and dissipation, copy the log file for analysis. Turn off the motor and data-collecting system. Detach cables, lift motor and rods;
- Dump the mixture into a barrel for later grain size distribution test;
- Clear the apparatus and sensor screws.

Great consciousness must be paid to exclude air bubbles from hoses and porous stones. Though, porous stones in the base remained challenging to reach full saturation with syringe. An efficient alternative is desired. Cautions are also needed for cables, especially the red cords, to ensure right and sound connectivity.

3.5. Supplementary tests
3.5.1. Centrifugal correction tests

During rotation centrifugal force contributed to pore pressure built-up. In order to gain net excess pore pressure induced by sediment particles agitation, centrifugal force's contribution must be quantified.

As illustrated in Fig. 3.10, an mixture element close to outer wall with infinitesimal width dR and area dA is subjected to centrifugal pressures p from outer cylinder, where the sensor sits, and p' from mixture interface, normal stresses from above and beneath σ_a and σ_b. The resulting centrifugal force acting on this element is

$$F_c = (p - p')dA = dp \cdot dA = \rho \cdot dA \cdot dR \cdot \omega^2 \cdot R \qquad (3.1)$$

which gives

$$p = \rho \cdot \omega^2 \int_0^R R dR + C = \frac{1}{2}\rho \cdot \omega^2 \cdot R^2 + C \qquad (3.2)$$

where C is arbitrary constant.

As a result, when ω and R are fixed, p is linearly correlated with suspension density ρ.

In order to quantify its influence three tests with pure water of height 8 cm, 10 cm and 12 cm were performed. Excess water pressure in test of 8 cm water is plotted in Fig. 3.11. It can be seen that sensor 2a&2b, 3a&3b gave consistent readings, indicating uniform centrifugal effect at different height. Sensor 4a experienced ever-reducing but reasonable values due to the existence of vortex, while sensor 4b presented apparently unreliable data. For specific test, readings of sensors 2a, 2b, 3a and 3b should be multiplied by the density ratio of suspension to water before being used for correction. No need of correction for sensors 4a and 4b due to the absence of centrifugal force at base.
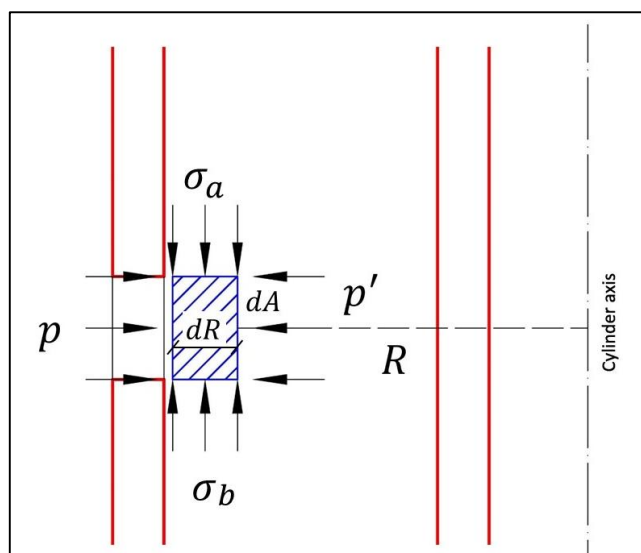
Figure 3.10: Illustration of centrifugal pressure
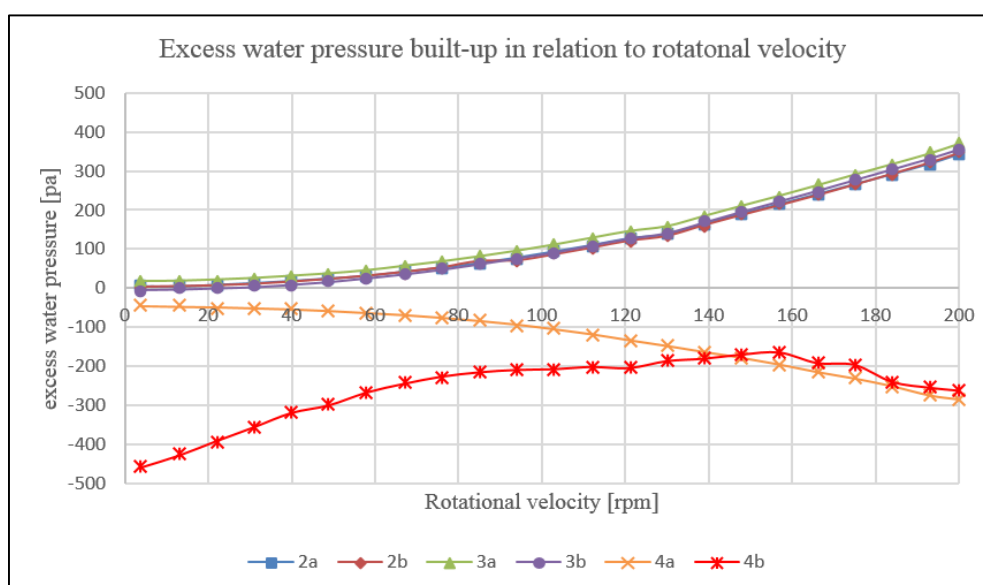
Figure 3.11: Water pressure measured in centrifugal correction test (water height 8 cm)

3.5.2. Data saving duration

As stated previously 5 minutes were allocated to reach stabilization of sensor reading. This choice was based on two trial tests $C50S20_{h8}$ and $C50S80_{h8}$, which would lend persuasive basis for samples of varying solid fraction and silt content respectively.

In both tests 9 minutes continuous readings were recorded for rotational velocities: 3 rpm, 39 rpm, 84 rpm, 120 rpm, 165 rpm and 200 rpm. The results showed that 5 minutes were sufficient to reach stable readings. For speed lower than 39 rpm in test $C50S20_{h8}$ a decreasing trend was detected (Fig. 3.12), which was caused by initial excess pore pressure dissipation and will be

explained in detail later in section 4.2.2. It was also observed that the higher the speed was, the shorter time was needed to reach stable (see Fig. 3.13 and Fig. 3.14). The rest figures are attached in Appendix B.
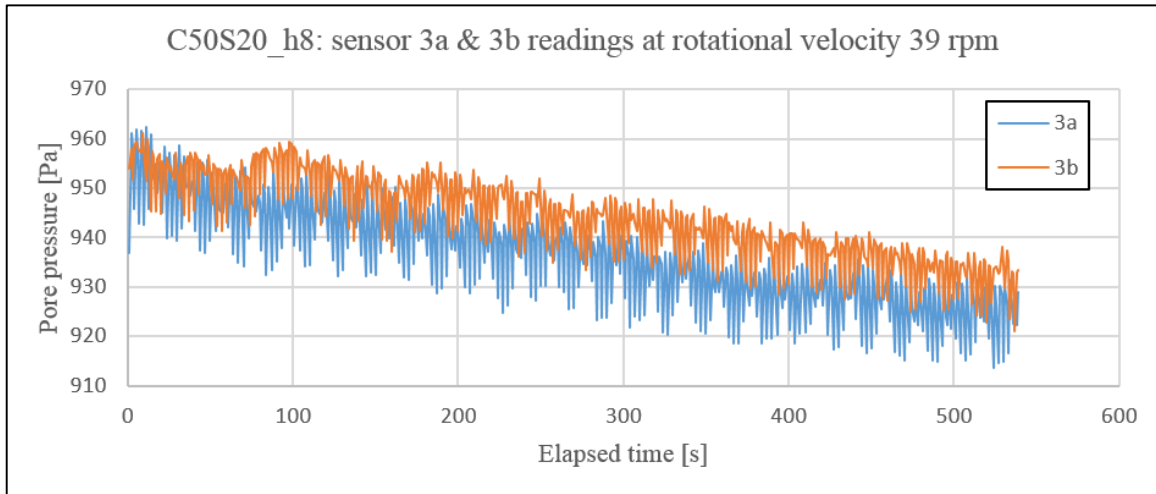
Figure 3.12: Pore pressure recorded over time at velocity 39 rpm in C50S20_h8
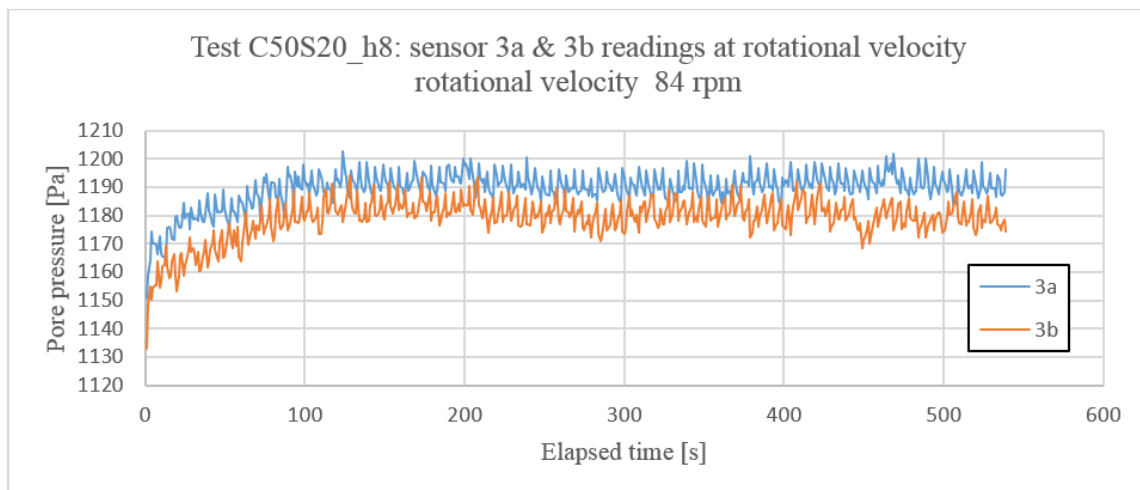
Figure 3.13: Pore pressure recorded over time at velocity 84 rpm in C50S20_h8
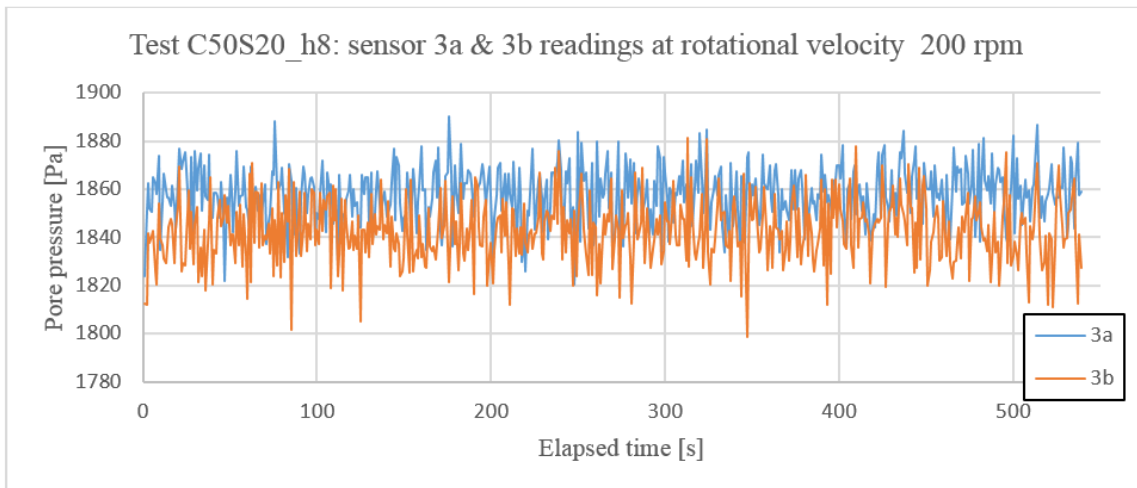
Figure 3.14: Pore pressure recorded over time at velocity 200 rpm in C50S20_h8

4.Results and discussions

4.1. General

In total 15 coaxial cylinder tests (including repeated ones) have been performed and classified into two series. Among the data generated from experiments, the net excess pore pressure due to particles-liquid interaction and floating ratio are of the most interest. Pore pressure measured at base and different heights on the wall enable better interpretation of pore pressure distribution when compared with merely sensors at base. In some tests inconsistent results were observed from sensors 4a and 4b. In addition, under high rotational velocity centrifugal forces acting on the wall took up a considerable proportion of pressure measured. As a result, the quality and representativeness of sensor readings must be evaluated, and the centrifugal effects must as well be quantified before any meaningful information can be drawn.

Three tests with pure water were conducted to provide reference for centrifugal correction. Some interesting results and plausible explanations are presented. Afterwards the results were compared with experiment results from Wang & Sassa (2003) in terms of consistency and discrepancy.

4.2. Original results

Some representative tests of the two series are chosen here to present original pore pressure measured at all sensors.
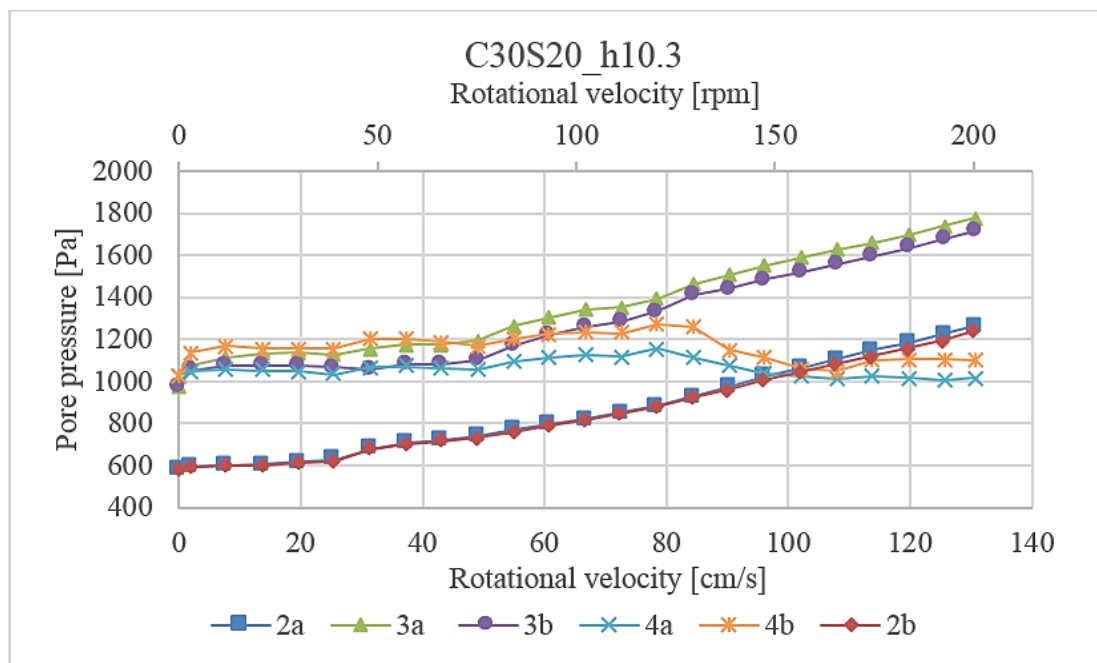
Figure 4.1: Original pore pressure in relation to rotational velocity in test $C30S20_{h10.3}$
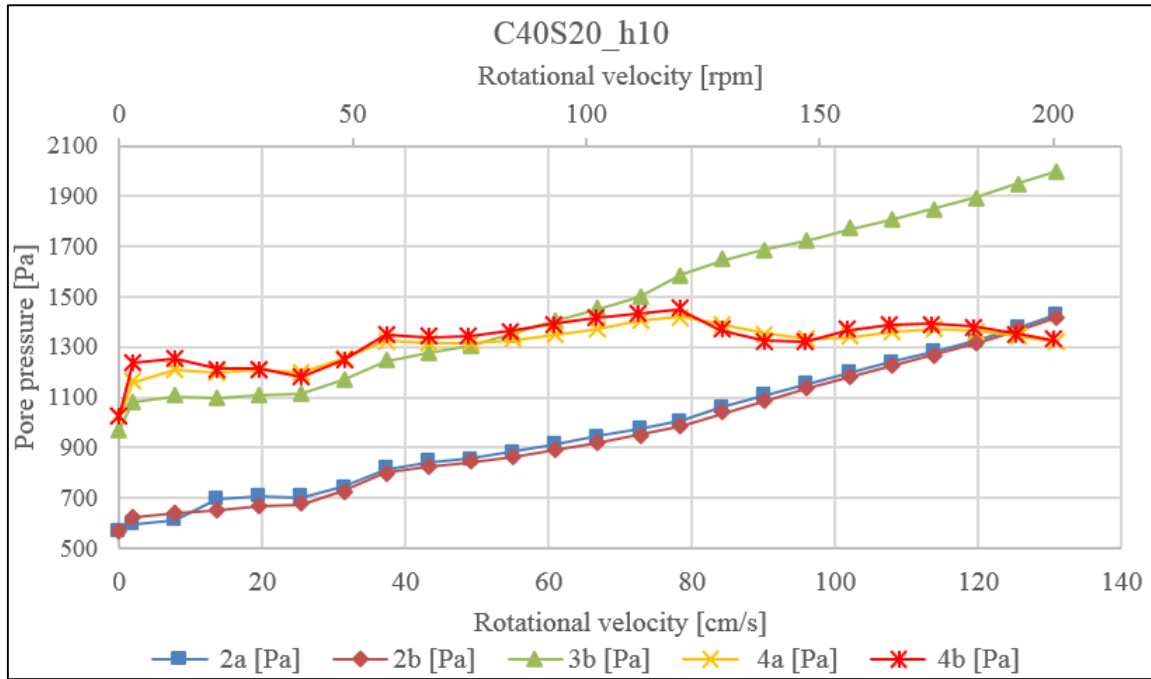
Figure 4.2: Original pore pressure in relation to rotational velocity in test $C40S20_{h10}$
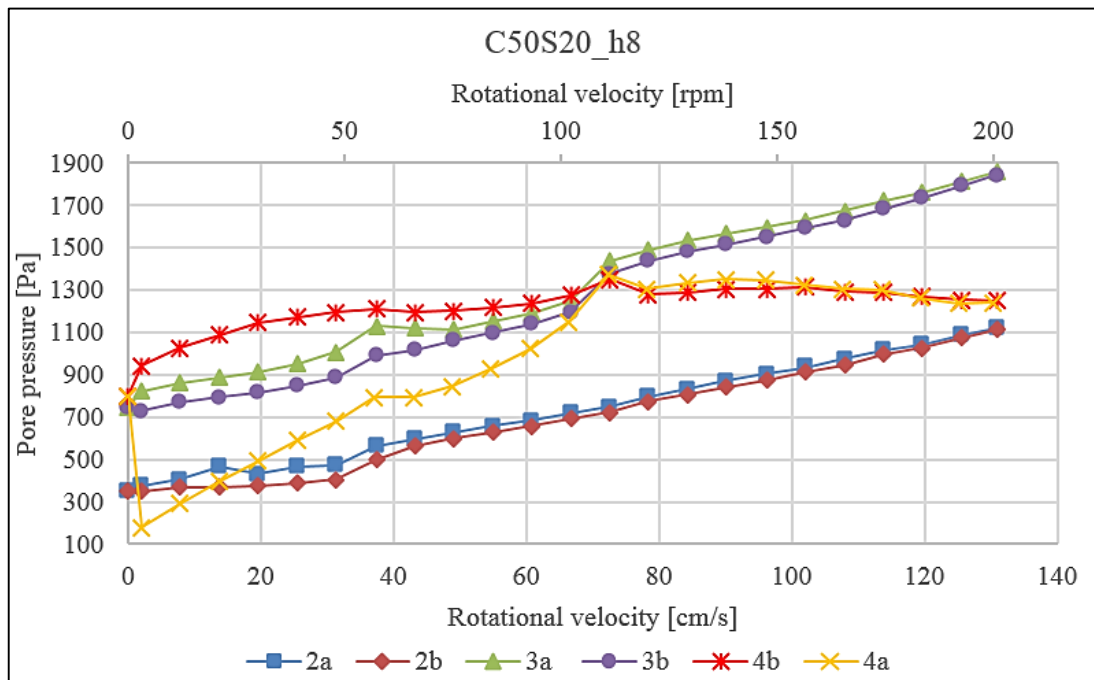
Figure 4.3: Original pore pressure in relation to rotational velocity in test $C50S20_{h8}$
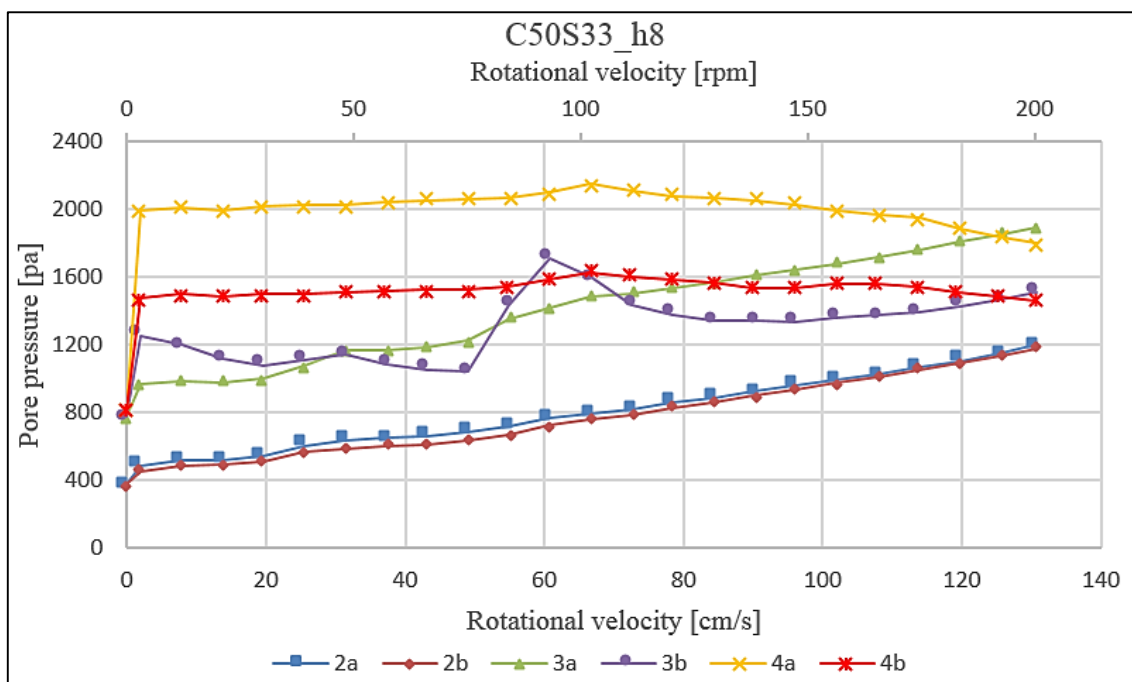
Figure 4.4: Original pore pressure in relation to rotational velocity in test $C50S33_{h8}$
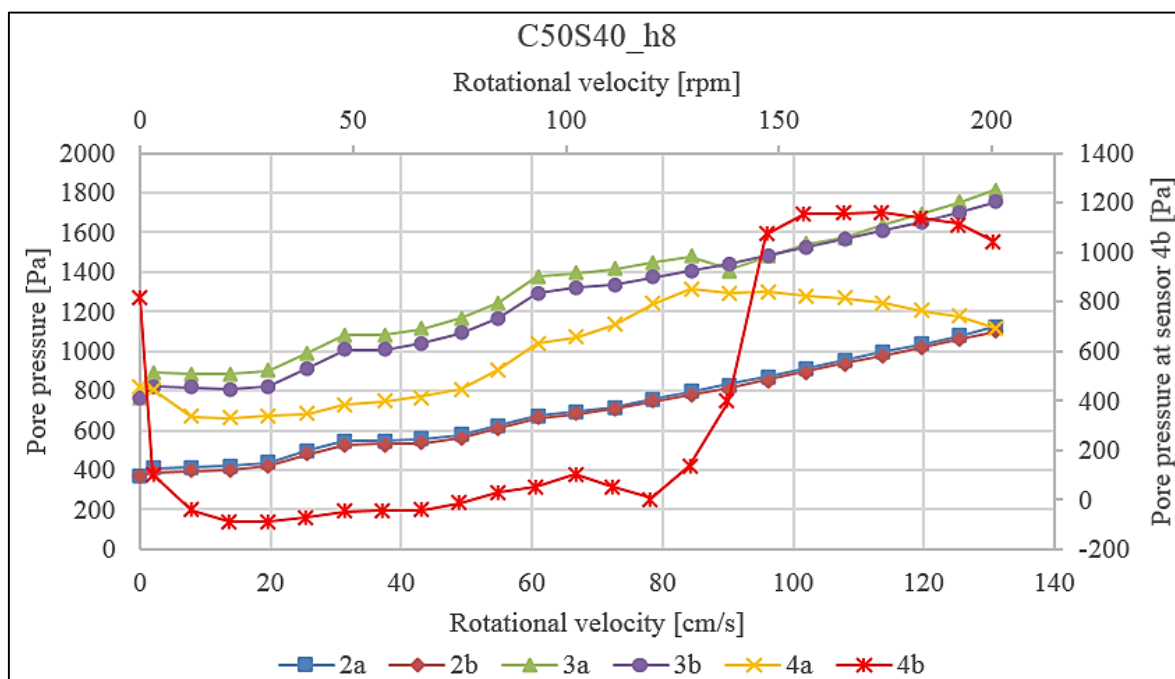
Figure 4.5: Original pore pressure in relation to rotational velocity in test $C50S40_{h8}$
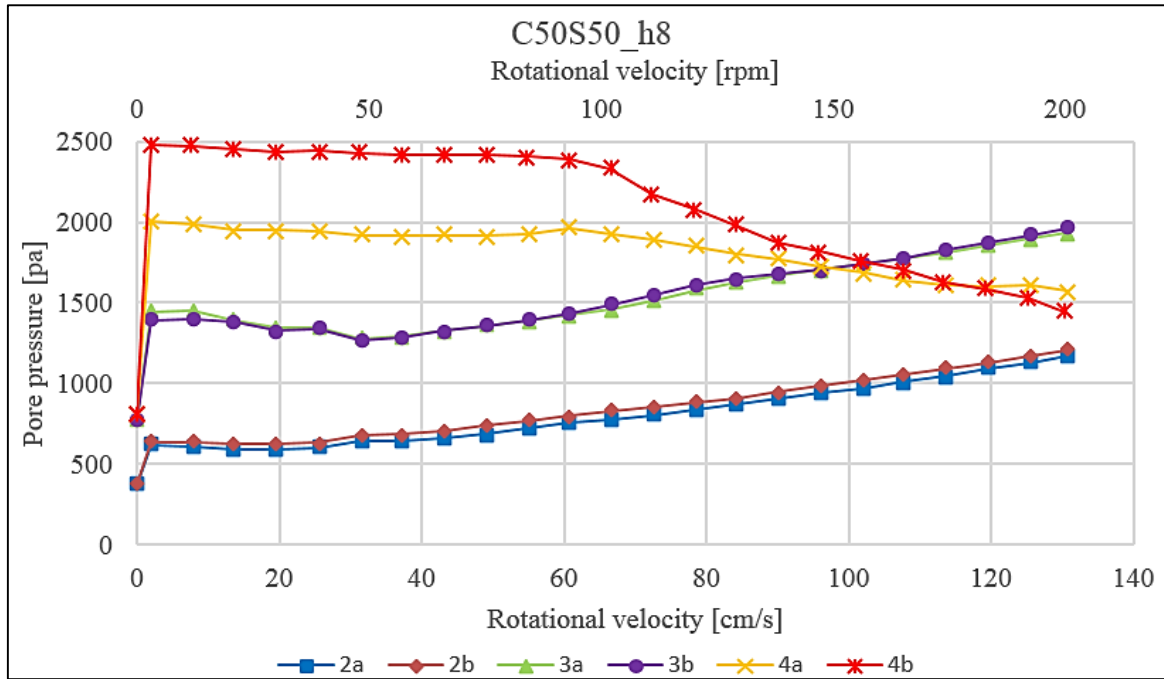
Figure 4.6: Original pore pressure in relation to rotational velocity in test $C50S50_{h8}$
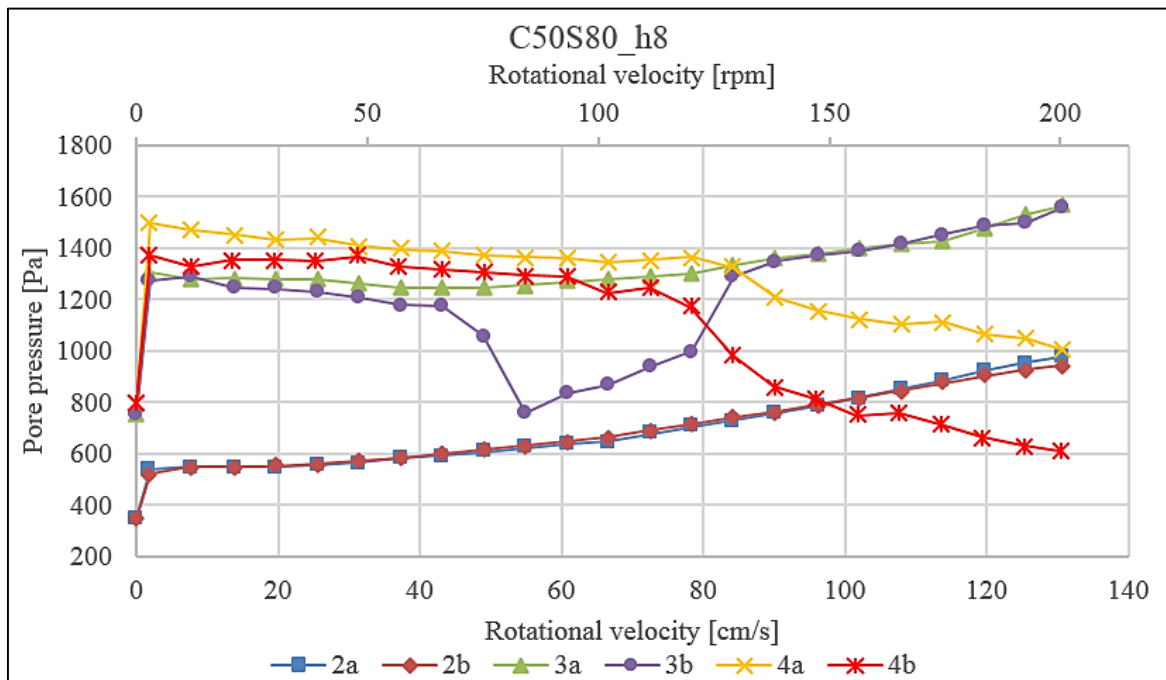
Figure 4.7: Original pore pressure in relation to rotational velocity in test $C50S80_{h8}$
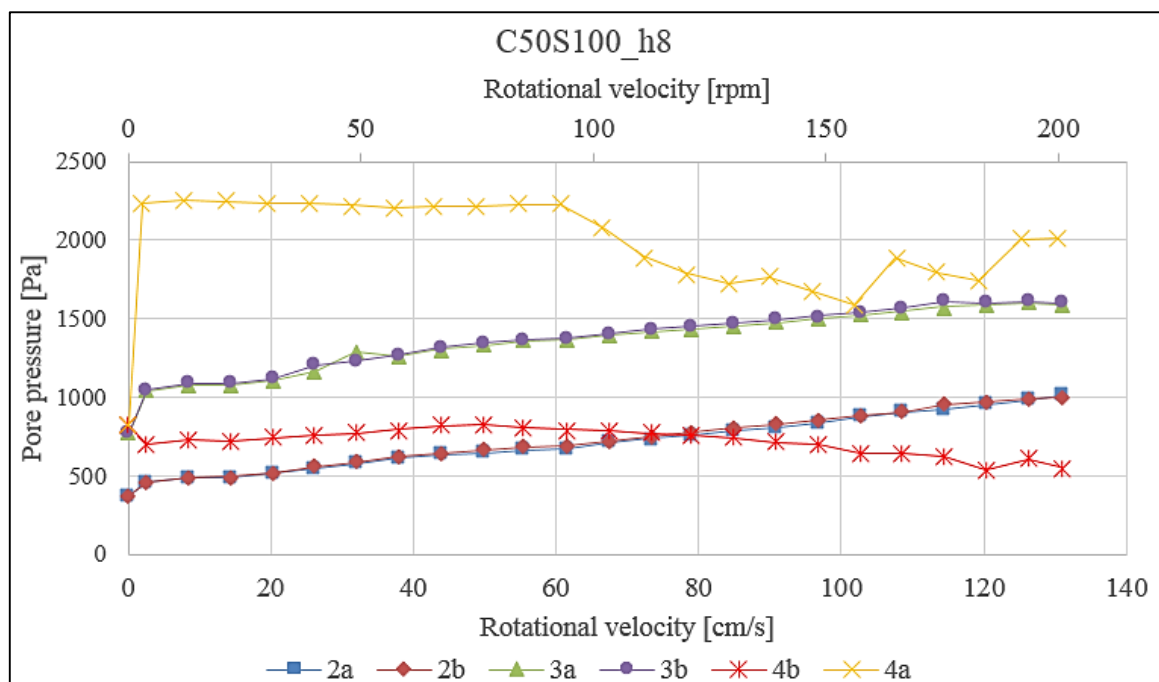
Figure 4.8: Original pore pressure in relation to rotational velocity in test $C50S100_{h8}$

4.3. Analysis of original results

After zero values were set when no mixture had been filled in cylinder, pore pressures were measured in kPa per second. The final stable readings found at completion of dissipation were believed to correspond to hydrostatic pressure, and were used to adjust measured data, which means to increase or decrease according to the difference between stable values and hydrostatic pressures (see illustration Fig. 4.9). Here original results of excess pore pressure are processed in Pa.
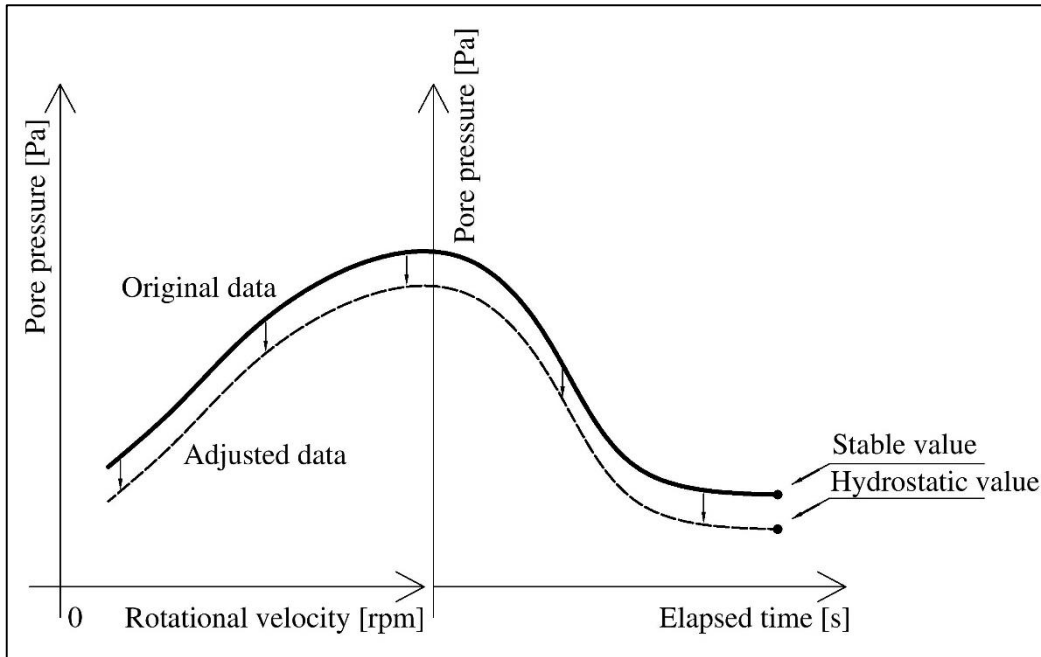
Figure 4.9: Original data adjustment

4.3.1. Quality evaluation of sensors

As the heights of most tested samples were below 10 cm, six sensors were installed on the wall with three on each side. They were named as 1a&1b, 2a&2b, and 3a&3b from top to base. The two sensors on base were labeled as 4a&4b as shown in Fig. 4.10.
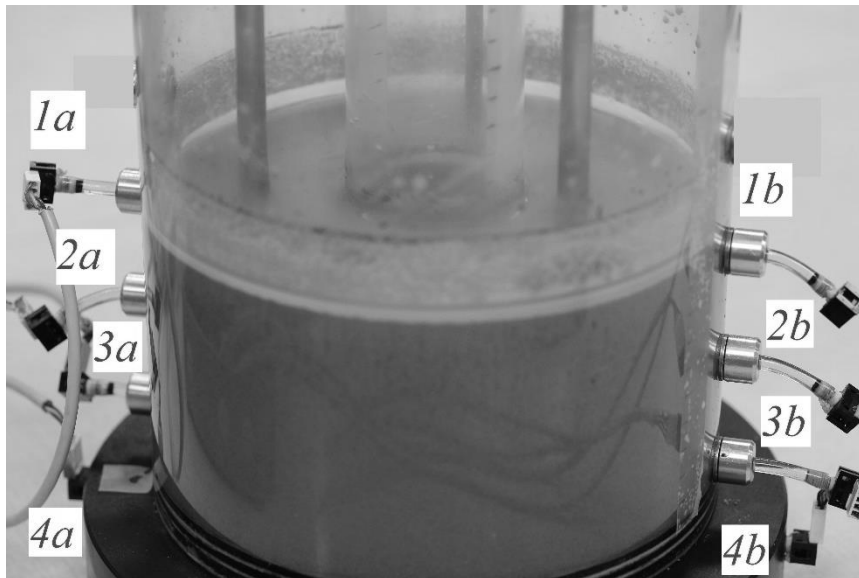
Figure 4.10: Naming of sensors

At static state and low rotational velocity the mixture near surface consisted with more liquid. During fast rotation the height of mixture varied drastically (Fig. 4.11), which would aggravate the instability of readings of sensors 1a and 1b.
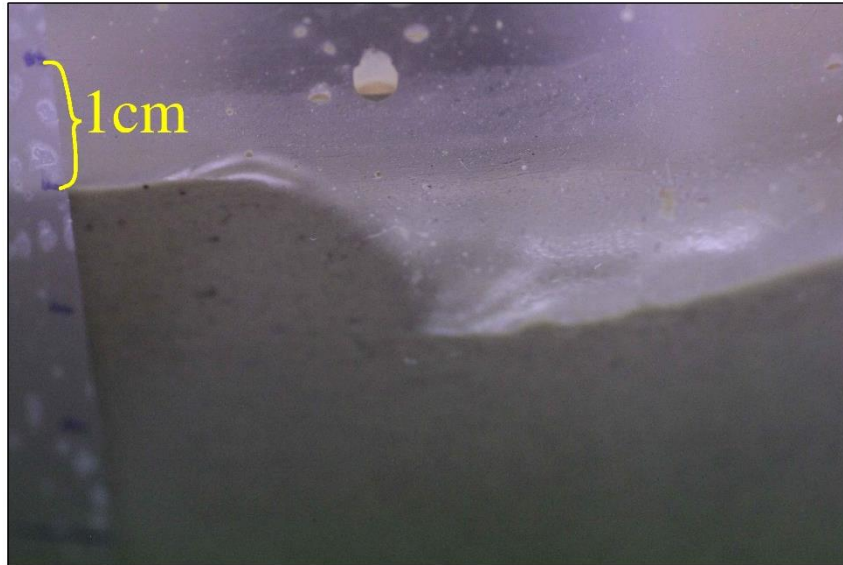
Figure 4.11: Turbulent surface at high rotational velocity

Compared with sensors 1a and 1b, sensors 2a and 2b gave much more stable and consistent readings. However, as a result of inverse segregation (Savage and Lun 1988), richer fine grain content was found near basal layer which was best represented by material at sensors 3a&3b's height.

In Wang & Sassa's (2003) experiment, data was only obtained from sensors installed at base. While in this study the two porous stones were often found to give divergent readings (see "Section 4.2"), which fact had data quality of readings from sensors 4a and 4b suffer. Even though one of these two sensors can be trusted, severe vortex posed another challenge as it became difficult to measure mixture's height above them, subsequently impeding the acquisition of net excess pore pressure and floating ratio.

Owing to the above reasons, sensors 3a and 3b stood as the most promising ones regarding the objective of observing the relationship between rotational velocity and pore pressure built-up as well as floating ratio.

4.3.2. Rods-insertion induced excess pore pressure and modified procedure

In test $C50S50_{h8}$ it was found that a considerable jump of pore pressure occurred upon initiation of test following the procedure that allocated 5 minutes for each velocity step before data-saving started. Instead of increasing with rotational velocity pore pressures measured at sensors 3a and 3b decreased until velocity 48 rpm (see Fig. 4.12). Since silt content had been raised and mixing rods were inserted given a short time, thus a most plausible postulation could be that excess pore pressure formed as a result of rods-insertion, and later was maintained as the mixture near outer wall had not been stirred up before certain velocity. Bearing this in mind a modification of experiment process was made that the initial velocity 3 rpm must be

maintained until no decrease of pore pressure can be observed before proceeding to next velocity.
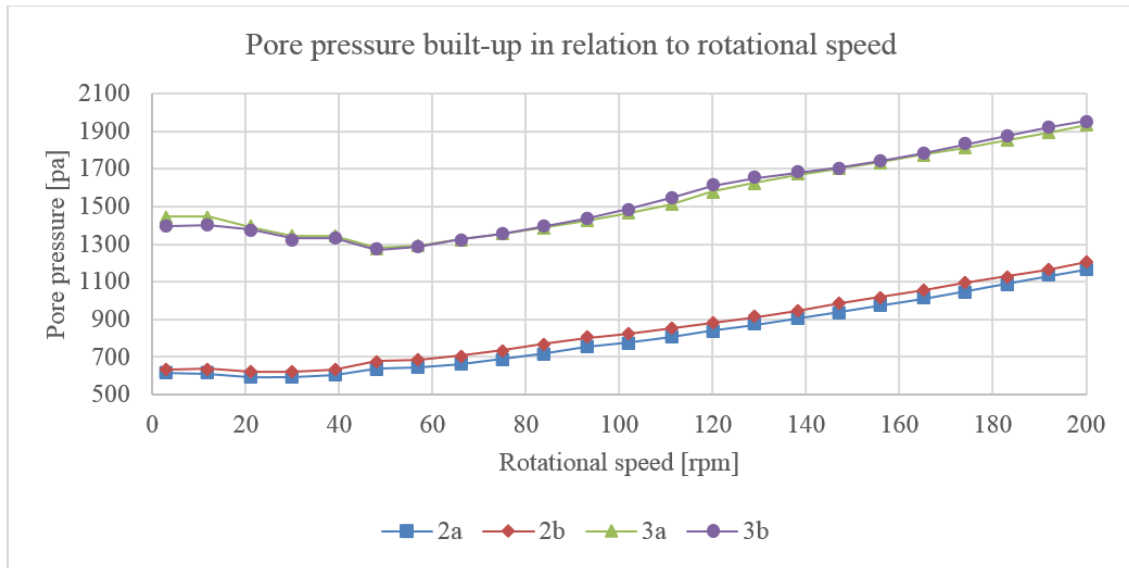
Figure 4.12: Pore pressure built-up in $C50S50_{h8}$

Later in an attempt of observing pore pressure built-up during deceleration in test $C50S50_{h8}$, pore pressure without the influence of rods-insertion before velocity 48 rpm was recorded. With this procedure not only pore pressure built-up can be studied, but less time would be consumed. The velocity would be raised directly to 200 rpm again before dissipation could be observed. Later the exploration of correlation between initial excess pore pressure and silt content was also made possible. As a result, this procedure had been adopted ever since. Fig. 4.13 below illustrates such test procedure in terms of pore pressure measurement at sensor 2b.
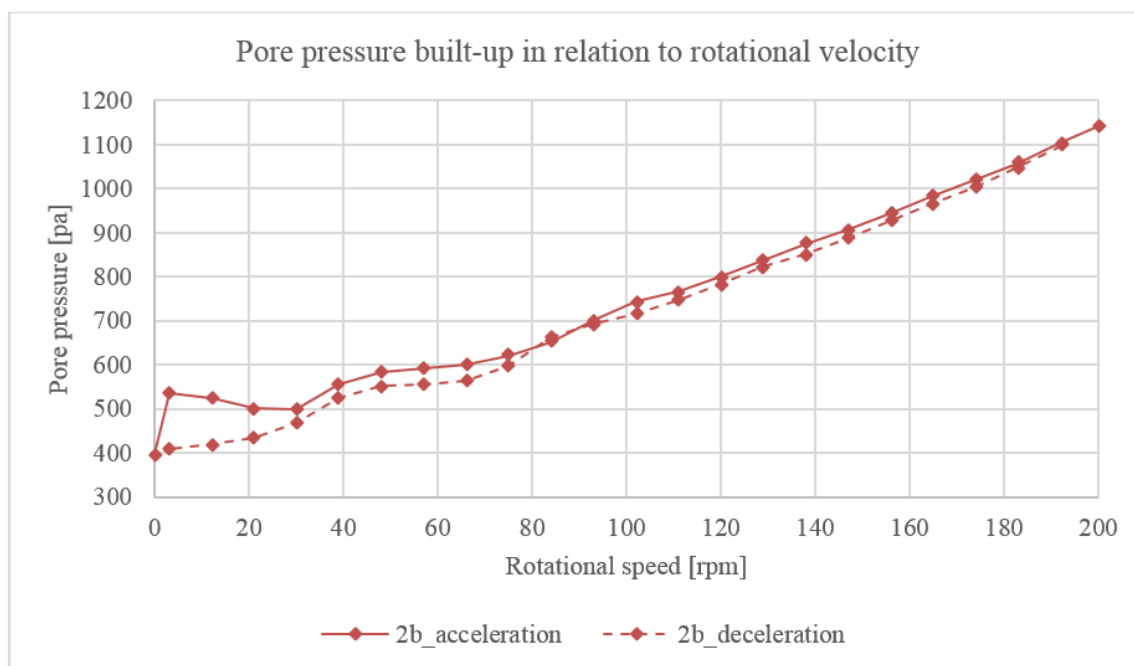
Figure 4.13: Modified test procedure

4.3.3. Test series one

While silt content by weight was kept as 20%, solid fraction concentration by volume increased from 20% to 40% and 50% corresponding to porosities 0.8, 0.6 and 0.5. Since different mixture heights were used, thus excess pore pressure is normalized by individual hydrostatic pressure, i.e. $\frac{\Delta u}{\gamma_w h}$, where h is water height at sensor. After initial growth upon initiation a range of velocity (3 rpm to 39 rpm) without meaningful growth was seen in all three tests. This may be because the generated excess pore pressure was confined to narrow zone around rods, and rapidly dissipated radically and vertically. Following this stage a short duration of sharp linear rise was experienced by test $C50S20_{h8}$ interestingly before another segment of moderate development was seen. As excess pore pressure had been continuously accumulated, another mechanism of decreasing excess pore pressure in addition to dissipation must exist. Tests $C30S20_{h10.3}$ and $C40S20_{h10}$ displayed simpler behavior; their growing rates seemed identical to test $C50S20_{h8}$ after velocity 120 rpm (78.48 cm/s), giving a constant disparity (0.248) for adjacent tests.
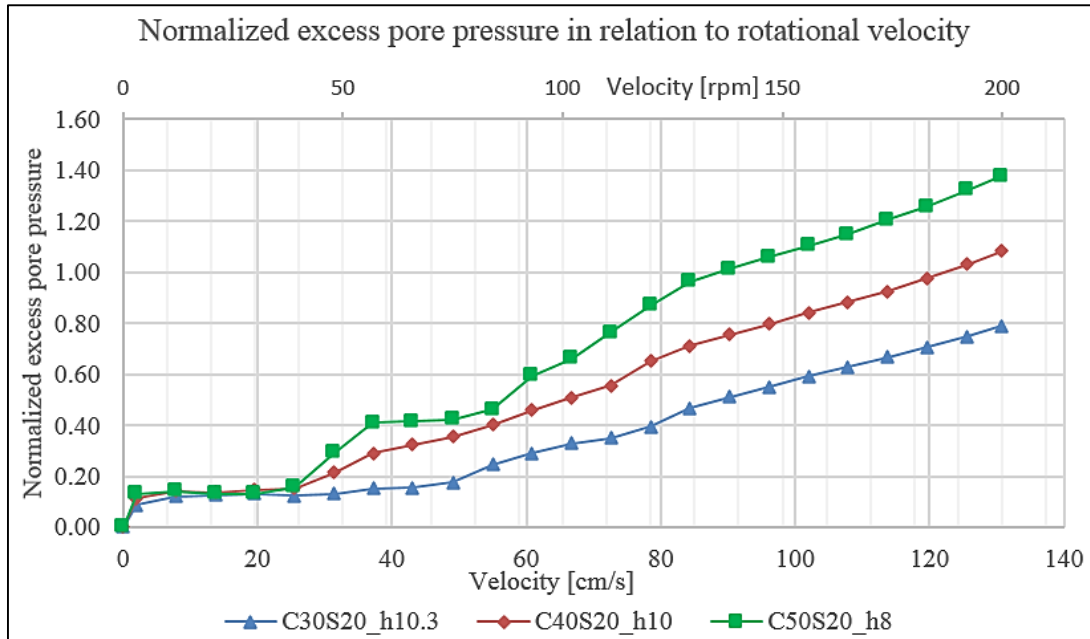
Figure 4.14: Normalized excess pore pressure built-up in test series one

4.3.4. Test series two

In this series of test solid fraction concentration was maintained as 50% while silt content was varied among 20%, 33%, 40%, 50%, 80% and 100%. Abnormal values exist at the beginning of test $C50S50_{h8}$ due to the influence of rods insertion. The data after velocity 48 rpm (31.392 cm/s) can still be trusted though. As far as individual test is concerned, similar characteristics can be detected as in "samples of varying solid concentration". Generally higher excess pore pressure is gained with higher content of silt. However tests $C50S33_{h8}$ and $C50S40_{h8}{}^{*}$ give almost identical values. The difference between tests $C50S20_{h8}$ and $C50S33_{h8}$ dwindles until velocity 138 rpm (90.252 cm/s) where parallel plots start.
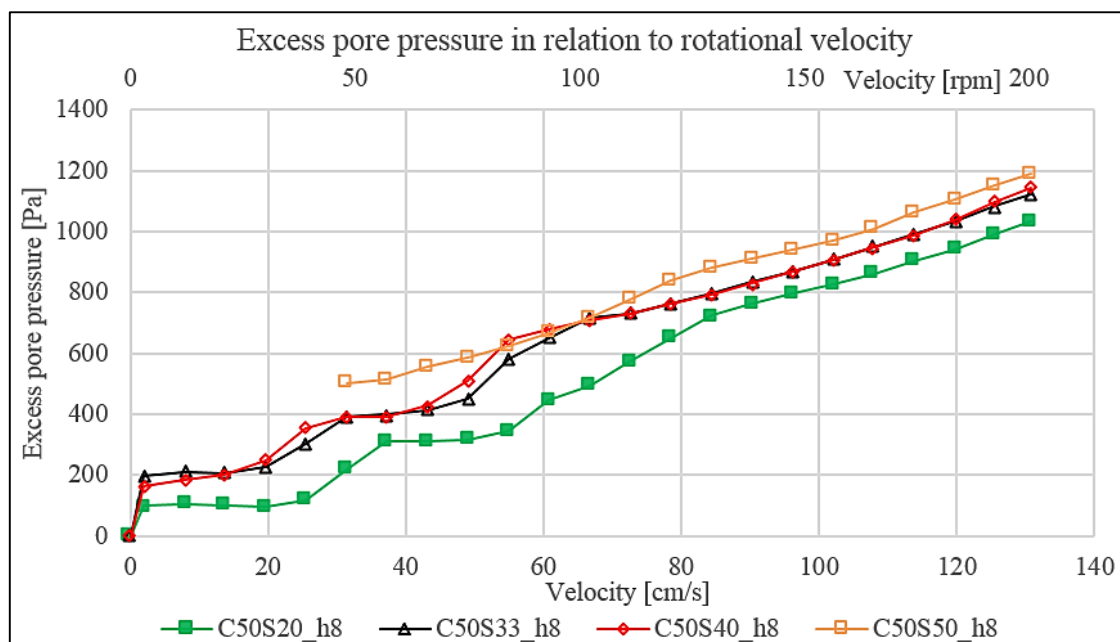
Figure 4.15: Excess pore pressure built-up in test series two except for $C50S80_{h8}$ and $C50S100_{h8}$

The situation gets complicated after tests $C50S80_{h8}$ and $C50S100_{h8}$ were included for consideration. These two tests start with greater Initial excess pore pressure, and that of test $C50S80_{h8}$ even exceeds test $C50S100_{h8}$. Thereafter test $C50S80_{h8}$ continues to rise linearly but at more moderate rate compared with the previous four tests. Eventually it reaches 814 Pa which is 218 Pa lower than that of test $C50S20_{h8}$. A stable gap of around 90 Pa between test $C50S100_{h8}$ and $C50S80_{h8}$ was formed soon after initiation and pertained except for the last two velocity steps. Bearing all six tests in mind, it appears implausible to explain with a straightforward pattern.
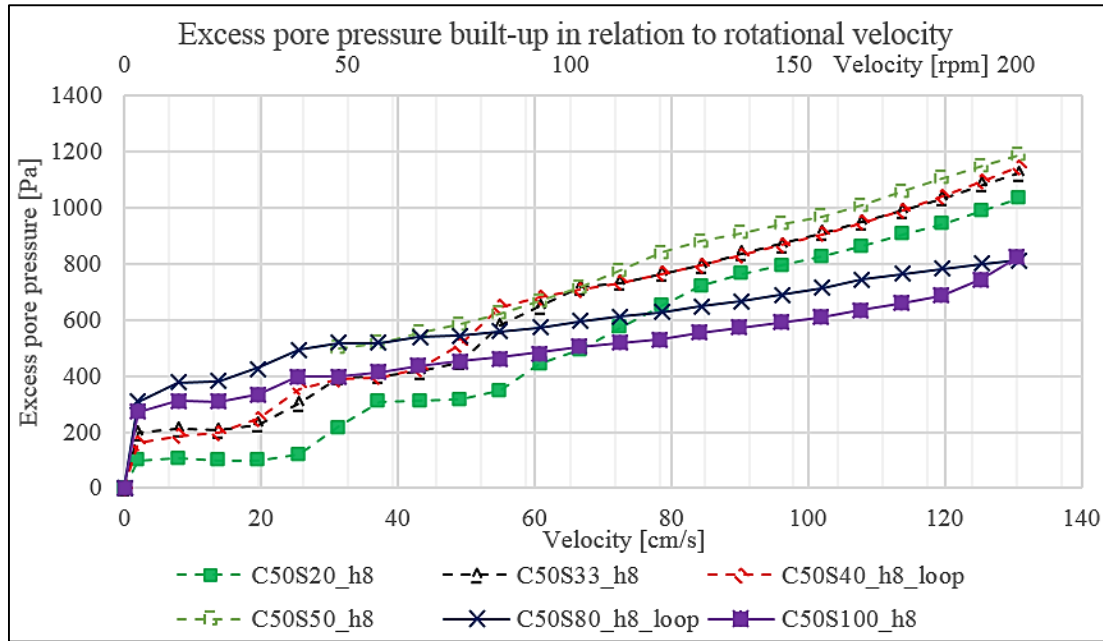
Figure 4.16: Excess pore pressure built-up in test series two

4.4. Centrifugal correction

Different from Wang & Sassa's (2003) experiment in which sensors installed at base provided pore pressure readings, in my work the two sensors at base failed to offer reliable data, and wider rotational velocity range was used. As a result excess pore pressure readings detected on outer wall consist of not only contribution of particle and liquid interaction but also centrifugal effect. Accompanying high velocity rotation, vortex (Fig. 4.17) became marked and varied with velocity and sample.

Figure 4.17: Illustration of vortex

In order to quantify centrifugal effect tests of pure water were performed with various heights: 8.2 cm, 10 cm and 12 cm. Average of net excess water pressure, i.e. difference between pressure measured and initial hydrostatic pressure, at sensors 3a and 3b are plotted in Fig. 4.18 in relation to rotational velocity. All three tests give consistent results. This validates that vortex is only the manifestation of centrifugal force, and should not be deducted separately, which

would undermine net excess water pressure. Average values of the three tests were used for correction.
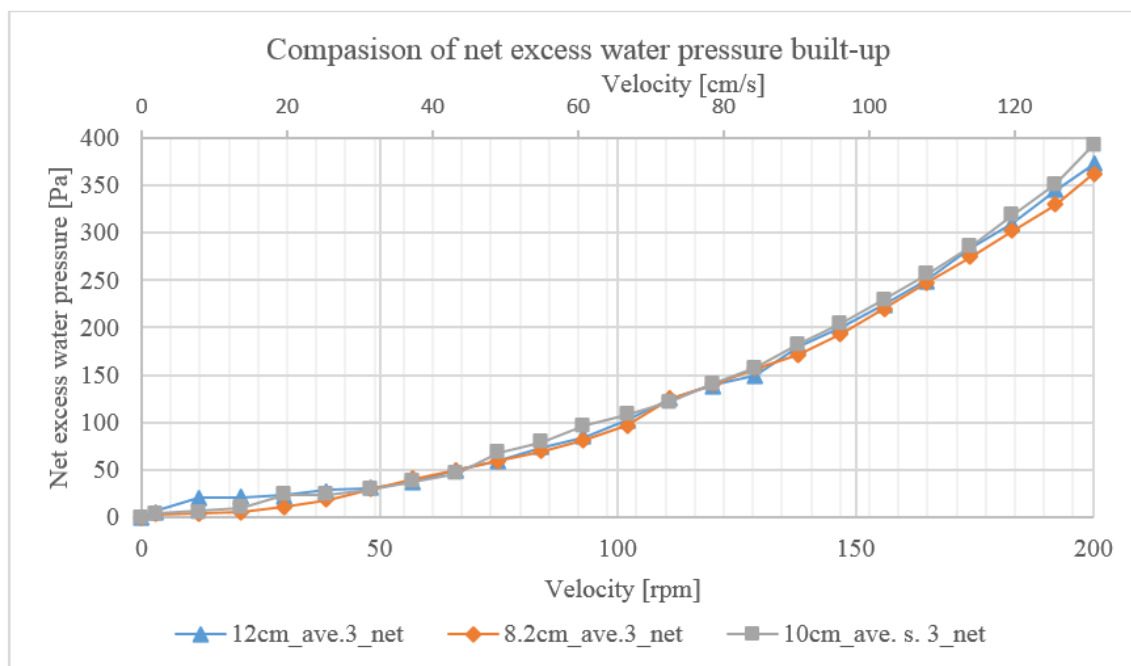
Figure 4.18: Comparison of net excess water pressure built-up in three pure water tests

4.5. Corrected results

Centrifuge effect corrected net excess pore pressure from sensors 2a, 2b, 3a and 3b in some representative tests are plotted below. Readings from sensors 4a and 4b were not included as a result of the absence of mixture height, which would make the derivation of net excess pore pressure untenable.
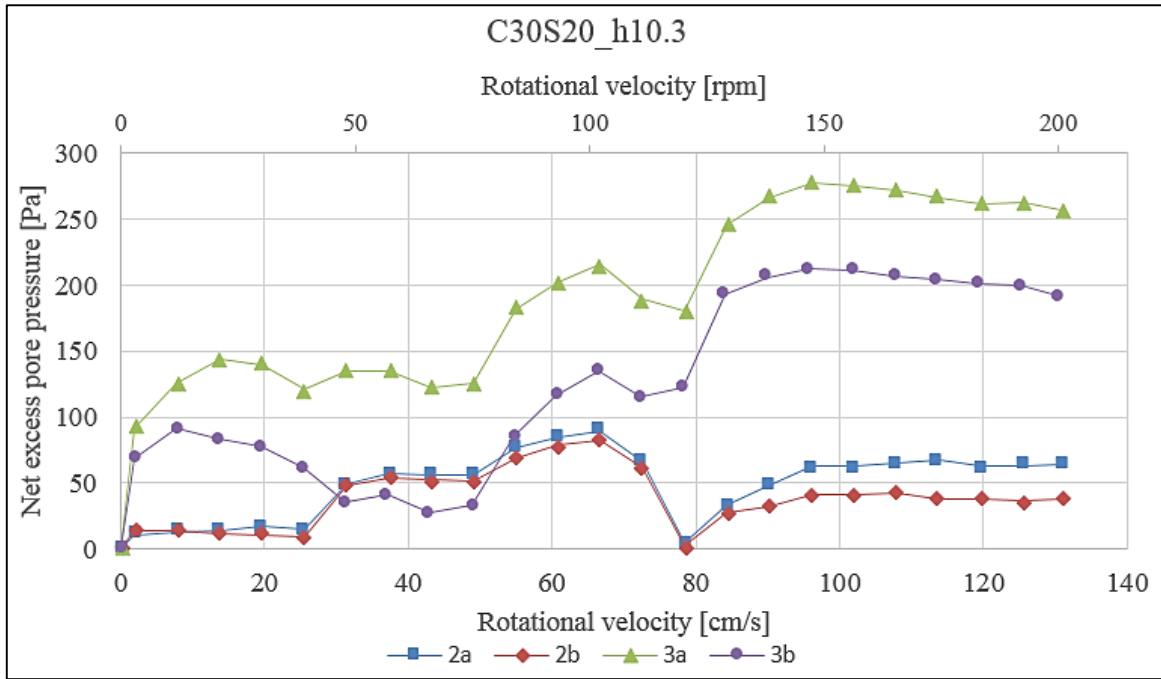
Figure 4.19: Net excess pore pressure built-up in test $C30S20_{h10.3}$
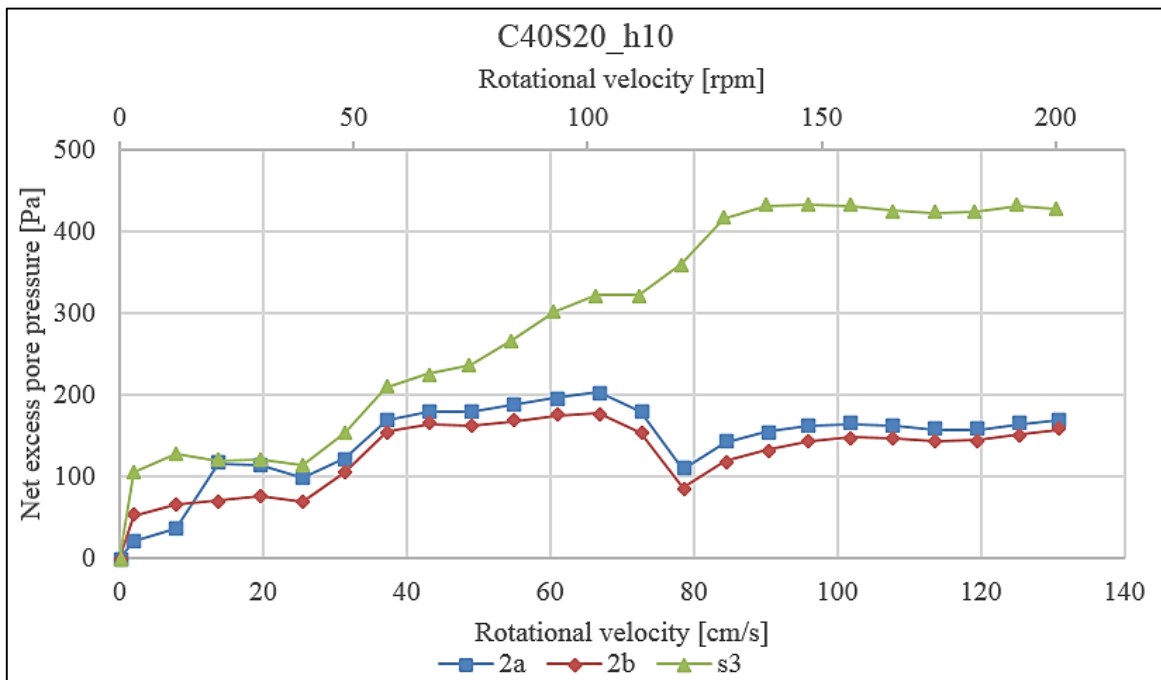
Figure 4.20: Net excess pore pressure built-up in test $C40S20_{h10}$
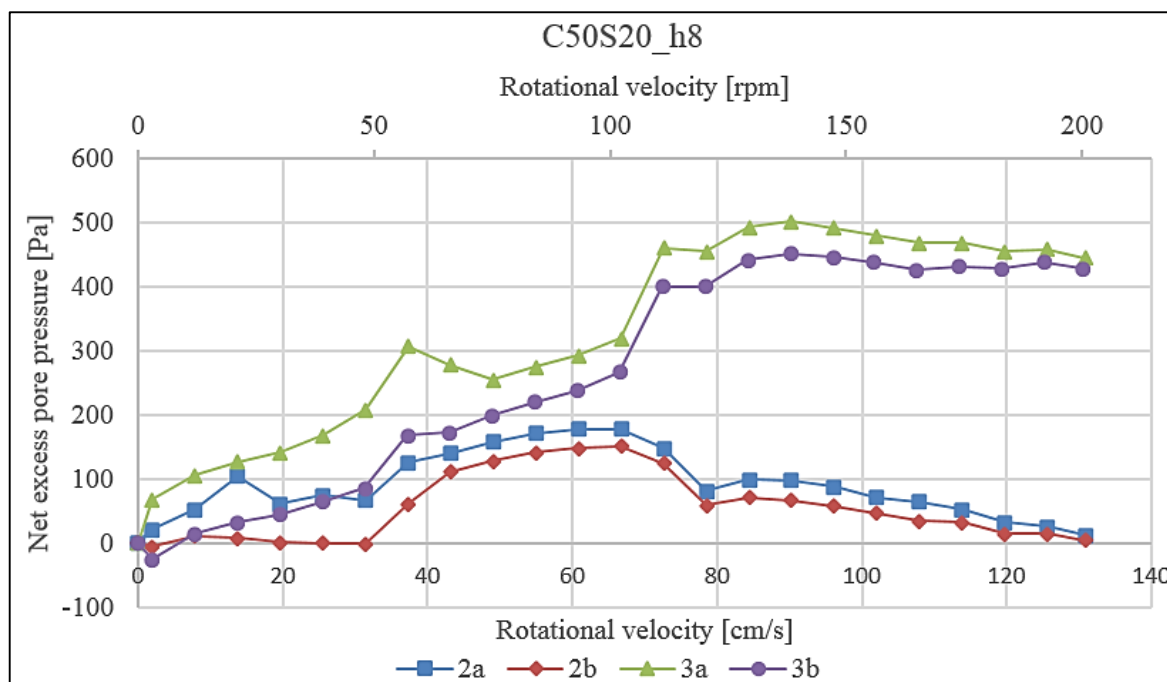
Figure 4.21: Net excess pore pressure built-up in test $C50S20_{h8}$
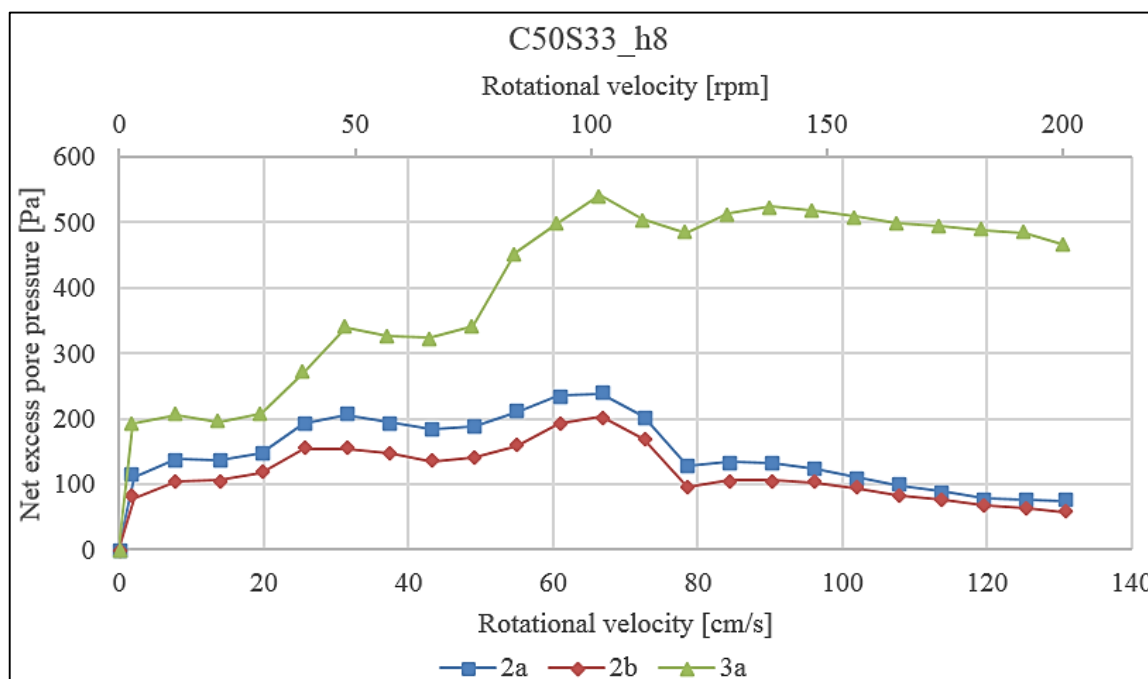
Figure 4.22: Net excess pore pressure built-up in test $C50S33_{h8}$
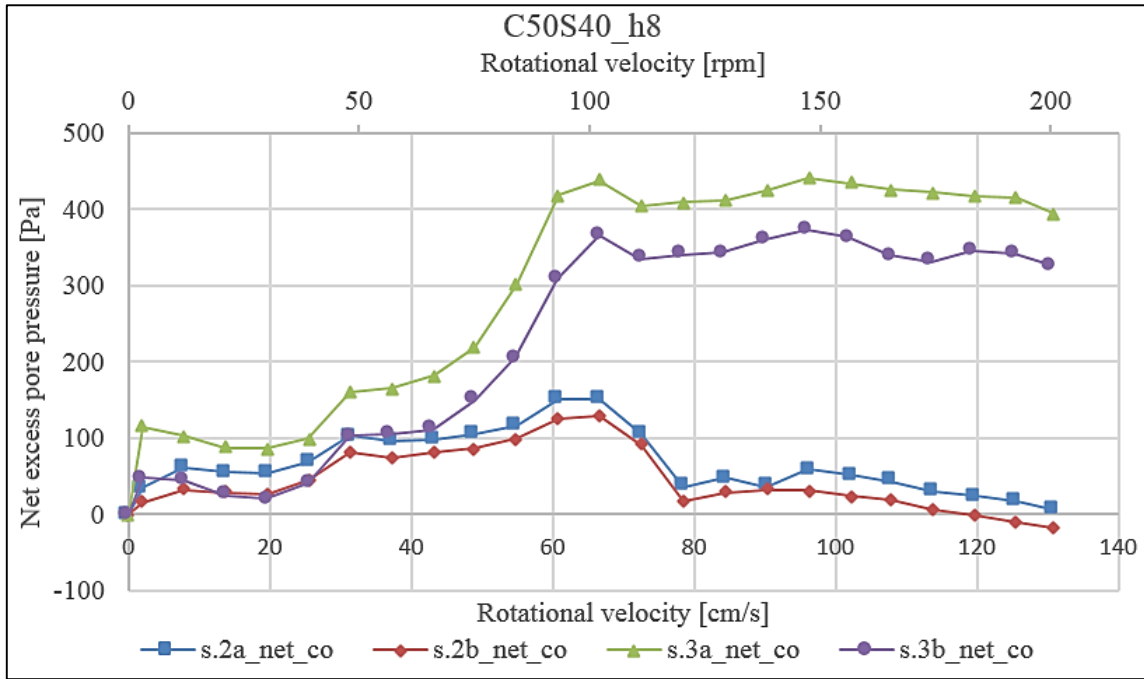
Figure 4.23: Net excess pore pressure built-up in test $C50S40_{h8}$
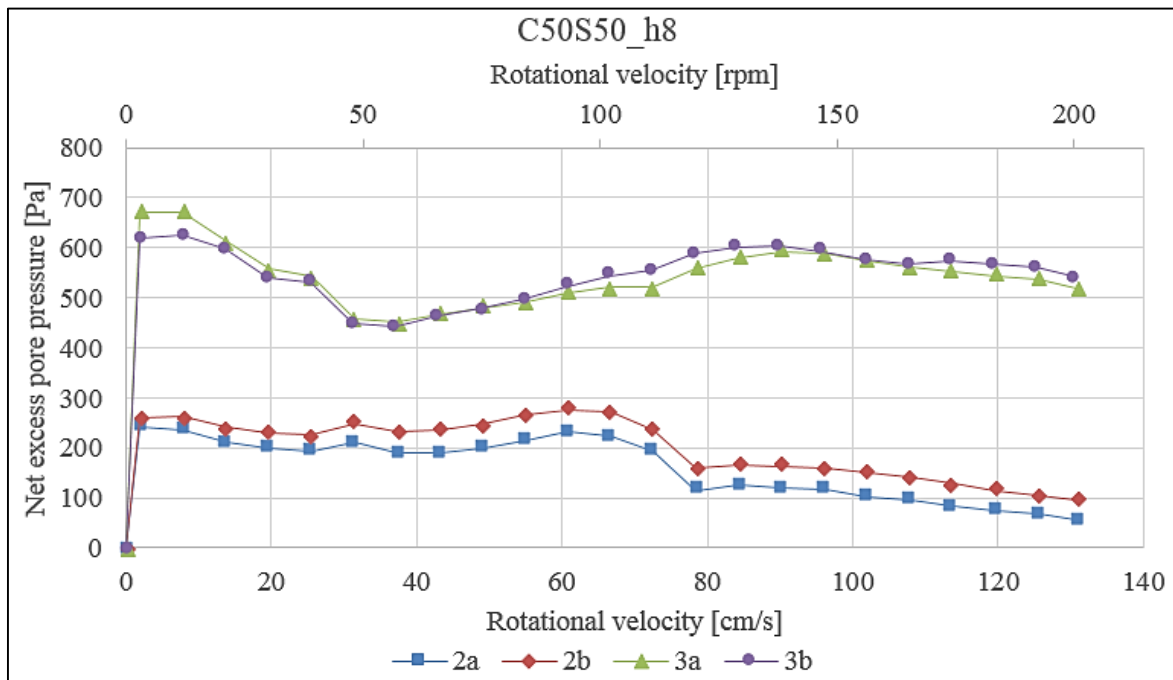
Figure 4.24: : Net excess pore pressure built-up in test $C50S50_{h8}$
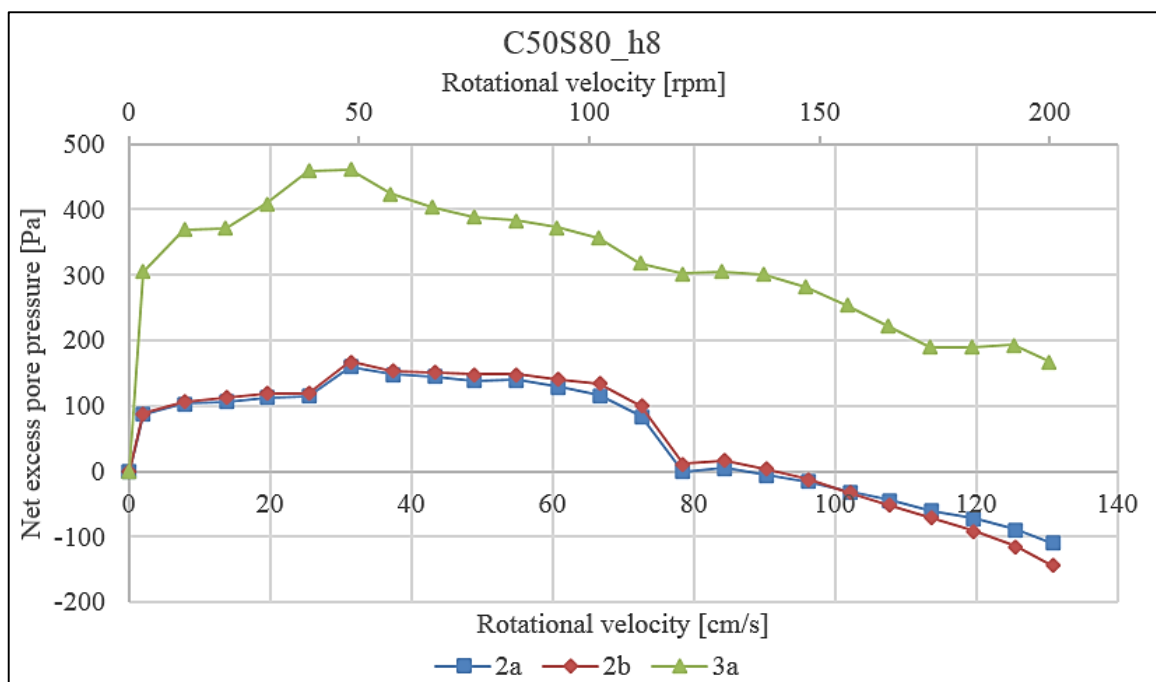
Figure 4.25: Net excess pore pressure built-up in test $C50S80_{h8}$
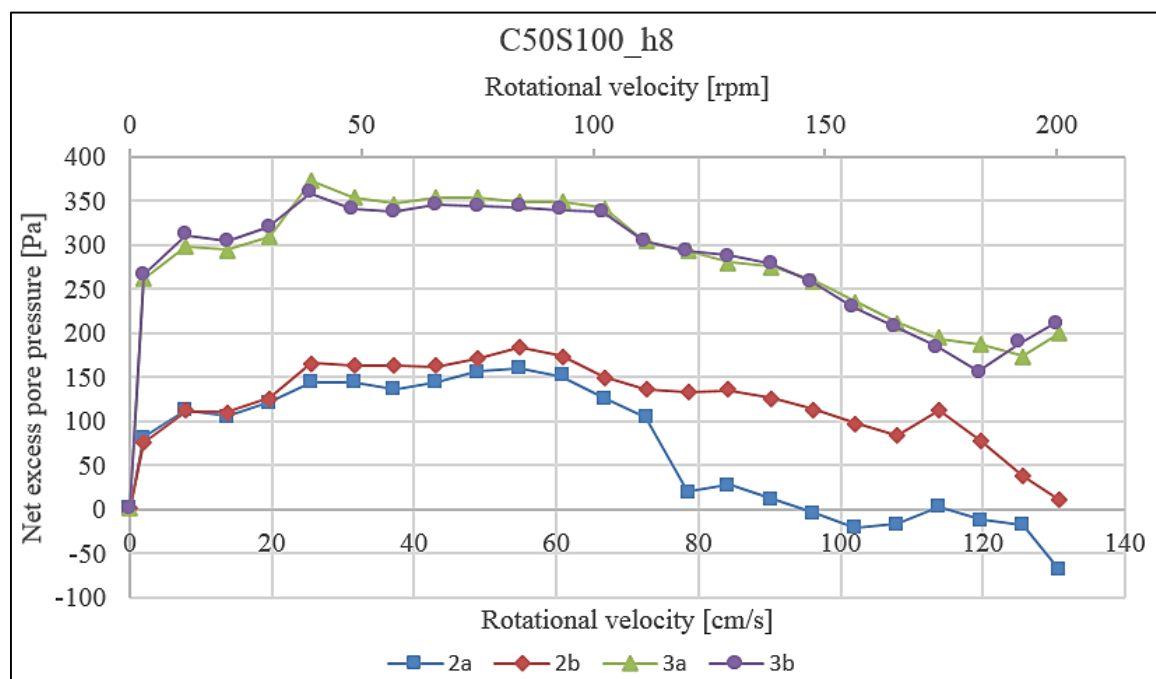
Figure 4.26: Net excess pore pressure built-up in test $C50S100_{h8}$

4.6. Analysis of corrected results

4.6.1. Net excess pore pressure

Test series one

After centrifugal correction and mixture height normalization, the net excess pore pressure exhibits more distinct characteristics (Fig. 4.27). First of all higher net excess pore pressure is obtained with higher solid concentration in a nonlinear manner. Secondly, in contrast to the previous uncorrected results, constant values other than linear growth were achieved by three tests at approximately the same velocity 129 rpm (84.366 cm/s). Besides, tests $C30S20_{h10.3}$ and $C50S20_{h8}$ possess the middle stagnation while test $C40S20_{h10}$ shows rather linear development within this range.
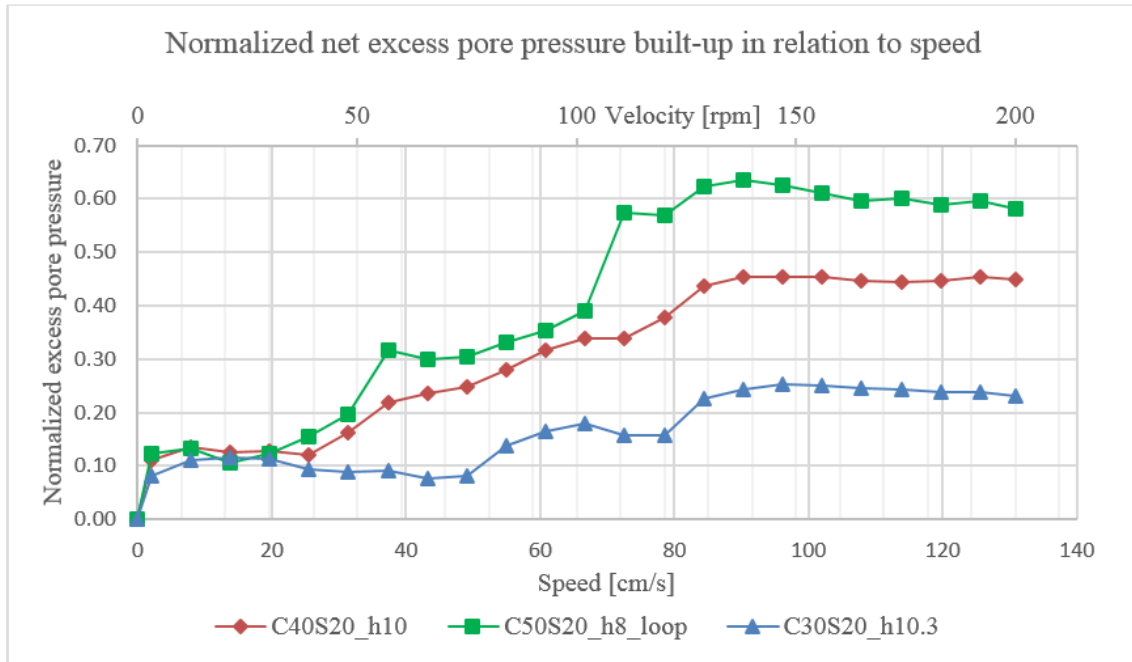
Figure 4.27: Normalized net excess pore pressure built-up in test series one

Test series two

Compared with the uncorrected results of this series, linear rise after velocity 129 rpm (84.366 cm/s) is replaced by modest decrease in all tests (see Fig. 4.28), and the decreasing rates seem alike. But the pattern that greater net excess pore pressure (Δu_{net}) is gained with higher silt content is maintained though the difference between tests $C50S33_{h8}$ and $C50S40_{h8}^{*}$ is minimal. Regarding the velocity when Δu_{net} started to level off, lower velocity appears to correspond to test with higher silt content except for test $C50S50_{h8}$ which is flawed in quality.
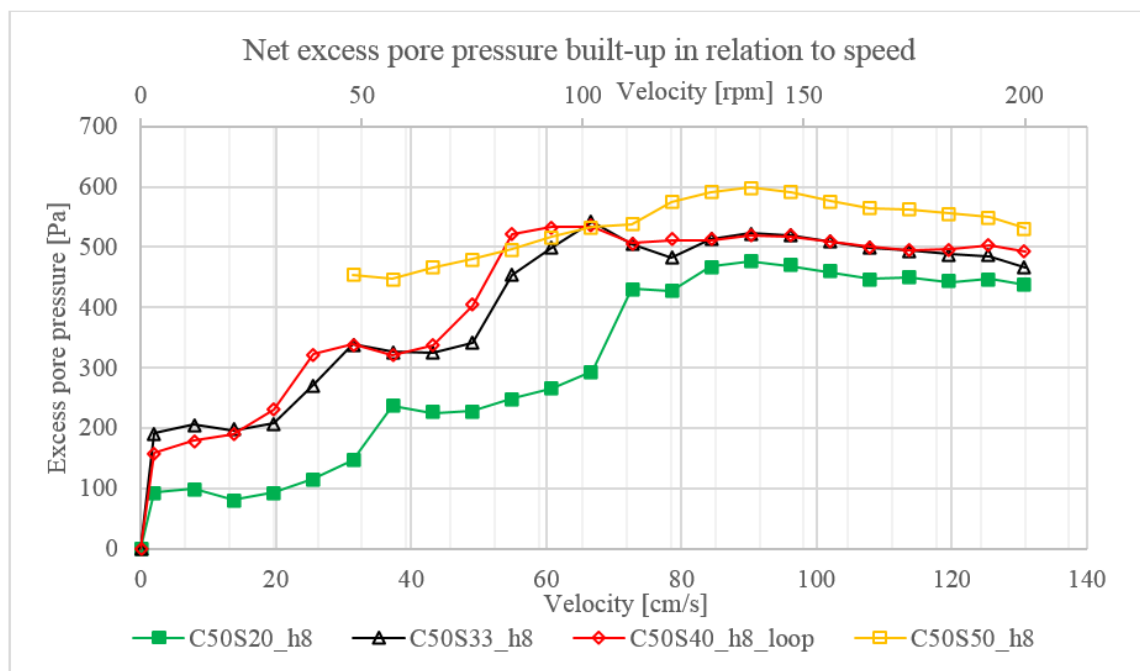
Figure 4.28: Net excess pore pressure built-up in test series two excluding $C50S80_{h8}$ and $C50S100_{h8}$

Similar to the phenomenon observed in previous uncorrected results, initial Δu_{net} exceeding half of their peak value was met in tests $C50S80_{h8}$ and $C50S100_{h8}$ (Fig. 4.29). And the maximum Δu_{net} in test $C50S100_{h8}$ is inferior to that in $C50S80_{h8}$ which is even lower than that in $C50S20_{h8}$. Once again prolonged declines present in both tests. But a range of constant values in test $C50S100_{h8}$ from velocity 48 rpm (31.392 cm/s) to velocity 102 rpm (66.708 cm/s) is not seen in test $C50S80_{h8}$.
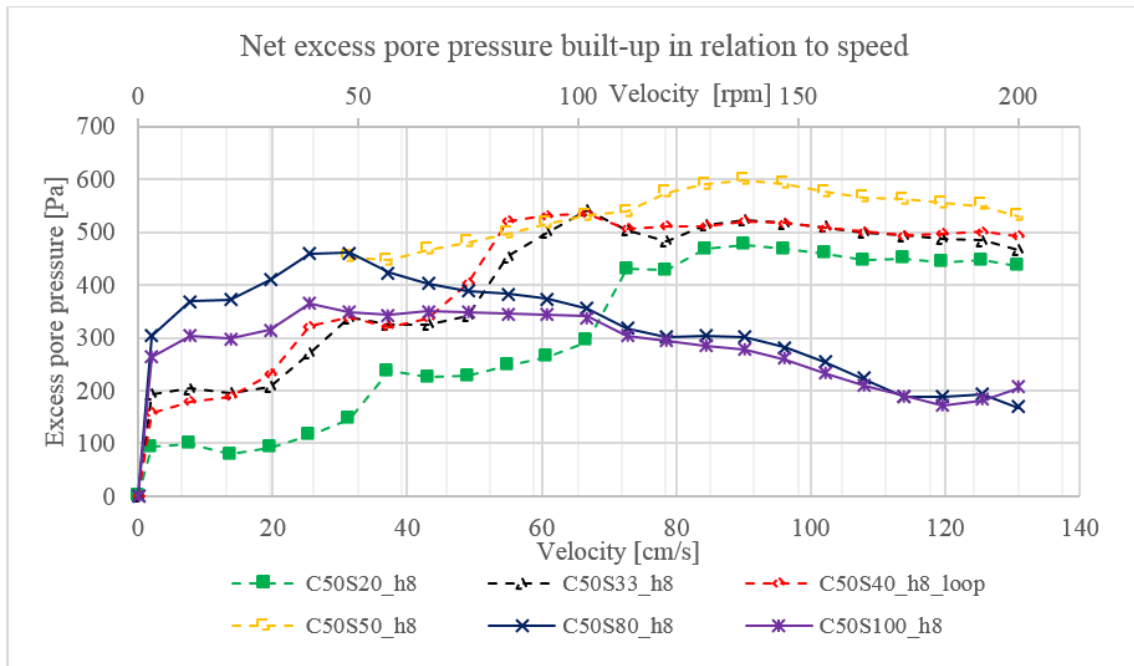
Figure 4.29: Net excess pore pressure built-up in test series two

The abrupt jump under speed 3 rpm (1.962 cm/s) in these two tests seemed suspicious. In order to verify this suspicion, one more test $C50S80_{h8}$ was performed with 1 rpm as velocity increment, and 60 rpm as ending point. As shown in Fig. 4.30, where data from the average of sensor 3a and 3b is plotted, similar sharp pore pressure built-up was obtained again, which consequently verifies the existence of initial abrupt increase.
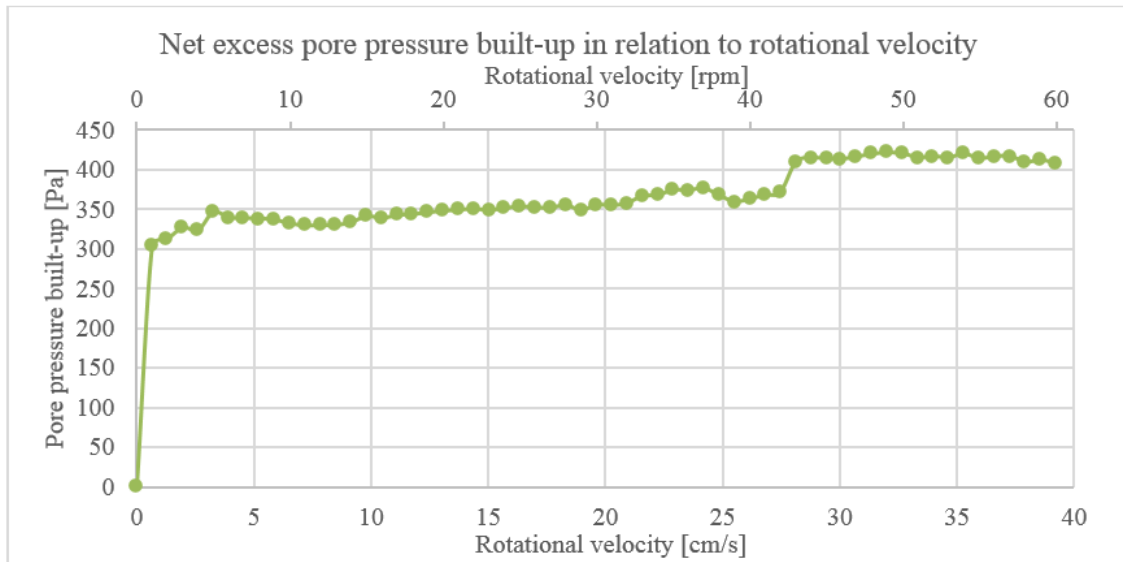
Figure 4.30: Verification of initial net excess pore pressure jump

4.6.2. Net excess pore pressure distribution

A rough idea of net excess pore pressure distribution is made possible by plotting the average results from sensor 2a&2b and 3a&3b at some chosen velocity levels. Representative tests $C50S33_{h8}$ and $C50S80_{h8}$ are shown in Fig. 4.31 and Fig. 4.32. Starting from approximately linear profile, continuous increase of pore pressure occurred at both mid height and base. When rotational velocity rose to magnitude corresponding peak pore pressure generation, abrupt reduction of excess pore pressure was first perceived at sensors 2a and 2b in most samples excluding $C50S80_{h8}$ and $C50S100_{h8}$. While in these two samples, reductions were first detected with sensors 3a and 3b. After the first reduction comparable decreases were found at those two locations, thus giving nearly parallel curves in the lower segment of mixture. In some cases, for instance test $C50S80_{h8}{}^{*}$, the net excess pore pressure at sensor 2a&2b diminished to negative values. A mechanism accounting for the difference of net excess pore pressure development at different height is naturally demanded.
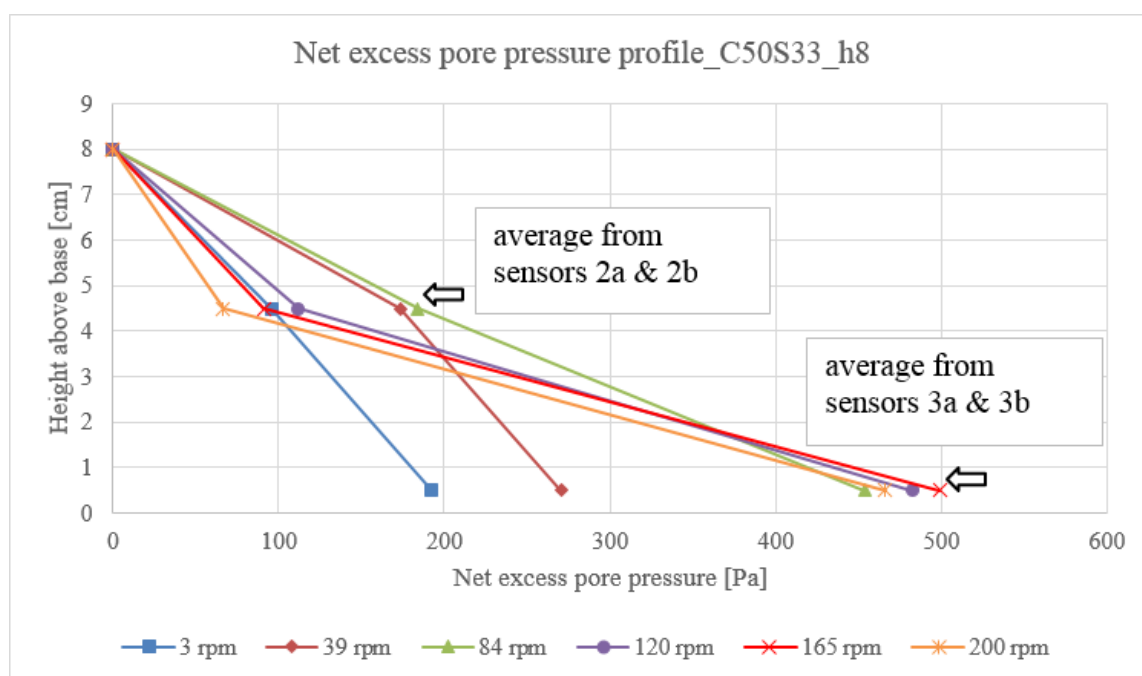
Figure 4.31: Net excess pore pressure profile in test $C50S33_{h8}$
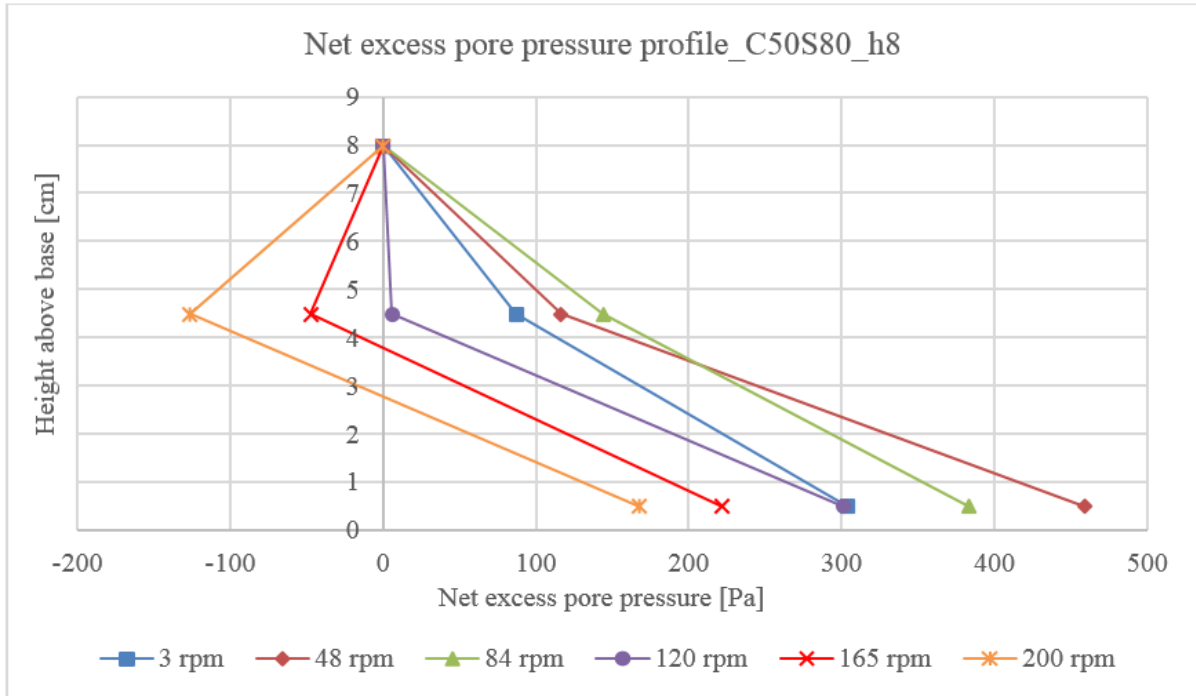
Figure 4.32: Net excess pore pressure profile in test $C50S80_{h8}$

According to Norifumi Hotta (2011) linear distribution of Reynolds stress (p_f) from turbulent mixing exist in stony debris flow (equation 4.1). However results in current study imply that this formula could not apply and more appropriate rheological equations are desired.

$$p_f = k_f \rho d^2 \frac{(1-c)^{2/3}}{c^{2/3}} \frac{25u_m^2}{4h^2}\left(1 - \frac{z}{h}\right)$$ *(4.1)*

4.6.3. Floating ratio

Test series one

To better compare excess pore pressure generation, test results were presented by floating ratio (γ_f) (Wang and Sassa 2003) which was originally defined as

$$\gamma_f = \frac{u - u_s}{\sigma_t - u_s}$$ *(4.2)*

where u is measured pore pressure, u_s is static water pressure ($u_s = \gamma_w \times h_w$), σ_t is total normal stress. In this study the numerator is substituted by net excess pore pressure $\Delta u_{net} = u - u_s - \Delta u_{cen}$, in which Δu_{cen} is the excess pore pressure induced by centrifugal force. If every grain floats in water, namely 100% liquefaction, $\gamma_f = 1.0$.

Test results in this series are shown in Fig. 4.33 in the form of floating ratio versus velocity of mixing rods. Comparable to the features demonstrated in Fig. 4.27, nonlinear relationship

prevails in these three tests. Starting at around 15% upon velocity 3 rpm (1.962 cm/s), γ_f stabilizes at 48%, 65% and 70% in tests $C30S20_{h10.3}$, $C40S20_{h10}$ and $C50S20_{h8}$ respectively.
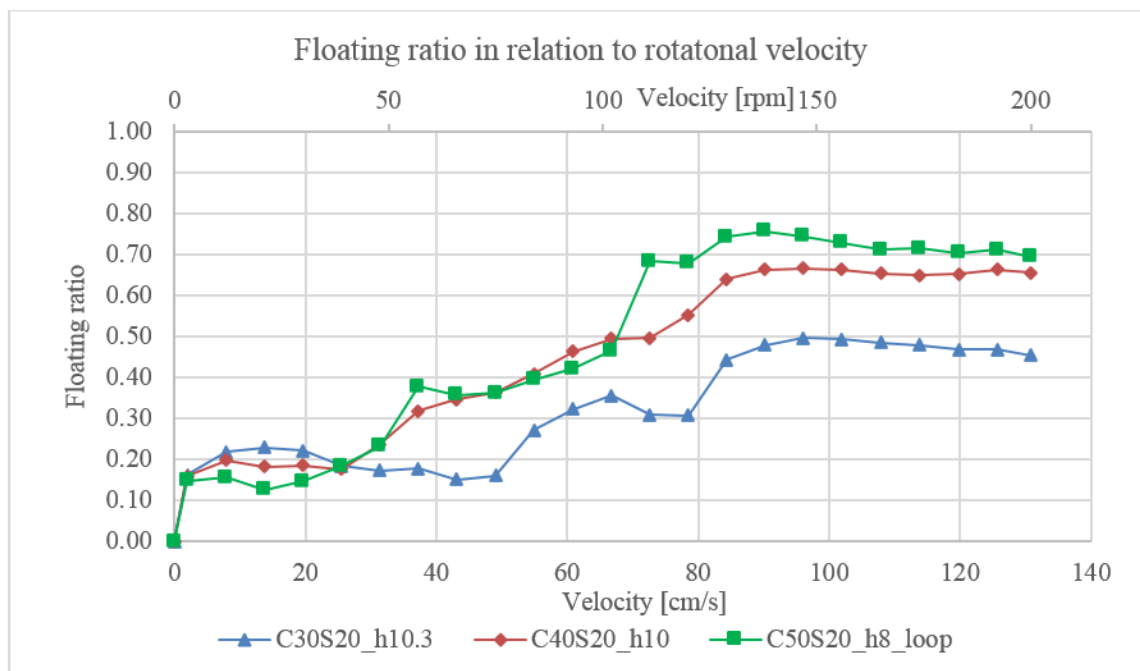
Figure 4.33: Floating ratio versus rotational velocity in test series one

Test series two

Floating ratio in tests $C50S20_{h8}$, $C50S33_{h8}$, $C50S40_{h8}$, and $C50S50_{h8}$, is plotted against rotational velocity in Fig. 4.34. Analogous to net excess pore pressure in these tests, nonlinear relationship presents in each test regarding the whole velocity range. After the initial jump, floating ratio tends to rise at a given velocity with silt content also in a nonlinear manner while few exceptional points can be seen in tests $C50S33_{h8}$ and $C50S40_{h8}$[*]. The highest floating ratio was achieved in test $C50S50_{h8}$ as 98.9% at velocity 129 rpm (84.366 cm/s).
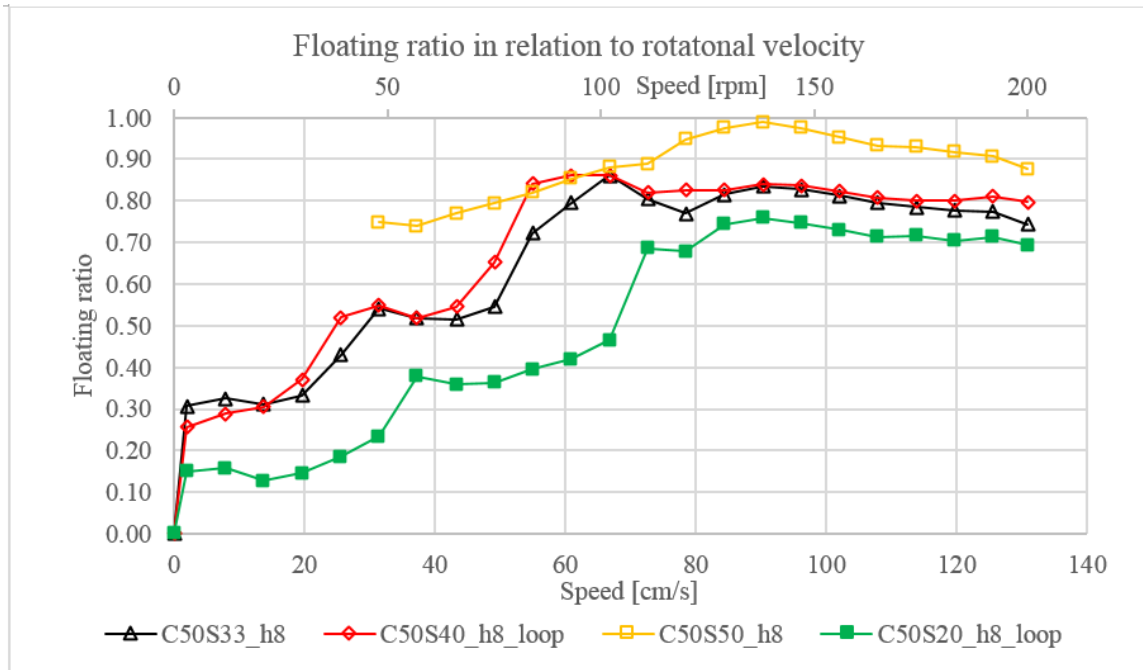
Figure 4.34: Floating ratio versus rotational velocity in test series two excluding $C50S80_{h8}$ and $C50S100_{h8}$

Floating ratio in the rest two tests $C50S80_{h8}$ and $C50S100_{h8}$ is shown in Fig. 4.35 with the previous four tests plotted in dash line. Floating ratios which are around 50% at velocity 3 rpm (1.962 cm/s), lower peak values and reversed relation, prolonged decline, and the ascending tendency at end in test $C50S100_{h8}$ altogether make these two tests extraordinary, and call for further scrutiny and sophisticated explanations.
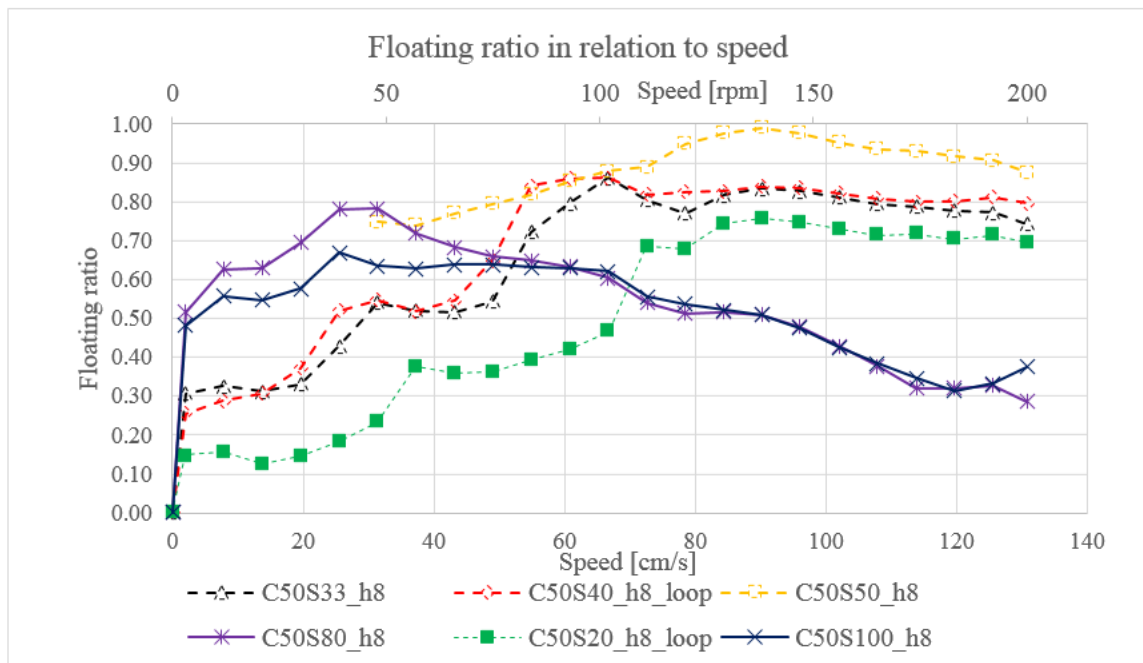
Figure 4.35: Floating ratio versus rotational velocity in test series two

4.6.4. Dissipation

After rotation stopped pore pressures were continuously logged for another 24 hours. Later floating ratio γ_f was plotted versus elapsed time for major tests as shown in Fig. 4.36. The test results revealed full dissipation in less solid-concentrated sample ($C30S20_{h10.3}$) was not that much quick when compared with $C50S20_{h8}$. When silt content varied from 40% to 100% similar time was consumed to reach full dissipation except for $C50S100_{h8}^*$ which took 5 hours before regaining hydrostatic state. Regarding the maintaining of peak floating ratio, it is consistent that longer peak duration is obtained in sample of higher solid concentration and greater silt content.
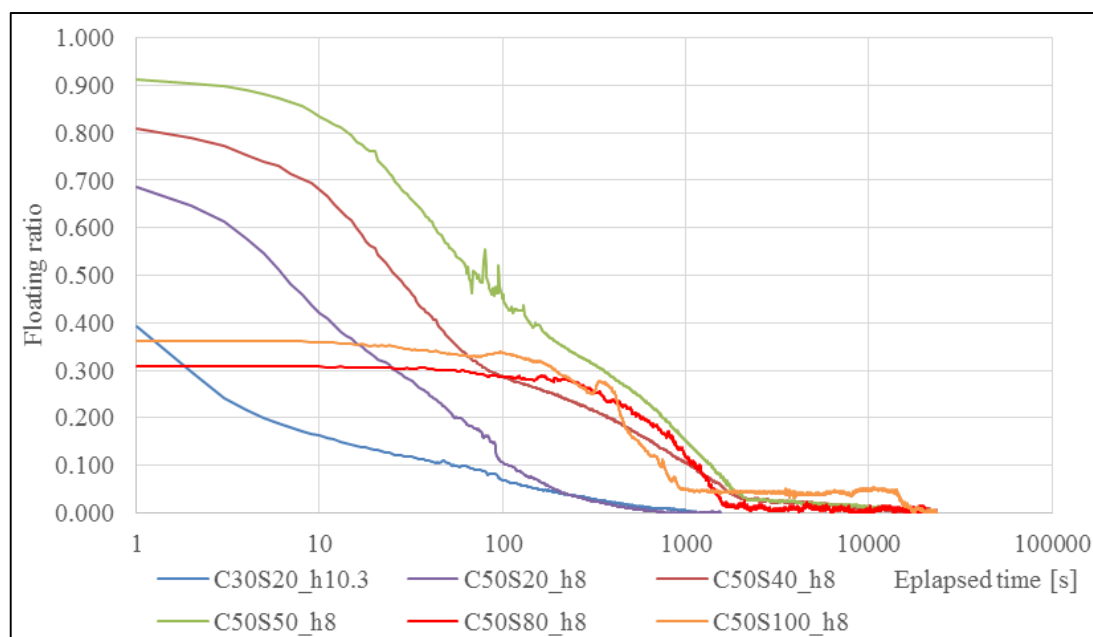
Figure 4.36: Time series of floating ratio after the rotation ceased for different samples

Compared with the results (Fig. 4.37) obtained by Wang & Sassa (2003), results in current study are much less remarkable. Fine grain content, especially clay content, is believed to be able to explain the discrepancy of pore pressure maintaining capacity of samples in the two studies. Table 4.1 lists clay content by weight in the mentioned tests. It appears that nonlinear relationship linking clay content and dissipation time exists. However as sand types and grain size distribution differ greatly in the two studies, it seems implausible to draw a universal correlation.

Table 4.1: Clay content of samples in current study and Wang & Sassa (2003)'s experiment

Test	Clay content % (by weight)
M10	5.59
M20	6.17
M30	6.76
C50S20	0.87
C50S40	1.08
C50S80	1.69
C50S100	2.10
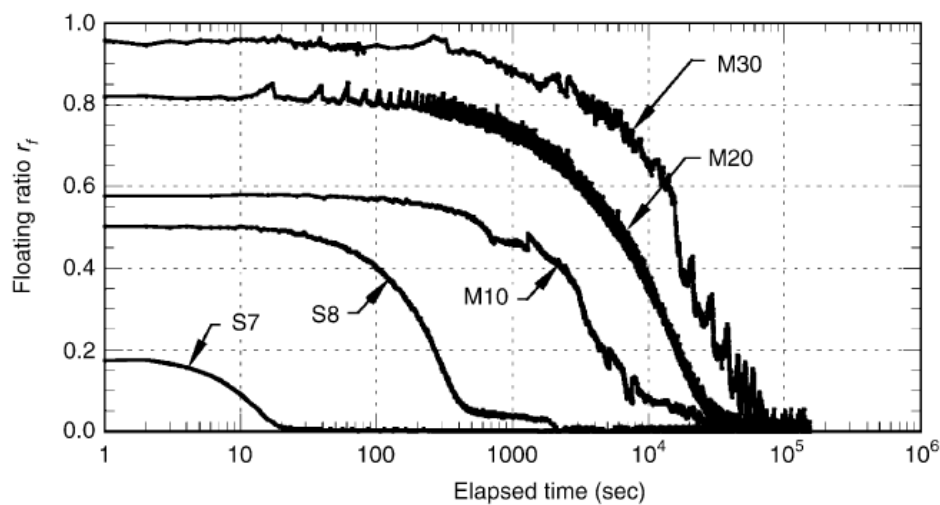
Figure 4.37: Time series of floating ratio after the rotation ceased for different samples in Wang & Sassa (2003)'s experiment

4.7. Comparison and discussion

4.7.1. Comparison

Regarding the relationship between floating ratio versus rotational velocity, results of two test series in current study are compared with Wang and Sassa (2003) (Fig. 2.11) in terms of consistency and discrepancy.

Consistency

- Firstly, the results show positive correlation between floating ratio γ_f and silt content except for $C50S80_{h8}$ and $C50S100_{h8}$.
- Secondly, despite of the initial and transitional stages observed in current study, floating ratio tends to increase with rotational velocity on the whole before reaching peak or constant level.

- Thirdly, the velocities corresponding to floating ratio peak, constant level, and transitional segment migrate towards lower velocity with increasing silt content, and solid fraction concentration as well.

Discrepancy

- More sophisticated floating ratio development processes exist in current study. Instead of smooth growth after initiation, most samples experienced a brief abrupt rise after coming to a steady stage roughly ranging from 3 rpm (1.962 cm/s) to 39 rpm (25.506 cm/s). Initial stagnation stage was given as its name. Afterwards another range with insignificant variation was detected in most tests. However the beginning and ending points varied from one test to another. This stage was named transitional stage.

- Test results from series two exhibit that distinct behaviors started after velocity 25 cm/s. Floating ratio in test $C30S20_{h10.3}$ remained more or less constant until velocity 50 cm/s, while $C40S20_{h10}$ began to rise linearly, and $C50S20_{h8}{}^*$ was about to arrive at transitional stage. Stable stages of these three tests initiated at about the same velocity: 138 rpm, or 90.25 cm/s, which is a contrasting fact when compared with test series two. Not surprisingly, smaller increment of floating ratio was gained from $C40S20_{h10}$ to $C50S20_{h8}{}^*$ then from $C30S20_{h10.3}$ to $C40S20_{h10}$.

- More prominent decline of floating ratio was detected by Wang & Sassa with samples of coarser grains (S7), and stable values with minor deviation were gained with samples with the most fine grain content (M30). On the contrary, in current study the finer samples are found to give more obvious and prolonged decrease of floating ratio ($C50S80_{h8}$ and $C50S100_{h8}$). Besides, these two tests also gave inconsistently low floating ratio with $C50S100_{h8}$ pertaining even lower peak values than $C50S80_{h8}$.

- Considering the proportion of initial floating ratio $\gamma_{f,i}$ to maximum floating ratio $\gamma_{f,max}$ (Fig. 4.38), samples of varying solid fraction concentration shew inverse correlation, while samples of test series two roughly gave higher ratio for greater silt content. Collectively more liquid and fine grains concentrated the mixture is, the higher floating ratio it may reach at low flow velocity.
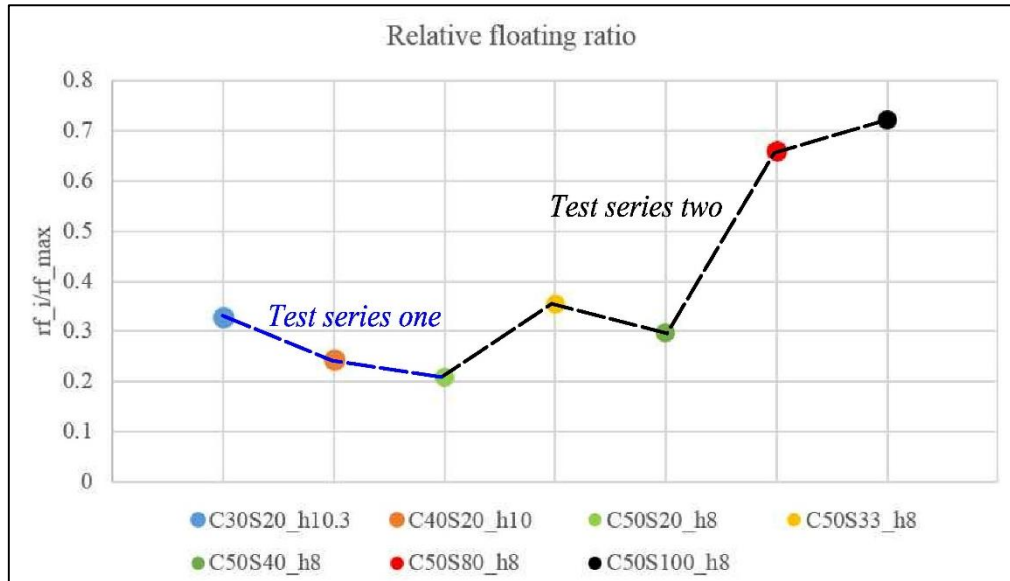
Figure 4.38: Relative floating ratio in different tests

4.7.2. Discussions

Articulation of the mechanism accounting for the increase of pore-liquid pressure with increasing rotational velocity would be necessary for providing basis of other special phenomena's explanation.

Granular temperature, which measures the degree of agitation of solid grains and is determined by the ensemble average of grains' velocity fluctuation (Ogawa 1978, Campbell 1990, Iverson 1997), is capable of deliverring satisfactory interpretation. When the sample is rotated by mixing rods, not only the mean velocity of grains will be increased, but also velocity fluctuation, i.e., higher granular temperature. Interparticle collisions with greater random moving velocity can help grains to fluctuate and float on the pore fluid, thus elevate the pore-liquid pressure (Wang and Sassa 2003).

Initial stagnation

As data from sensors 2a&2b and 3a&3b were majorly used, the excess pore pressure generated near mixing rods at low velocity would rapidly dissipate and could not accumulate at sensors on the wall to high enough magnitude. Later until the majority of solids were stirred up, sensors on cylinder wall finally had more prompt response to rotational velocity increase.

Transitional stage

Observed in most tests, excess pore pressure was maintained for varying duration of time before reaching peak values. A potential explanation could be that within certain velocity range the increase of mean velocity is not necessarily accompanied by the increase of velocity fluctuation. This explanation, which is against the basic assumption in "Granular temperature", could also support the final constant level experienced by some tests.

Floating ratio versus silt content and rotational velocity

- When it comes to the positive correlation between floating ratio and silt content, Wang & Sassa provided a sound interpretation. They wrote that, since the increase in pore pressure was owing to the floating of grains in the fluid. Thus, corresponding to a certain rotational velocity, there will be more grains involved in floating for sample with high silt content, which is finer; consequently, the resultant pore-pressure increment will be greater. However results from $C50S80_{h8}$ and $C50S100_{h8}$ can hardly be deciphered with this hypothesis. As a result a non-monotonic correlation should exist.

- Regarding the decline of floating ratio after certain velocity, Wang & Sassa proposed that "because the mixing rods rotated too fast (relative to the moving mixtures) so that the mixtures could not move with the mixing rods together, the mixtures were subjected to shear; therefore, a reduction in pore pressure evidently occurred as a consequence." However it remained unclear how the reduction in pore pressure is connected with shearing. It may seem clearer to rephrase that when the rods moved too fast, disturbance in suspension became limited, and so did the agitation of particles, hence leading to reduced pore pressure.

- The decline can alternatively be attributed to sediment dilatancy which is caused by particle-breakup. To verify this hypothesis grain size distribution tests were conducted before and after experiment. A representative result is displayed below. As shown in Fig. 4.39 the percentage of grains from 0.075 mm to 0.125 mm decreased from 28.50% to 5.95%. Meanwhile grains with size ranging from 0.02 mm to 0.075 mm increased its percentage from 16.59% to 40.9%. Thus break-up of large particles had actually occurred. Assuming this process lasted for a relatively long time and had kept a steady rate, prolonged decline of floating ratio would be made possible. Furthermore, if the process terminated after a duration, floating ratio may again rise with increasing rotational velocity. The final rising segment of $C50S100_{h8}$ may be explained in such a way.
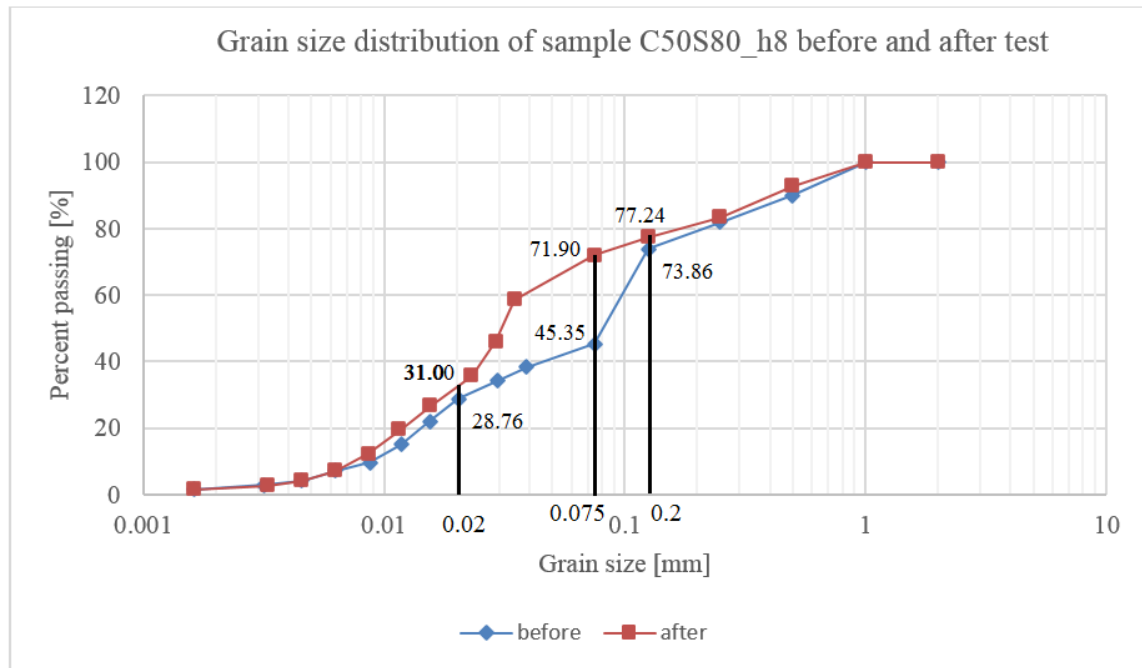
Figure 4.39: Grain size distribution of sample $C50S80_{h8}$ before and after test

- As mentioned in "section 4.5.2", negative net excess pore pressure occurred. Though being subject to shearing and dilation effect both account for pore pressure reduction, it is more likely to have their combination or dilation effect alone explain that distribution because being subject to shearing can only bring down positive pore pressure not lead to negative values independently.

4.7.3. Limitations

Due to the lack of well documented precedent experience of this experiment, many lessons have been learnt through trial and error. Quite a few limitations concerning objectives of the study were realized after tests finish; they are listed as follows.

- In the first series of test, only silt content 20% was explored. Given higher silt content the behavior of samples in this series may be different.
- Porous stones used for wall sensors and base sensors are prone to getting stuck and damage as a result of particle collision. Specified porous stones with appropriate pore size are thus expected.
- Currently the base was not able to be fitted in vacuum fest after being injected with paraffin liquid. Consequently unusable data quality has been induced. Therefore a better saturation procedure is desired.
- As the study is concentrated on the basal layer in debris flow, normal pressure from upper material surely plays an important role towards basal layer behavior. This effect was also not included here.

- The space between two cylinders was found too wide (6,5 cm) compared to the outer cylinder radius. Narrower space is believed to be able to offer more velocity-uniform flow.

- Decline of pore pressure was revealed to derive from rods-shearing effects and sediment dilatancy, but their individual contribution, the rate and timing of particle break-up remain unclear. It would be pleasant to have these two factors separately studied.

- In this experiment horizontal rotation not only resulted extra excess pore pressure but also forced sediment particles to cluster near outer cylinder. Thence solid fraction concentration would deviate from that designed.

5. Conclusion

5.1. Main messages

Based on tests results presented in this study the following messages can be drawn corresponding to objectives.

1. As for objective one, the coaxial cylinder apparatus has been proved effective in delivering data on pore pressure built-up and its distribution though some shortcomings remain to be improved.

2. Concerning the second and third objectives, pore pressure built-up in both series of test is correlated with rotational velocity in nonlinear manner. Universal formulation fitting all results seems unlikely as some tests shew distinct initial stagnation and transitional stage while others maintained more or less linear growth before reaching stable value. Samples $C50S80_{h8}$ and $C50S100_{h8}$ even possess prolonged decline, which indicates that quite a wide phenomenological spectrum has been covered. More samples with intermediate silt content (from 50% to 80%) and solid fraction concentration seem worthwhile of further inspection.

3. Corresponding to objective four. Compared with samples of less silt content, more drastic growth after initiation but lower maximum values of pore pressure built-up were observed for samples $C50S80_{h8}$ and $C50S100_{h8}$. Knowing that finer sample in Wang and Sassa's work (loess with $D_{50} = 0.0182\ mm$) gave not only higher pore pressure built-up but also stable endings, a reasonable postulation could be constructed on the notion «most breakable grain sizes" that is concentrated from 0.075 mm to 0.125 mm in current study. Combined with the fact that finer grains can float easier, test results in the second series and Wang & Sassa's work can be explained under a global scheme. That is to say when most grains are with size above the «most breakable grain sizes", sharper pore pressure built-up, more notable and earlier decline could be expected for finer samples. On the other side when most grains sizes are below it, higher pore pressure built-up and also floating ratio would be easily achieved without noticeble decline upon rapid rotation.

4. Regarding objective five. The patterns of pore pressure distribution described in "section 4.5.2" could be interpreted that, in samples of less silt the difference of grain size composition between mid-height and base is greater than samples of richer silt ($C50S80_{h8}$ and $C50S100_{h8}$). Besides, the proportion of "most breakable grains" is also higher in the former group of samples.

5. In natural event the basal layer of debris flow is expected to experience ever-reducing friction and maximum pore pressure built-up soon after initiation, because the maximum pore pressure built-up found in current tests was below 1 m/s, and peak

velocity up to 10 m/s during transportation is regarded common from observations (Hutter, Svendsen et al. 1994). Therefore the mobility of debris flow would be highly facilitated before notable reduction of pore pressure built-up due to sediment dilatancy. At higher velocity the reduced pore pressure, i.e., higher friction resistance would instead help drag the flow.

6. The first series of test suggested that pore pressure built-up tended to increase with solid concentration. Considering in real event solids are more concentrated at the front, and the rear consists of richer liquid, thus, apart from boulders at front, higher frictional coefficient would be seen near the rear. This distribution of resistance would help elongate debris body and accelerate deposition.
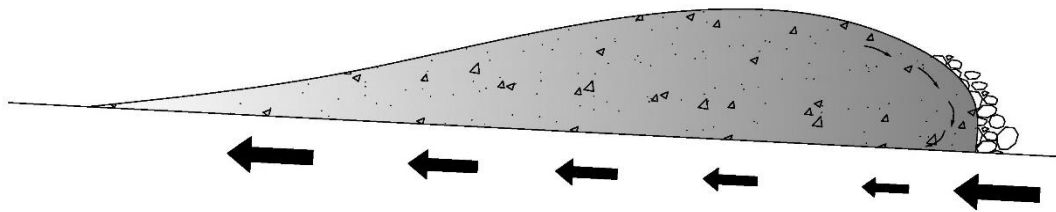
Figure 5.1: Friction coefficient longitudinal distribution

5.2. Shortcomings

Assessed in the domain of physical modelling of debris flow, some shortcomings of co-axial cylinder experiment can be named as below.

- At low speed the disturbance induced by mixing rods is confined within narrow space. Even though the generated pore pressure could be captured by sensors beneath rods, the result is still of flawed representativeness before radial dissipation becomes negligible.
- First of all, energy replenished to debris mass is from rotating rods, other than gravity. The adoption of steel rods may aggravate the break-up of grains, which could be less significant in real events.
- For the purpose of studying entrainment in this apparatus, some modifications are still needed.

6. Scope of future work

As it is described in (Section 1.5 and Section 4.2.4), many efforts need to be done by fulfilling the limitations of this study. Possible future works are listed below:

- Concerning samples and the apparatus:
  - Finer soil with greater clay content, for instance exceeding 5%, is interesting to test with to see if stable floating ratio approaching unity is possible to achieve. Samples of higher fixed silt content (>20%) and varied solid fraction concentration are also expected to shed light on a broader spectrum of samples.
  - Specified porous stones with appropriate pore size are expected to avoid being stuck and damaged upon collision. Better saturation and vacuumization procedures for the porous stones and ducts at base are needed.
  - Larger inner cylinder is believed to be able to deliver more radially-uniform velocity field, less lateral dissipation under low velocity and less severe particle migration upon centrifugal force. Modification can be directly made on the current base.
- Concerning test procedure and verification:
  - Normal pressure from upper material plays an important role towards basal layer behavior, thus more representative results are promising if this effect could be modeled.
  - Work to separate the two factors accounting for decline of pore pressure built-up: rods-shearing and sediment dilatancy, would be valuable. Scrutiny into transitional stage is also expected to be fruitful.
  - In-situ or large scale flume test observations of pore pressure built-up decline due to dilatancy.
  - Verify the existence of "most breakable grain sizes" and study the geometric and physical properties of those particles.
- Construct empirical or analytical correlations to incorporate the significance of pore pressure built-up in debris flow mobility simulation models.

References

Bagnold, R. A. (1954). Experiments on a Gravity-Free Dispersion of Large Solid Spheres in a Newtonian Fluid under Shear. *Proceedings of the Royal Society of London Series a-Mathematical and Physical Sciences, 225*(1160), 49-63. doi: DOI 10.1098/rspa.1954.0186

Bardou, E., Ancey, C., Bonnard, C., & Vulliet, L. (2003). *Classification of debris-flow deposits for hazard assessment in alpine areas.* Paper presented at the 3th International Conference on Debris-Flow hazards mitigation: mechanics, prediction, and assessment.

Berti, M., & Simoni, A. (2007). Prediction of debris flow inundation areas using empirical mobility relationships. *Geomorphology, 90*(1), 144-161.

Brown, S. M. (1992). The vertically rotating flume for use as a rheometer.

Campbell, C. S. (1990). Rapid Granular Flows. *Annual review of fluid mechanics, 22*, 57-92. doi: DOI 10.1146/annurev.fl.22.010190.000421

Bagnold, R. A. (1954). "Experiments on a Gravity-Free Dispersion of Large Solid Spheres in a Newtonian Fluid under Shear." Proceedings of the Royal Society of London Series a-Mathematical and Physical Sciences 225(1160): 49-63.

Bardou, E., C. Ancey, C. Bonnard and L. Vulliet (2003). Classification of debris-flow deposits for hazard assessment in alpine areas. 3th International Conference on Debris-Flow hazards mitigation: mechanics, prediction, and assessment., Millpress.

Berti, M. and A. Simoni (2007). "Prediction of debris flow inundation areas using empirical mobility relationships." Geomorphology 90(1): 144-161.

Brown, S. M. (1992). "The vertically rotating flume for use as a rheometer."

Campbell, C. S. (1990). "Rapid Granular Flows." Annual Review of Fluid Mechanics 22: 57-92.

Casagrande, A. (1940). "Characteristics of cohesionless soils affecting the stability of slopes and earth fills." Contributions to Soils Mechanics, 1925-1940.

Coussot, P. (1992). Rhéologie des laves torrentielles-Etude de dispersions et suspensions concentrées, Thèse de l'Institut National Polytechnique de Grenoble, France, 420p.

Coussot, P. and M. Meunier (1996). "Recognition, classification and mechanical description of debris flows." Earth-Science Reviews 40(3): 209-227.

Crosta, G., S. Cucchiaro and P. Frattini (2003). Validation of semi-empirical relationships for the definition of debris-flow behavior in granular materials. 3rd International Conference on Debris-Flow Hazards Mitigation, MILLPRESS SCIENCE PUBLISHERS.

De Wrachien, D. and C. A. Brebbia (2010). Monitoring, Simulation, Prevention and Remediation of Dense and Debris Flows III. SOUTHAMPTON, WIT Press.

Fiskum, E. (2014). Flomskred – Litteraturstudie og modellforsøk med voller som sikringstiltak, NTNU.

Griswold, J. P. (2004). Mobility statistics and hazard mapping for non-volcanic debris flows and rock avalanches, Portland State University.

Herrmann, H. J. and S. Luding (1998). "Modeling granular media on the computer." Continuum Mechanics and Thermodynamics 10(4): 189-231.

Hill, H. M. (1966). "Bed forms due to a fluid stream." J. Hydraul. Div., Proc. ASCE 92: 127-143.

Hotta, N. (2011). "Pore water pressure distributions of granular mixture flow in a rotating mill." Debris-Flow Hazards Mitigation: Mechanics, Prediction and Assessment, edited by:

Genevois, R., Hamilton, DL, and Prestininzi, A., Casa Editrice Universita La Sapienza, Roma: 319-330.

Hotta, N. and K. Miyamoto (2008). "Phase classification of laboratory debris flows over a rigid bed based on the relative flow depth and friction coefficients." International Journal of Erosion Control Engineering 1(2): 54-61.

Huizinga, R. J. (1993). "An analysis of the two-dimensional flow in a vertically rotating flume."

Huizinga, R. J. (1996). "Verification of vertically rotating flume using non-Newtonian fluids." Journal of Hydraulic Engineering 122(8): 456-459.

Hungr, O. (1995). "A Model for the Runout Analysis of Rapid Flow Slides, Debris Flows, and Avalanches." Canadian Geotechnical Journal 32(4): 610-623.

Hungr, O. and M. Jackson (2005). Debris flow hazards and related phenomena.

Hungr, O., S. McDougall and M. Bovis (2005). Entrainment of material by debris flows. Debris-flow hazards and related phenomena, Springer: 135-158.

Hutter, K., B. Svendsen and D. Rickenmann (1994). "Debris flow modeling: A review." Continuum mechanics and thermodynamics 8(1): 1-35.

Infrarisk (2013). http://www.ngi.no/en/prosjektnett/infrarisk.

Iverson, R. M. (1997). "The physics of debris flows." Reviews of Geophysics 35(3): 245-296.

Iverson, R. M. (2013). "Numerical study on the entrainment of bed material into rapid landslides." Geotechnique 63(10): 887-888.

Iverson, R. M. (2014). "Debris flows: behaviour and hazard assessment." Geology Today 30(1): 15-20.

Iverson, R. M., J. E. Costa and R. G. LaHusen (1992). Debris-flow flume at H. J. Andrews Experimental Forest, Oregon. Open-File Report.

Iverson, R. M., M. Logan, R. G. LaHusen and M. Berti (2010). "The perfect debris flow? Aggregated results from 28 large-scale experiments." Journal of Geophysical Research-Earth Surface 115.

Iverson, R. M., S. P. Schilling and J. W. Vallance (1998). "Objective delineation of lahar-inundation hazard zones." Geological Society of America Bulletin 110(8): 972-984.

Jakob, M. and O. Hungr (2005). Debris-flow hazards and related phenomena. Berlin ; New York, Springer.

Julien, P. Y. and Y. Q. Lan (1991). "Rheology of Hyperconcentrations." Journal of Hydraulic Engineering-Asce 117(3): 346-353.

Kaitna, R. and D. Rickenmann (2007). "A new experimental facility for laboratory debris flow investigation." Journal of Hydraulic Research 45(6): 797-810.

Kramer, S. L. and H. B. Seed (1988). "Initiation of Soil Liquefaction under Static Loading Conditions." Journal of Geotechnical Engineering-Asce 114(4): 412-430.

Leonardi, A., F. K. Wittel, M. Mendoza and H. J. Herrmann (2014). "Coupled DEM-LBM method for the free-surface simulation of heterogeneous suspensions." Computational Particle Mechanics 1(1): 3-13.

Lorenzini, G. and N. Mazza (2004). Debris flow: Phenomenology and rheological modelling, Wit Press.

McDougall, S. and O. Hungr (2004). "A model for the analysis of rapid landslide motion across three-dimensional terrain." Canadian Geotechnical Journal 41(6): 1084-1097.

Nadim, F., O. Kjekstad, P. Peduzzi, C. Herold and C. Jaedicke (2006). "Global landslide and avalanche hotspots." Landslides 3(2): 159-173.

NIFS (2014). "Naturfareprosjektet - publications 26/2014 and 37/2014."

NVE (2011). "Plan for skredfarekartlegging- Delrapport jord og flomskred." NVEs Publication nr 26/2011.

O'Brien, J. and P. Julien (1985). "Physical properties and mechanics of hyperconcentrated sediment flows." Proc. ASCE HD Delineation of landslides, flash flood and debris flow Hazards.

Ogawa, S. (1978). Multitemperature theory of granular materials. Proc. of US-Japan Symp. on Continuum Mechanics and Statistical Approaches to the Mechanics of Granular Media, Gakujutsu Bunken.

Papa, M., S. Egashira and T. Itoh (2004). "Critical conditions of bed sediment entrainment due to debris flow." Natural Hazards and Earth System Sciences 4(3): 469-474.

Reid, M. E. and R. M. Iverson (2011). "entrainment of bed sediment by debris flows: results from large-scale experiments."

Reid, M. E., R. G. LaHusen and R. M. Iverson (1997). "Debris-flow initiation experiments using diverse hydrologic triggers." Debris-Flow Hazards Mitigation: Mechanics, Prediction & Assessment: 1-11.

Rickenmann, D., D. Weber and B. Stepanov (2003). "Erosion by debris flows in field and laboratory experiments." Debris-Flow Hazards Mitigation: Mechanics, Prediction, and Assessment, Vols 1 and 2: 883-894.

Sassa, K. (1988). "Special Lecture - Geotechnical Model for the Motion of Landslides." Landslides, Vols 1-3: 37-55.

Sassa, K. (1998). Recent urban landslide disasters in Japan and their mechanisms. Proceedings of 2nd International Conference on Environmental Management,''Environmental Management'', Australia.

Sassa, K., H. Fukuoka, F. W. Wang and S. G. Evans (1998). "Sliding surface liquefaction and undrained loading mechanism in rapid landslides in Japan and Canada." Eighth International Congress International Association for Engineering Geology and the Environment, Proceedings, Vols 1-5: 1923-1930.

Sassa, K., H. Fukuoka, G. H. Wang and N. Ishikawa (2004). "Undrained dynamic-loading ring-shear apparatus and its application to landslide dynamics." Landslides 1(1): 7-19.

Savage, S. B. and C. K. K. Lun (1988). "Particle-Size Segregation in Inclined Chute Flow of Dry Cohesionless Granular Solids." Journal of Fluid Mechanics 189: 311-335.

Stiny, J. (1910). Die Muren - Versuch einer Monographie mit besonderer Berücksichtigung der Verhältnisse in den Tiroler Alpen, University Library of Innsbruck; University and Regional Library of Tyrol.

Takahashi, T. (1978). "Mechanical characteristics of debris flow." Journal of the Hydraulics Division 104(8): 1153-1169.

Takahashi, T. (1981). "Debris flow." Annual review of fluid mechanics 13(1): 57-77.

Takahashi, T. (2014). Debris flow: mechanics, prediction and countermeasures. London, CRC Press.

Takahashi, T., H. Nakagawa, T. Harada and Y. Yamashiki (1992). "Routing Debris Flows with Particle Segregation." Journal of Hydraulic Engineering-Asce 118(11): 1490-1507.

Wang, G. H. and K. Sassa (2002). "Post-failure mobility of saturated sands in undrained load-controlled ring shear tests." Canadian Geotechnical Journal 39(4): 821-837.

Wang, G. H. and K. Sassa (2003). "Pore-pressure generation and movement of rainfall-induced landslides: effects of grain size and fine-particle content." Engineering Geology 69(1-2): 109-125.

Coussot, P., & Meunier, M. (1996). Recognition, classification and mechanical description of debris flows. *Earth-Science Reviews, 40*(3), 209-227.

Crosta, G., Cucchiaro, S., & Frattini, P. (2003). *Validation of semi-empirical relationships for the definition of debris-flow behavior in granular materials.* Paper presented at the 3rd International Conference on Debris-Flow Hazards Mitigation.

De Wrachien, D., & Brebbia, C. A. (2010). *Monitoring, Simulation, Prevention and Remediation of Dense and Debris Flows III.* SOUTHAMPTON: WIT Press.

Fiskum, E. (2014). *Flomskred – Litteraturstudie og modellforsøk med voller som sikringstiltak.* NTNU.

Griswold, J. P. (2004). *Mobility statistics and hazard mapping for non-volcanic debris flows and rock avalanches.* Portland State University.

Herrmann, H. J., & Luding, S. (1998). Modeling granular media on the computer. *Continuum Mechanics and Thermodynamics, 10*(4), 189-231. doi: DOI 10.1007/s001610050089

Hill, H. M. (1966). Bed forms due to a fluid stream. *J. Hydraul. Div., Proc. ASCE, 92*, 127-143.

Hooke, R. L. B. (1967). Processes on Arid-Region Alluvial Fans. *Journal of Geology, 75*(4), 438-&.

Hotta, N. (2011). Pore water pressure distributions of granular mixture flow in a rotating mill. *Debris-Flow Hazards Mitigation: Mechanics, Prediction and Assessment, edited by: Genevois, R., Hamilton, DL, and Prestininzi, A., Casa Editrice Universita La Sapienza, Roma*, 319-330.

Hotta, N., & Miyamoto, K. (2008). Phase classification of laboratory debris flows over a rigid bed based on the relative flow depth and friction coefficients. *International Journal of Erosion Control Engineering, 1*(2), 54-61.

Huizinga, R. J. (1993). An analysis of the two-dimensional flow in a vertically rotating flume.

Huizinga, R. J. (1996). Verification of vertically rotating flume using non-Newtonian fluids. *Journal of hydraulic engineering, 122*(8), 456-459.

Hungr, O. (1995). A Model for the Runout Analysis of Rapid Flow Slides, Debris Flows, and Avalanches. *Canadian Geotechnical Journal, 32*(4), 610-623. doi: Doi 10.1139/T95-063

Hungr, O., & Jackson, M. (2005). *Debris flow hazards and related phenomena.*

Hungr, O., McDougall, S., & Bovis, M. (2005). Entrainment of material by debris flows *Debris-flow hazards and related phenomena* (pp. 135-158): Springer.

Hutter, K., Svendsen, B., & Rickenmann, D. (1994). Debris flow modeling: A review. *Continuum Mechanics and Thermodynamics, 8*(1), 1-35.

Iverson, R. M. (1997). The physics of debris flows. *Reviews of Geophysics, 35*(3), 245-296. doi: Doi 10.1029/97rg00426

Iverson, R. M. (2013). Numerical study on the entrainment of bed material into rapid landslides. *Geotechnique, 63*(10), 887-888. doi: DOI 10.1680/geot.12.D.007

Iverson, R. M. (2014). Debris flows: behaviour and hazard assessment. *Geology Today, 30*(1), 15-20.

Iverson, R. M., Costa, J. E., & LaHusen, R. G. (1992). Debris-flow flume at H. J. Andrews Experimental Forest, Oregon *Open-File Report* (- ed.).

Iverson, R. M., Logan, M., LaHusen, R. G., & Berti, M. (2010). The perfect debris flow? Aggregated results from 28 large-scale experiments. *Journal of Geophysical Research-Earth Surface, 115*. doi: Artn F03005

Doi 10.1029/2009jf001514

Iverson, R. M., Schilling, S. P., & Vallance, J. W. (1998). Objective delineation of lahar-inundation hazard zones. *Geological Society of America Bulletin, 110*(8), 972-984.

Jaedicke, C., Lied, K., & Kronholm, K. (2009). Integrated database for rapid mass movements in Norway. *Natural Hazards and Earth System Sciences, 9*(2), 469-479.

Jaedicke, C., Solheim, A., Blikra, L. H., Stalsberg, K., Sorteberg, A., Aaheim, A., . . . Mestl, H. (2008). Spatial and temporal variations of Norwegian geohazards in a changing climate, the GeoExtreme Project. *Natural Hazards and Earth System Sciences, 8*(4), 893-904.

Jakob, M., & Hungr, O. (2005). *Debris-flow hazards and related phenomena*. Berlin ; New York: Springer.

Johnson, A. M. (1970). *Physical processes in geology: A method for interpretation of natural phenomena; intrusions in igneous rocks, fractures, and folds, flow of debris and ice*: Freeman, Cooper.

Kaitna, R., & Rickenmann, D. (2007). A new experimental facility for laboratory debris flow investigation. *Journal of Hydraulic Research, 45*(6), 797-810.

Kramer, S. L., & Seed, H. B. (1988). Initiation of Soil Liquefaction under Static Loading Conditions. *Journal of Geotechnical Engineering-Asce, 114*(4), 412-430.

Leonardi, A., Wittel, F. K., Mendoza, M., & Herrmann, H. J. (2014). Coupled DEM-LBM method for the free-surface simulation of heterogeneous suspensions. *Computational Particle Mechanics, 1*(1), 3-13.

Lorenzini, G., & Mazza, N. (2004). *Debris flow: Phenomenology and rheological modelling*: Wit Press.

McDougall, S., & Hungr, O. (2004). A model for the analysis of rapid landslide motion across three-dimensional terrain. *Canadian Geotechnical Journal, 41*(6), 1084-1097. doi: 10.1139/t04-052

Ogawa, S. (1978). *Multitemperature theory of granular materials*. Paper presented at the Proc. of US-Japan Symp. on Continuum Mechanics and Statistical Approaches to the Mechanics of Granular Media.

Papa, M., Egashira, S., & Itoh, T. (2004). Critical conditions of bed sediment entrainment due to debris flow. *Natural Hazards and Earth System Sciences, 4*(3), 469-474.

Reid, M. E., & Iverson, R. M. (2011). entrainment of bed sediment by debris flows: results from large-scale experiments.

Rickenmann, D., Weber, D., & Stepanov, B. (2003). Erosion by debris flows in field and laboratory experiments. *Debris-Flow Hazards Mitigation: Mechanics, Prediction, and Assessment, Vols 1 and 2*, 883-894.

Sassa, K. (1988). Special Lecture - Geotechnical Model for the Motion of Landslides. *Landslides, Vols 1-3*, 37-55.

Sassa, K. (1998). *Recent urban landslide disasters in Japan and their mechanisms*. Paper presented at the Proceedings of 2nd International Conference on Environmental Management,''Environmental Management'', Australia.

Sassa, K., Fukuoka, H., Wang, F. W., & Evans, S. G. (1998). Sliding surface liquefaction and undrained loading mechanism in rapid landslides in Japan and Canada. *Eighth International Congress International Association for Engineering Geology and the Environment, Proceedings, Vols 1-5*, 1923-1930.

Sassa, K., Fukuoka, H., Wang, G. H., & Ishikawa, N. (2004). Undrained dynamic-loading ring-shear apparatus and its application to landslide dynamics. *Landslides, 1*(1), 7-19. doi: DOI 10.1007/s10346-003-0004-y

Savage, S. B., & Lun, C. K. K. (1988). Particle-Size Segregation in Inclined Chute Flow of Dry Cohesionless Granular Solids. *Journal of Fluid Mechanics, 189*, 311-335. doi: Doi 10.1017/S002211208800103x

Stiny, J. (1910). *Die Muren - Versuch einer Monographie mit besonderer Berücksichtigung der Verhältnisse in den Tiroler Alpen*: University Library of Innsbruck; University and Regional Library of Tyrol.

Takahashi, T. (1978). Mechanical characteristics of debris flow. *Journal of the Hydraulics Division, 104*(8), 1153-1169.

Takahashi, T. (1981). Debris flow. *Annual review of fluid mechanics, 13*(1), 57-77.

Takahashi, T. (2009). A review of Japanese debris flow research. *International Journal of Erosion Control Engineering, 2*(1), 1-14.

Takahashi, T. (2014). *Debris flow: mechanics, prediction and countermeasures*. London: CRC Press.

Takahashi, T., Nakagawa, H., Harada, T., & Yamashiki, Y. (1992). Routing Debris Flows with Particle Segregation. *Journal of Hydraulic Engineering-Asce, 118*(11), 1490-1507. doi: Doi 10.1061/(Asce)0733-9429(1992)118:11(1490)

Takahashi, T., & Yoshida, H. (1979). Study on the deposition of debris flows, part 1-deposition due to abrupt change of bed slope. *Annals of the Disaster Prevention Research Institute, Kyoto University, Kyoto, Japan, 22*.

Wang, G. H., & Sassa, K. (2002). Post-failure mobility of saturated sands in undrained load-controlled ring shear tests. *Canadian Geotechnical Journal, 39*(4), 821-837. doi: Doi 10.1139/T02-032

Wang, G. H., & Sassa, K. (2003). Pore-pressure generation and movement of rainfall-induced landslides: effects of grain size and fine-particle content. *Engineering Geology, 69*(1-2), 109-125. doi: Doi 10.1016/S0013-7952(02)00268-5

Appendices

Appendix A: Drawings of coaxial cylinder apparatus
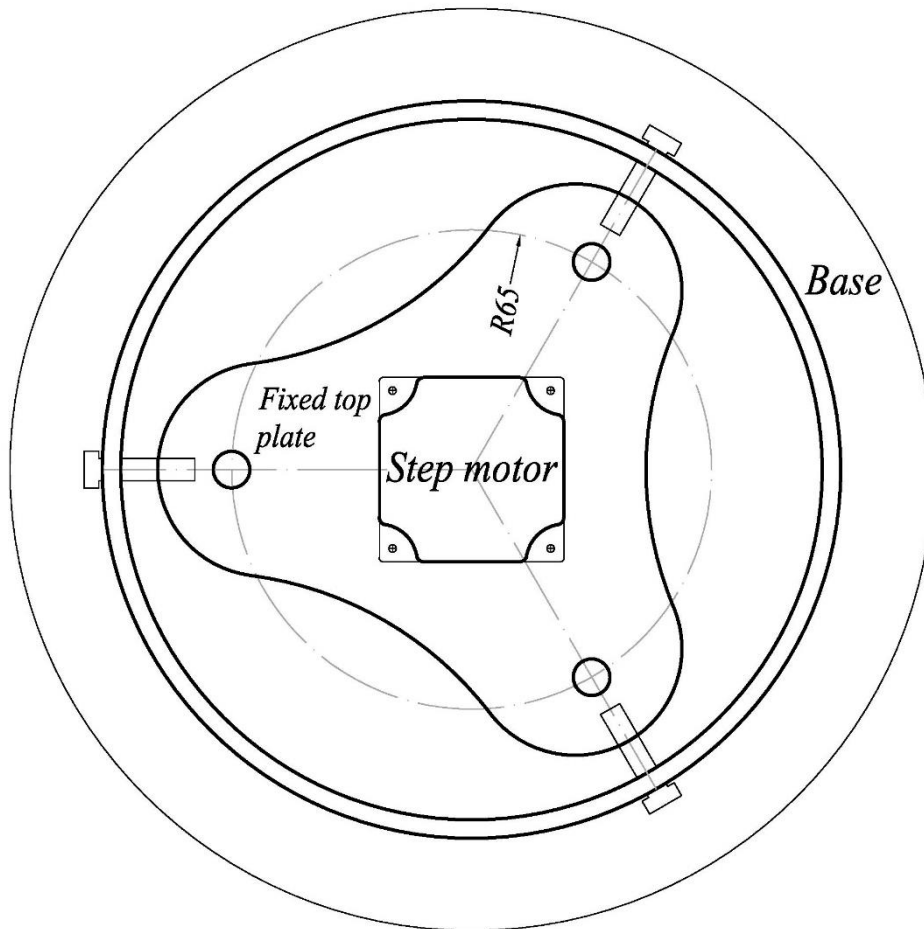
(measured in mm)
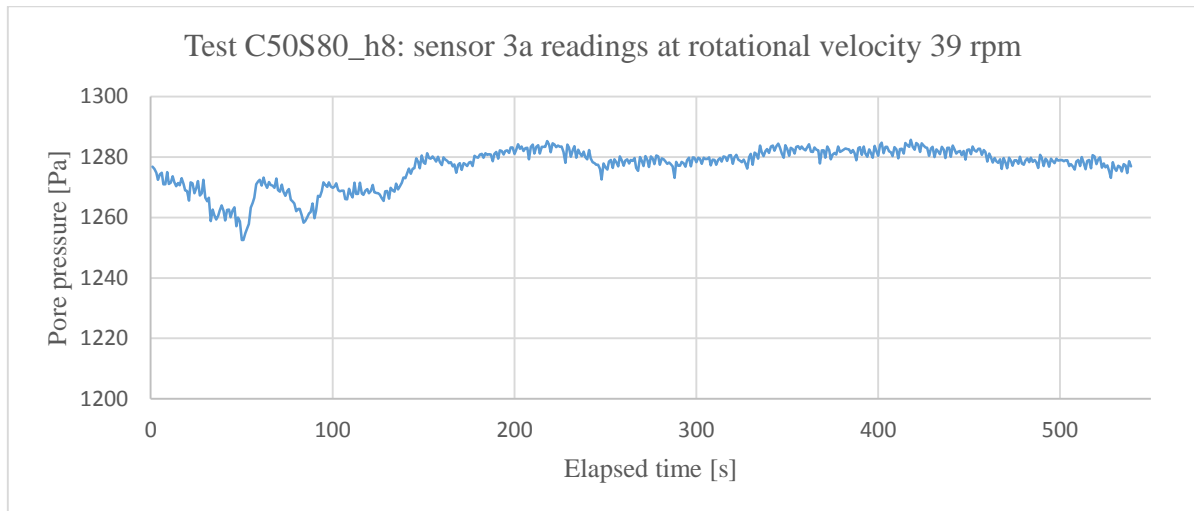
$A - A$

(measured in mm)

Appendix B:

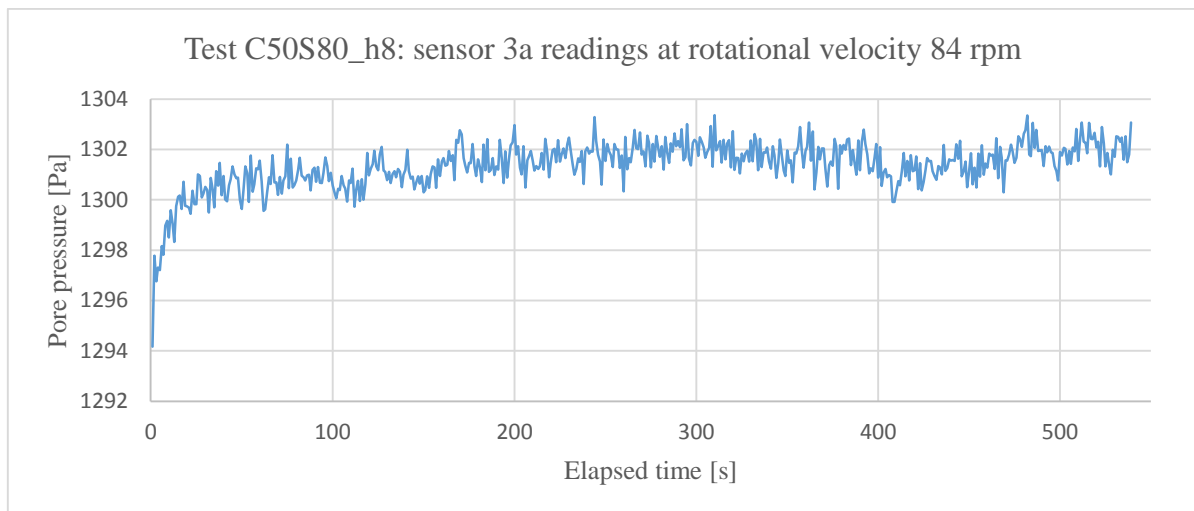*Figure 0.1: Pore pressure recorded over time at velocity 39 rpm in C50S80_h8*

Figure 0.2: Pore pressure recorded over time at velocity 84 rpm in C50S80_h8
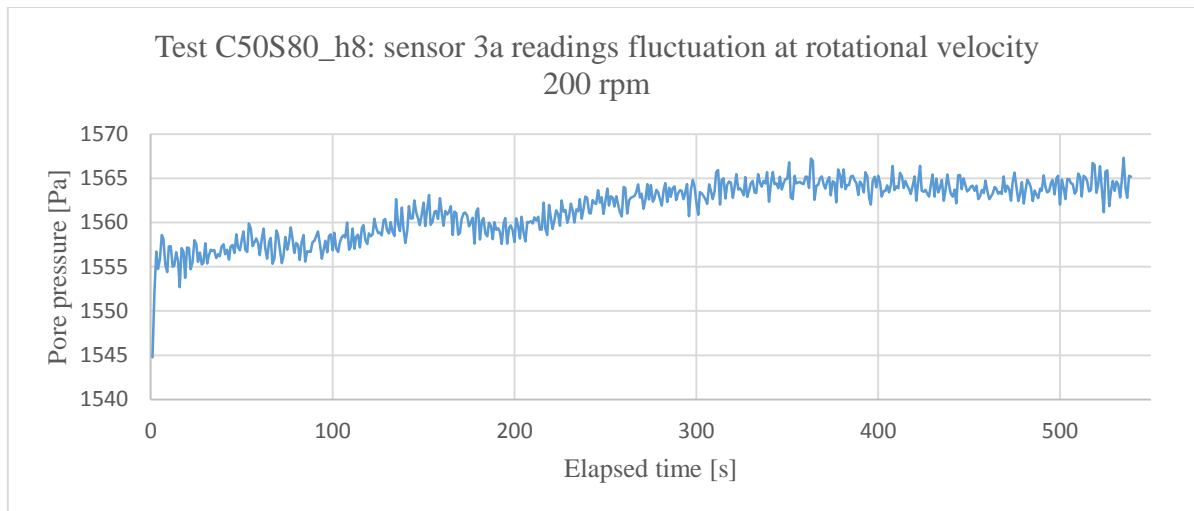
Figure 0.3: Pore pressure recorded over time at velocity 200 rpm in C50S80_h8